Investigation of the Fluid Dynamics of a Gas Jet Expansion in a Liquid Pool

L. Meyer, D. Wilhelm
Institut für Neutronenphysik und Reaktortechnik

Kernforschungszentrum Karlsruhe

KERNFORSCHUNGSZENTRUM KARLSRUHE

Institut für Neutronenphysik und Reaktortechnik

KfK 5307

Investigation of the Fluid Dynamics of a Gas Jet Expansion in a Liquid Pool

L. Meyer, D. Wilhelm

Abstract

Experiments and calculations with the AFDM-code are described on a high pressure gas injection into a low pressure liquid pool with a free surface. The expanding bubble accelerates the water and a mixing of both gas and water at the interface takes place. The rate and magnitude of this entrainment process for different initial conditions is investigated. Also the shape of the bubble, the velocity of the water and pressures during the transient are determined. The entrainment rates found in the experiments are compared with different entrainment models.

Most of the experiments are recalculated with the two-dimensional, multi-phase, three-velocity-field computer code AFDM. For the gas discharge into a large open pool, the calculational results agree well with the experimental data. It is found that a turbulence model is needed to better represent the water flow near structures. A higher order differencing method for space discretization is necessary to track the sharp interfaces. Using this differencing method, the interface is always smeared over three computational cells. It is proven that the change of the radial cell size by more than 100% has an effect on the results. The shapes of the expanding bubbles calculated by AFDM are similar to those observed in the experiments. The biggest discrepancies are found for the high pressure bubbles. The experimental bubbles are generally more pointed at the top. The experimental entrainment is of the same order of magnitude as the smearing of AFDM bubble interfaces by numerical diffusion.

Untersuchung der Expansion eines Gasstrahles in einem Wassertank

Zusammenfassung

Experimente und Nachrechnungen mit dem AFDM-code über die Expansion eines Hochdruck-Gasstrahles in einem Wassertank werden beschrieben. Die expandierende Blase beschleunigt das Wasser, und Gas und Wasser vermischen sich an der Blasenoberfläche. Die Stärke dieser Vermischungsrate wird für verschiedene Anfangsbedingungen bestimmt. Ebenso werden die Blasenform, die Wassergeschwindigkeit und die Drücke während des transienten Vorganges bestimmt. Die experimentell bestimmten Vermischungsraten werden mit theoretischen Modellen verglichen.

Die meisten Experimente sind mit dem zweidimensionalen Mehrphasen-Code AFDM nachgerechnet worden. Für die Gasexpansion in einen weiten, offenen Pool stimmen die Rechenergebnisse gut mit den experimentellen Daten überein. Ein Turbulenzmodell wäre nötig, um die Wasserströmung in der Nähe von Strukturen besser beschreiben zu können. Für die Ortsdiskretisierung wird eine Methode höherer Ordnung benutzt, um die scharfen Phasenoberflächen verfolgen zu können. Mit dieser Diskretisierungsmethode wird die Oberfläche immer über drei Zellen verschmiert. Es wird nachgewiesen, daß die Änderung der Zellgrößen um mehr als 100% einen Einfluß auf die Resultate hat. Die von AFDM berechneten Blasenformen sind ähnlich denen im Experiment. Die größten Abweichungen ergeben sich für die hohen Drücke. Die experimentellen Blasen sind im allgemeinen spitzer am oberen Ende. Die experimentellen Vermischungsraten sind von der gleichen Größenordnung wie die Verschmierung der Blasenoberfläche durch numerische Diffusion.

INTRODUCTION

The injection of a high pressure gas into a stagnant liquid pool is the characteristic phenomenon during the expansion phase of a hypothetical core disruptive accident in liquid-metal fast breeder reactors. High pressure, high temperature fuel (UO_2) and steel vapor is driven out of the damaged core region into the overlying pool of sodium. For the further development of the accident sequence the rate of mixing between the hot vapor and the relatively cold sodium is the decisive parameter.

Computer codes, which analyse multicomponent, multiphase transient flow, need proper physical models to handle such phenomena. Codes such as the AFDM-code [1] and the IVA2-code [2] can be validated against small scale experiments. These experiments are performed in a simple and clearly defined geometry using easy to handle simulant materials. Several research groups performed experiments to study an expanding high pressure gas or vapor bubble in a vessel filled with a liquid, usually water. Moszynski and Ginsberg [3] gave a survey of the experiments performed up to 1980 with special attention to the phenomena of the liquid entrainment into the bubble. They reviewed experiments with and without heat transfer. Experiments without heat transfer or phase change like the present one, were performed by Theofanous and Saito at the Argonne National Laboratory (ANL) [4], by Rothrock et al. at the Massachussets Institute of Technology (MIT) [5], and Tobin and Cagliostro at SRI International [6] . In respect to the entrainment phenomena the experiments did not furnish consistent data. A number of mechanisms have been investigated to describe the observed entrainment. Entrainment through mechanisms of jet momentum transfer, Kelvin-Helmholtz instability and Rayleigh- Taylor instability are probably involved at some stage `of the expansion. Their conclusion was that the available models do not adequately characterise the available experimental data. More experimental data are needed with a better verification of reproducibility. This assessment is basically not different today, although some more experiments have been performed since [7,8,9].

This report consists of two parts. In part A the results of ten experiments are presented, results of the first three experiments (No.91,93,95) were published already before in Ref.12. In part B the results of calculations with the AFDM-code are presented for six of these experiments.

PART A: THE EXPERIMENT

EXPERIMENTAL APPARATUS, INSTRUMENTATION, PROCEDURE AND EVALUATION

The experimental apparatus was built by SRI International, California, and has been used for a first series of experiments at KfK [10]. The apparatus, the control of the experiment and the data acquisition and evaluation is described in detail in Ref.10. The main features shall be shortly described here again. Some changes have been made in the experiment and its evaluation in the second series. The experiment has been named SGI which stands for 'Schnelle Gas Injektion'.

Fig.A.1 shows all relevant dimensions of the experimental apparatus. The main vessel consists of an acrylic cylinder of 33 cm id., filled partially with water and air at 0.1 MPa. Inside, another smaller cylinder represents the shield tank of an SNR-type reactor. No internal structures have been simulated anymore in the second series. The pressure vessel situated below is filled with nitrogen at pressures between 0.3 MPa and 1.1 MPa. The two vessels are connected by a short tube, which is closed by two sliding doors and a thin metal foil above the doors. The objective of the doors is to open the flow cross section within a short time with the least possible disturbance of the flow. The doors are opened by exploding hydrogen-oxygen gas which drives two pistons toward the doors pushing them sideways in opposite directions. If both doors start moving at exactly the same instant the period between fully closed and fully open is only 0.5 ms. Experiments without the metal foil above the doors showed, however, an effect of the movement of the doors upon the water. Therefore a brass foil of 5 μm thickness was used to keep the water away from the moving doors. The foil breaks at the slightest pressure pulse at the beginning of the opening process.

Transient pressures are recorded at five positions. The pressures at three different radii at the vessel cover and in the lower pressure vessel are measured by piezoresistive transducers (Kistler type 4073). The signals are amplified by linear and logarithmic amplifiers. The pressure at the nozzle is measured by two piezoelectric transducers (Kistler type 60115007). The pressure measurements within the water have been abolished because the instrumentation stems disturbed the expanding bubble to much.

The flow inside the upper vessel is filmed with c. 7000 frames per second. By means of five mirrors pictures of two sides perpendicular to each other could be taken in the second series of experiments to check the symmetry of the flow. To track the movement of the water, two horizontal rows of red marker beads are placed at different vertical positions. These beads have a diameter of 4.8 mm and a density of 1026 kg/m^3. Initially, they rest on two thin wires. Due to the small density difference between beads and water and their small size the slip between water and beads is negligible.

All experiments were performed at room temperature. The water is degassed to an air volumetric fraction of 0.005-0.013. The experiment is controlled by a PDP-II/23 computer. After the pressure vessel and the explosive chambers have been filled manually with the respective gases, the pressure transducers are calibrated computer controlled. Then a time signal is generated which will be recorded on the tape recorder together with the transducer signals. After all systems have been automatically checked, the operator is prompted for a start command. This command starts a chain of signals for the high speed camera, the flash lights and the explosive ignition.

The signals of the pressure transducer and the photo diodes monitoring the door movement are recorded together with the time signal on a FM- tape recorder at a speed of 120 inches per second. For the digitisation of the data the tape is run at 1 inch per second which results in an effective digitisation rate of 200 kHz.

UNCERTAINTY OF THE RESULTS

The high pressure peaks are subject to errors in the order of 10%. Pressure pulses or oscillations above 40 kHz can also have errors in that order of magnitude. All pressure traces contain signals of the vibration of the vessel which originates from the door opening mechanism. Errors due to the digitisation are below 0.1% and electrical noise contributes less than 1% of the measured signal. Apart from the above mentioned extreme errors the uncertainty of the piezoresistive transducer measurements is ±2.6%. The uncertainty for the data obtained with the piezoelectric transducers is ±4%.

The time zero is defined by the beginning of the opening of the doors. The synchronisation with the film pictures is achieved by a small light flash and a reference signal written on the time channel. The discretisation time of a single frame is c. 0.15 ms. The uncertainty of the frequency of the frames, i.e. the time scale for the data obtained from the film, is 1.3%.

Not all optical distortions could be compensated. At extreme positions errors of ±2mm can still occur. The contour of the bubble surface and the position of the beads can be determined with an uncertainty of ±2mm due to the fuzzy picture.

It is difficult to quantify the total error in the calculated bubble volume and bead displacement volume (the method for the determination of the bubble volume has been changed in order to get vertical bulging of the bubble right). In addition to the digitisation errors there are the irregularities in the bubble shape, which means that the two-dimensional profile being digitised might not be representative of the three-dimensional bubble. This applies also to the bead motion. Since the absolute error is almost independent of time or size of the volume determined the relative errors at small volumes can be substantial. We estimate the uncertainty to be ±10% for volumes larger than 100 cm^3, and somewhat smaller errors for volumes above 1000 cm^3. Since the entrainment volume is determined from the difference between bubble volume and displaced water volume the error for this might reach ±30%.

EXPERIMENTAL PARAMETERS

The experimental parameters were the initial pressure with 0.3, 0.6 and 1.1 MPa, the diameter of the nozzle with 9 and 6 cm and the (inner) vessel diameter. In **Table A.1** nine successful experiments of the second series are listed. Tests No. 91, 93 and 95 were performed with the same geometry (**Fig.A.1**) as the tests of the first series described in [9], except for the above mentioned changes. In test No.21 the bottom of the vessel was changed (being flat) as shown in **Fig.A.2a**, but the inner cylinder representing the biological shield tank was present. This means a departure from the prototypical geometry but a simplification of the geometry and the bubble shape. A further simplification of the geometry and an important parameter for the bubble expansion is the removal of the inner shield tank in the tests No.29, 30 and 32 (**Fig.A.2a**). An entirely different geometry was used in tests No.33 and 37, where a cylinder with the same diameter as the nozzle diameter is added, which prevents a radial expansion of the bubble (**Fig.A.2b**). A similar geometry was used by Tan & Delhaye [9] , who performed 30 experiments at different pressures in a cylindrical and a square tube each.

EXPERIMENTAL RESULTS

Transient pressure

The only measured data are the transient pressures at different locations. All other data are derived from the high speed film recordings.

As a base case, useful for testing the computer codes, an experiment without water in the upper vessel was performed (SGI-11, not listed in Table A.1). The geometry was that of **Fig.A.1**, the initial pressure in the lower chamber was 0.6 MPa, absolute. The pressure histories at three locations are shown in **Fig.A.3**. At time t = 0 the doors begin to open and are fully open at t = 0.4 ms. Please refer to Fig. A.1 for the definition of the location of the pressure transducers.

In the first report on the SGI-experiments [10] many photographs of the expanding gas bubble were shown. Here the first stages of the process of a 1.1 MPa experiment (No.88) up to the water impact at the top cover are shown as contour plots of the expanding bubble, the vortex ring at the top of the inner cylinder, and the water surface at different times of the transient (**Fig.A.4**). The radial expansion of the bubble is constrained by the inner cylinder. At the upper edge of the inner cylinder cavitation occurs due to the high velocity at this sharp edge. A growing vortex ring is formed containing water vapor. At a later time it detaches from the edge and moves with the water flow. Finally it merges with the expanding bubble. Shown here are only two stages, one is shortly after formation of the vortex ring (No.5) and the other just before the merging with the bubble (no.15). The water surface is domed with a peak in the center. There it impacts the vessel cover first. Times after impact are not shown in the figure. The associated curve is therefore not shown. Depending on the initial pressure the impact area grows more or less toward the vessel periphery. The cover gas is correspondingly compressed.

Figs.A.5 through **A.13** present records of the transient pressures measured in the nine experiments. The nozzle pressure in test No.91 could not be measured during the first five milliseconds, because it was out of range. The pressure peaks resulting from the water impact at the cover are not always shown, but are documented by their maximum values and time of impact in **Table A.2**. Because of the doming of the water surface, the transducer at the center sees the impact first. The pressure peaks in the corner show the cover gas compression. The height of the pressure peaks corresponds with the initial pressure. In the low pressure experiment with 0.3 MPa (**Fig.A.7**, No.95) and the medium pressure experiment (0.6 MPa) without the shield tank (**Fig.A.11**, No.32) all three top pressure transducers record identical signals. Here the water does not impact the cover. On the other hand, in the experiment with the small cylinder in the center (**Fig.A.13**, No.37) which constrains the flow, the water impacts the top even at the low initial pressure of 0.3 MPa.

Bubble contour and bubble volume

All data discussed from here on are derived from the high speed photographs. The following figures show the bubble contours at different times up to the moment when

considerable cavitation at the upper edge of the inner cylinder sets in. Only every third frame is shown here, data were taken from each frame, however.

Both, the front view and the side view are shown for the experiments with the inner shield tank (No.91,93,95 and 21, **Fig.A.14-A.17**). Similar to the difference between the left and right hand side is the difference between the front view and the side view of the bubble. In the experiments No. 93 and 95 with 0.3 MPa and 0.6 MPa initial pressure a dimple at the centerline of the bubble was observed, looking from the front. The opening of the flow cross section by the two doors starts in the center with a non circular cross section, but with an oval with the long axis running from the front to the back side (s. [10]). Whether this is the reason for the different bubble shapes looking from the front and from the side is not clear. If the two doors do not open at exactly the same time, the bubble has an asymmetric shape as in test No.21 (**Fig.A.17**). The front view only has been taken in the experiments No. 29, 30, 32, 33 and 37, **Fig.A.18 - A.22**). The bubble volume, which is determined from these digitised shapes, should not depend on the view in order to be of general interest. All derived quantities, such as the bubble volume and the velocity were averaged from both sides (left and right) and, if available, from both views.

The bubble volumes Q_b were calculated by rotating each half of the bubble profile about the vessel center line and taking the average of both. This was done by discretisation of the bubble profile in vertical sections. Thereby all protrusions of the bubble are correctly considered. The volume of the cylindrical space between foil and upper edge of the nozzle was added to this visible average bubble volume (for No.91,93,95). In **Fig.A.23** the bubble volumes derived from both, the front view and the side view, are shown. The differences between front view and side view are small except for No.91. The results of an identical experiment (No.88) lie in between the results derived from both views. For further evaluations the average of both views was taken. **Fig.A.24** shows the bubble volumes versus time for all experiments. For a better resolution of the data points two different scales for the bubble volumes were chosen.

Fig.A.25 shows the bubble surface versus the bubble volume together with that of a hemisphere. Since the space within the nozzle above the foil counts as bubble volume but does not have a free surface, some of the data of tests No.91,93 and 95 lie below the curve relating to the hemisphere. The dashed line takes that effect into account and those data lie above that curve.

The displaced water volume, which is equal to the gas volume expanded from the nitrogen pressure source, was calculated from the bead motion in a similar fashion as the bubble volume. The bead positions starting at two different levels are shown in **Fig.A.26** at different times. Generally the agreement of the results from both rows of marker beads was good. The upper row of beads was positioned at the top of the inner cylinder. Therefore the beads close to the edge were drawn into the vortex and could not be used for evaluation anymore. All data shown are derived from the lower beads.

The displaced water volume was always smaller than the bubble volume at the same time. The difference between bubble volume and the displaced volume is the volume of liquid entrained within the bubble. These entrainment volumes Q_e are plotted as a function of time in **Fig.A.27** together with a polynomial curve fit of second order. As mentioned before, the error band for the entrainment volume is much wider, the scatter of the data larger, because two large values are subtracted to determine the

entrainment. For a better resolution of the data points two different scales are used in Fig.A.27 through A.31 and Fig.A.36 and A.37.

In the following analysis we try to find a relation between the entrainment and geometric or other global parameters, such as the gas exit velocity. Relations to local parameters, such as the local interface velocity, would be more desirable for the code modelling, but it is impossible to derive local entrainment rates from the experiments.

The entrainment volumes Q_e are plotted as function of bubble volume Q_b in Fig.A. 28 and as a function of bubble surface in Fig.A.29. Most of the data fall into a narrow band, which suggests that the entrainment does not depend on the pressure, within the applied pressure range. Of course, the results of No.33 and 37, which were similar to an expansion in a tube, do not fit in. The data from the tests without an inner cylinder (No.29,30 and 32) show a larger deviation, but no specific trend depending on pressure or nozzle size can be derived. Several runs of each test would be necessary to prove any such trend.

For comparison the range of the SRI results [6] is shown, which showed a larger scatter. Since the MIT experiments [5] were performed in a planar geometry a comparison with those is not justified. The authors of the ANL experiment [4] stated that entrainment is negligible for their Nitrogen tests.

Expressed as a fraction of the bubble volume the relative entrainment Q_e/Q_b approaches a constant value of 20% for large bubbles (Fig.A.30) in the cases with an inner cylinder (No.21, 91, 93 and 95). Without this constraint the bubbles grow larger and the relative entrainment drops to 10 - 16% (No.29, 30, 32).

The entrainment volume related to the bubble surface represents an entrainment thickness with a water volume fraction of 100%, contrary to the physical process, where the water is distributed within the bubble at lower water volume fractions. This artificial entrainment thickness is shown in Fig.A.31 versus the bubble volume. Again, for the tests with the inner cylinder the entrainment thickness approaches a constant value of 6 cm, while the other tests show a variable thickness between 4 and 8 cm.

COMPARISON OF EXPERIMENTAL DATA WITH ENTRAINMENT MODELS

Theoretical entrainment models (for a review see e.g.[3]) employ the entrainment velocity and the acceleration of the bubble front as most important parameters. Tan and Delhaye [9] performed a series of experiments in a round and a square tube similar to our experiments No.33 and 37. They obtained an almost uniform acceleration of the water front in each test during the time of observation. The velocity of entrainment was determined by

$$v = \frac{d}{dt}(x_L - x_U) \qquad (1)$$

where x_U and x_L denote the positions of the upper water interface and the apex of the lower interface (bubble surface). Also the entrainment velocity was found to be uni-

form in each test. Thus they obtained one data point for each test and found a relation between the rate of entrainment and the acceleration in the round tube:

$$v = 0.35(aD)^{1/2} \qquad (2)$$

where D is the diameter of the circular section. The data obtained in the square section did not obey Eq.(2). **Fig.A.32** shows the data from Tan and Delhaye together with results of the tests No.33 and 37.

The interpretation of these results must be done with great care. First of all, the definition of the entrainment velocity or rate by Eq.(1) is very specific; it is not the water inside the visible bubble as we defined it. The entrainment defined by the difference of the positions of the top of the water interface and the top of the bubble interface is quite large compared to the conventional definition which is the difference between the bubble volume and displaced water volume (**Fig.A.33**). Taking the position of the apex of the interface as the governing parameter is somewhat arbitrary. Moreover, the acceleration is not the local acceleration of the interface. The application of these results to an expanding bubble or jet is therefore not possible.

Secondly, to determine the acceleration of the interface, means to fit data points taken from the high speed film by a second or third degree polynomial and form the second derivation. As Tan and Delhaye pointed out, it is not possible to decide which kind of polynomial fits the data better (Fig.4 in [9]). **Fig.A.34** demonstrates this fact for our test No.33. Except near the first two points at the lower left end of the curve for the water position the lines of the second and of the third order polynomial cannot be distinguished from each other. However the resulting water velocity functions are clearly different and the acceleration varies by more than a factor of two in case of the third order polynomial versus a constant value for the second order fitting. The entrainment rate is determined by derivation of the water thickness $(x_U - x_L)$ which is shown in **Fig.A.35**. A linear function clearly does not fit the data, therefore the entrainment rate cannot be a constant. Tan and Delhaye chose a constant acceleration and consequently had to use a constant entrainment velocity also, in order to be consistent with the theory.

Another free parameter is the way of determining the co-ordinate x_U. Taking a single point at the apex of the bubble interface is certainly not the best choice, as can be seen in Fig.A.21 and A.22. The SGI-results in **Fig.A.32** were obtained by taking the average of the data in a radius of 20 mm around the tube axis. If this radius is varied between 0 and 30 mm the velocity varies by approximately 2 m/s. Larger radii change the results entirely.

The entrainment mechanism in the expanding bubble emerging from a nozzle is more complicated than the one-dimensional case. It may be governed by the following mechanisms:
1. Jet entrainment
2. Kelvin-Helmholtz instability
3. Rayleigh-Taylor instability

The contribution of each mechanism to entrainment probably varies during the transient and it is impossible to find any one simple relation for different geometries.

According to Ricou and Spalding [11] the first mechanism can be estimated by a relation between the volume rate of the entrained fluid q_e and the gas jet q_g

$$q_e = C\frac{L}{D}\left(\frac{\rho_g}{\rho_l}\right)^{1/2} q_g \qquad (3)$$

with ρ_g and ρ_l the density of the gas and liquid, respectively, D is the diameter of the jet, L the effective entrainment length and C a constant.

The volumetric entrainment rate q_e was determined by the derivation of a second polynomial fit of the entrainment volume shown in **Fig.A.30**. The velocity of the gas v_g at the nozzle can be calulated from the displaced water volume. The gas velocity at the nozzle versus time is quite different for the different tests (**Fig.A.36**). However, **Fig.A.37** shows a good correlation between q_e and the gas velocity v_g for the series No.91, 93 ,95 and No.33 and 37. For test No.21 which had a different nozzle diameter and for the tests with the larger vessel diameter the relation between q_e and v_g is different and no simple parameter, such as L/D can force the curves to converge. Equation (3) is valid for a steady state gas jet issuing into a large body of another gas. For obvious reasons the applicability of the model to the bubble expansion is questionable, as has been pointed out already by Moszynski and Ginsberg [3].

Based on the Rayleigh-Taylor instability the model by Corradini estimates the entrainment rate by

$$q_e = 4.65 A_p \left(a\lambda_{cr}\right)^{1/2} \qquad (4)$$

where A_p is the projected area of the interface and λ_{cr}, the minimum unstable wavelength given by

$$\lambda_{cr} = 2\pi\left(\frac{\sigma}{(\rho_l - \rho_g)a}\right)^{1/2}. \qquad (5)$$

To put this model to a test the acceleration of the water interface at the top of the bubble was determined in a similar fashion as for the tube experiments No.33 and 37 using a second degree polynomial. The plot of the entrainment rate versus the acceleration (**Fig.A.38**) shows that Eq.(4) cannot hold unless the acceleration or the parameter A_p is variable. However, the acceleration is not an increasing function, except for the tube experiments No. 33 and 37. From Eq.(4) we can determine the area A_p which would reproduce the measured entrainment rates q_e. The diameter D of this area is listed in the last column of **Table A.3**. These values lie in the range of the observed bubble diameters as can be seen in Figs.A.14 to A.20, but it would be difficult to use Eq.(4) as a predictive tool since the parameter A_p is not defined precisely. Again, as for the correlation between entrainment rate and gas velocity, no simple geometric parameter can make all results obey a single correlation. Only a combination of entrainment models can describe the expansion of a gas into a liquid correctly.

For modelling this process in a computer code the local entrainment should be a function of local parameters, such as local velocity or acceleration. From the experiment only the total entrainment is known, but local interface velocities and accelerations

can be determined. We tried several methods to correlate those data. The correlations contained up to three coefficients, which had to be chosen to fit the experimental data. No single set of coefficients was found to apply for all experiments. Moreover, the number of experiments was not sufficient to test such lengthy correlations.

CONCLUSION OF THE EXPERIMENTAL WORK

Nine different experiments on a high pressure gas injection into a liquid pool are described and the results are documented. The transient pressure traces are a valuable benchmark test for computer codes. The evaluation of the high speed films yields integral entrainment rates as functions of time or other experimental parameters. The data were compared to three entrainment models and some agreement was found. But not all experiments can be described by a single model. Codes containing entrainment models can be validated by these results, models can be refined.

PART B. RECALCULATION WITH THE COMPUTER CODE AFDM

The Advanced Fluid-Dynamics Model (AFDM) is a Eulerian, three-velocity-field, multiphase, multicomponent fluid-dynamics computer code [13] that was developed at the Los Alamos National Laboratory with participation of the Kernforschungszentrum Karlsruhe. It has been designed to test approaches for investigating severe liquid-metal cooled reactor accidents, i.e. highly transient flow in pool geometry. A time-factorization approach is used to differentiate intracell modelling from convection between the two-dimensional cells of the Eulerian grid in cylindrical co-ordinates. A semi-implicit procedure is used for the inter-cell solutions with a pressure iteration that is driven by the discrepancy between the cell pressures and the equation-of-state pressures. A higher-order differencing method is available to reduce numerical diffusion. Convection of interfacial areas is performed to follow phenomenological histories. These convection equations include interfacial area source and loss terms based on detailed models for the splitting and coalescence of bubbles and droplets [14]. The momentum coupling between the phases is described by a generalized model [15] that is valid for all flow regimes. Except for the choice of the continuous phase, the constitutive relationships for the momentum transfer are thus independent of flow regimes.

A selection of six SGI-experiments was recalculated. AFDM pressures and volume fractions of phases were recorded and compared with experimental data. In all cases, the higher-order differencing option was used because it was known from AFDM tests that donor-cell differencing would produce excessive numerical diffusion at the sharp interfaces observed in the experiment. The AFDM code required a memory of 800.000 words and the ability to do vector arithmetic to achieve running times of less than 10 minutes on a Siemens/Fujitsu VP50. A maximum of 20 radial cell columns and 36 axial cell rows was used. For most practical purposes, the number of cells was

smaller. Calculations were performed at the Los Alamos National Laboratory and at the Kernforschungszentrum Karlsruhe, explaining some differences in the plot formats.

All calculations start from initial conditions defined by the SGI system at rest. The time is set zero for the beginning of the sliding door opening. In AFDM, the finite opening time of the doors which is about 0.5 ms, is not modelled. Instead, the doors are supposed to open instantaneously at time zero.

RECALCULATION OF SGI-33

SGI-33 has a very simple geometry. Nozzle diameter and the diameter of the inner vessel are equal. Therefore, the lower test section is a straight cylindrical tube which is a good testbed for code performance. Two key questions were addressed during the recalculations: first, how large is the numerical diffusion at the lower gas-water interface, and second, what is the influence of the wall model of the code on the volume fraction profiles. **Fig. B.1.** shows a cross section of the right side of the AFDM model in cylindrical co-ordinates (r, z) with air velocity vectors at 3.3 ms. There are 20 radial and 36 axial cell rows. There is always a vapor component in each of the cells, even if the cell is filled with only water. In this case, the residual small vapor contents is to represent nucleation sites, and has the same velocity as the liquid phase. From z = 0 to z = 0.26 m, the pressure vessel is filled with nitrogen at 11 bar pressure. The pool top interface at z = 0.46 m is clearly visible because of the abrupt change of velocity directions. The water and the cover gas are initially at ambient pressure.

Fig. B.2. shows the experimental pressure (dotted line) and the AFDM recalculation (solid line) of the gas pressure is the pressure vessel. AFDM does not model the slight pressure oscillations during the first 6 ms. **Fig. B.3.** shows the pressures at the top center, both of the experiment and the code using the same notation as before, **Fig. B.4.** shows the pressures at the top middle, and **Fig. B.5.** at the top corner. There is a time lag of AFDM pressures between 0.5 and 1 ms which can be explained by the lack of details in modelling the opening of the sliding doors and the liquid-gas interfaces. The agreement between experimental and code pressure is judged to be very good which is a necessary condition for the analysis of code performance at the lower gas-liquid interface. The lower gas-liquid interface is accelerated upwards starting at an elevation of 0.26 m, and moves through the tube which extends up to 0.43 m. Its history is of specific interest.

Fig. B.6. shows the vapor fluid fraction which is the volume fraction of vapor with respect to the cell volume fraction available to the fluid flow. As time progresses, both gas-liquid interfaces move upwards. The lower interface which moves within the tube of 9 cm diameter is smeared over several cells. This looks similar to the experimental smearing of the interface through entrainment although the reason is the numerical diffusion caused by the space discretization. We shall discuss this problem below. **Fig. B.7.** shows the cross section of the center part of SGI-33 with contour lines of constant vapor fluid fractions. The figure shows almost straight parallel lines at the lower gas-water interface indicating that the profiles of **Fig. B.6.** are valid for all radii. In the cells adjacent to the wall, a slight influence of the wall friction is visible. Close to contour line "zero", there is the interface between pure water and the two-phase region. In the experiment, this interface can easily be observed because pure water is

transparent, but the two-phase region is not. To reduce inconsistencies due to the interpolation procedures of the plot programme, the water-two-phase interface is defined by the contour line of a vapor fluid fraction of 0.07. With this threshold condition selected, **Fig. B.8.** shows three frames at times between 2.7 ms and 5.5 ms comparing the AFDM contour with the experimental interface between water and the two-phase region. Neglecting the differences in shape of the contour lines, AFDM produces a history of the interface motion which yields average velocities and mass flow consistent with experimental data. However, the experimental contours are clearly influenced by he friction at the wall. In AFDM, only the cells adjacent to the wall are influenced by wall friction. There is no momentum exchange between cells perpendicular to the fluid velocity. This exchange, based on turbulent diffusion of momentum, is apparently a dominant physical phenomenon in the experiment. The lack of an AFDM model for such an exchange decreases the code validity especially close to structures and walls. The lack of a turbulence model cannot be compensated by an artificial increase of the wall friction factor. **Fig. B.9.** shows water fluid fraction contour lines for an AFDM calculation with an increased friction factor. Although the contours show a slower progression of the two-phase bubble in the cells adjacent to the wall, the profile in the tube center is not affected. Instead, there is an overcompensation of momentum exchange through mass convection in the row of cells next to the wall cells leading to a speed-up of the interface at that point which does not reflect the experimental observations.

Comparing AFDM calculations with nominal wall friction factors, the question of the magnitude of the numerical diffusion has still to be answered. Therefore, the calculations were performed with four different driving gas pressures, from 0.5 MPa to 4.4 MPa, resulting in different accelerations of the water column inside the tube. **Fig. B.10.** shows four vapor fluid fractions along the center line at exactly the same location. Because of the different accelerations, the times at which the gas-liquid interface reaches this location are different, and so are the velocities. From **Fig. B.10.** it is obvious that the numerical diffusion yields exactly the same volume fraction profiles, except for slight changes close to void fractions of 0.95 and above. The data of these four calculations plus an additional AFDM run with doubled axial cell length are condensed into **Table B.1.** The initial gas pressures drive the liquid upwards through the tube. At 0.4 m elevation, accelerations are between 3500 m/s^2 and 30600 m/s^2. The void gradient depends only on the cell length. Because of the different accelerations, the velocities at 0.4 m are different. Finally, the product of void gradient times cell length is about constant for all cases. That means that the gas-liquid interface is smeared by numerical diffusion over three cells, independent of velocity and acceleration. This result changes substantially, if donor-cell differencing is used in AFDM instead of second-order differencing. Since donor-cell differencing is hardly used, we have not run AFDM to quantify the magnitude of the diffusion. As we shall see below, higher order or second-order differencing is mandatory for producing a good agreement between experimental results and AFDM.

THE FIRST GROUP OF RECALCULATIONS.

The first group of recalculations covers SGI-29, SGI-30, and SGI-32. For all three experiments, the water pool and the cover gas plenum was identical. There were no internal structures inside the water pool. SGI-29 and SGI-32 had a nozzle diameter of

9 cm, SGI-30 of 6 cm. The high pressure nitrogen volume was identical in all cases, the nitrogen pressure was either 0.6 or 1.1 MPa.

RECALCULATION OF SGI-29

The nitrogen pressure of SGI-29 was 1.1 MPa. **Fig. B.11.** shows the right half of the cylindrical AFDM grid with 16 radial cell columns and 22 axial cell rows. The heavy lines represent boundaries with regions of uniform initial conditions. The uppermost four cell rows represent the cover gas, the next ten rows the water pool, the center 5 x 3 cells the air gap between the diaphragm and the sliding doors, the 11 x 6 cells to the right of the air gap represent the solid structure where no fluid flow is possible, and the lower cells represent the pressure vessel with the high pressure nitrogen. The AFDM pressure vessel has the same volume as in the experiment, its shape, however, is projected onto the 16 x 22 AFDM grid, with a contour change that will not influence the fluid-dynamics in the volume above the diaphragm.

Fig. B.12. shows the pressures inside the pressure vessel. The AFDM cell pressure (solid line) is compared to the reading of the SGI pressure transducer (dotted line) at the equivalent location. Phase and amplitude compare well which indicates that the whole energetic is modelled correctly.

Fig. B.13. shows the pressures at the periphery of the nozzle above the sliding doors. Phase and amplitude compare well for times earlier than slug impact at the vessel head (at 7 ms). A phase shift of up to 2 ms can be observed afterwards. The nozzle pressures are rather sensitive to the motion of the pool following the impact on the vessel head and the cylinder periphery. After 7 ms, part of the gas-water mixture is forced down through the nozzle into the pressure vessel. This motion is a function of the impact and the development of a complex two-phase mixture after the impact. There is a lack of detail in AFDM modelling for this late phase of the transient. First, the impact is not modelled precisely because the leading water edge which is a sharp interface in the experiment is smeared due to numerical diffusion, although higher order differencing has reduced the magnitude of the diffusion considerably. The diffusion increases slightly with time. Diffusion can be reduced by defining smaller computational cells. This method will be used later. Second, AFDM lacks a model of cell-to-cell momentum coupling by momentum diffusion. Consequently, there is also a lack of a turbulence model. Turbulent dissipation, however is likely to be important after slug impact.

Fig. B.14. shows the pressures at top center, which is a location at the center of the vessel head. Although a rather course mesh of cells has been used for the cover gas region, phase and amplitude of the AFDM calculation compare well with the experimental reading. The experiment shows a very narrow pressure peak because of the impact of the smooth water surface on the vessel head. In AFDM, the cell pressure of the cell next to the rigid wall is recorded. The pressure peak is broader because of the finite volume of the cell and because of the fact that the sharp water surface is smeared by numerical diffusion. Additionally, the AFDM pressures are static pressures, whereas the experiment reads total pressures. In AFDM however, the cell density at impact is considerably smaller than that of pure water, and the dynamic pressure would not contribute much to the total pressure.

Fig. B.15. shows six frames of SGI-29 contours at different times. A two-phase bubble is emerging from the nozzle into the liquid water pool. The dotted lines show the interfaces between pure water and the two-phase bubble as observed in the experiment. The AFDM contours (solid lines) are produced the same way as those of SGI-33. The explanation for the contour line selection is the same. The contour lines close to a void fraction zero are as close to the experimental interface as the post processor can interpolate. The two contour lines of **Fig. B.15.** represent void fractions of 0.04 and 0.07. The good agreement between experimental and AFDM contours indicate that AFDM fluid motions are calculated correctly. If we recall from SGI-33 that AFDM numerical diffusion was independent of the velocity and the acceleration of the interface, but only dependent on the size of the computational cells, then the steep gradient of the AFDM interface extends over 54 mm (3 times the axial cell length) in axial direction, and 30 mm (3 times the radial cell width) in radial direction. There may, however, be some mass diffusion beyond the three cells, depending on the progress of the interface when it advances into new cells.

To demonstrate the effects of cell sizes, two AFDM-runs were performed for SGI-29 with identical input parameters, but two different radial mesh cell sets. **Fig. B.16.** shows the void fraction profiles at six different elevations for the base calculation which had 16 radial cells, most of which had a radial width of 0.01 m. Curves number 4, 5, and 6 show the profiles of the top part of the emerging bubble at elevations of 0.364, 0.382, and 0.4 m, respectively.

Fig. B.17. shows the same profiles produces by an AFDM-run with only 5 radial cells which were 0.04 m wide. The smearing over the radial length has increased substantially. A commercial computer program has been used to generate 2D pictures from AFDM data using a geostatical technique to calculate the auto correlation between data points and producing a minimum variance unbiased estimate. This is believed to be the most accurate gridding method. A grid of 51 x 41 lines has been used. **Fig. B.18.** shows the contour lines of vapor volume fraction 0.07 and 0.93 for the base case (solid lines) and the reduced radial cell number (broken lines). The contour lines represent the beginning and end of the two-phase region. The mass diffusion of the broken-lines is more pronounced in radial direction. This has a slight effect on the distribution of water, and therefore the two-phase bubble extends further upwards. However, the top of the pool, represented by the two horizontal top contour lines, is barely affected.

Fig. B.19. shows the pressures in the pressure vessel and at the top center for both cases which only differ slightly. The pressure vessel values (curves 1) are almost identical, only the top center pressures (curves 2) deviate close to the water slug impact on the vessel head. The solid lines of the base case shows a single peak as it was measured in the experiment. The broken line shows two peaks which are functions of the excess radial motion due to numerical diffusion. The second pressure peak follows the impact of water at the top radial corners which sends a pressure wave back to the top vessel center. In the base case, the impact on the vessel corner comes earlier, and it only broadens the single pressure peak.

The numerical experiment with a course radial cell grid shows that the good agreement between experimental and AFDM bubble shapes can only be achieved if the cell sizes are not too far from what has been chosen as the base case. However, changing the cell sizes by the order of 100 % would not influence contour lines beyond the uncertainties imposed by the gridding method of the commercial plot programme.

Therefore, it is impossible to infer the amount of the entrainment from the gradients of numerical diffusion produces by AFDM. It is only possible to estimate the order of magnitude of the entrainment.

RECALCULATION OF SGI-32

The nitrogen pressure of SGI-32 was 0.6 MPa. The AFDM cell grid of SGI-29 as shown in **Fig. B.11.** was used, and data were processed the same way as before.

Fig. B.20. shows the pressures inside the pressure vessel. For the first 7 ms, the AFDM pressure (solid line) compares well with the experimental reading (dotted line). The AFDM impact of the water pool on the vessel head comes later than that in the experiment. Therefore, the minimum in **Fig. B.20.** is observed later for the AFDM data. **Fig. B.21.** shows the nozzle pressures. The experimental (dotted) pressure peaks between 6 and 8 ms may be a result of background noise. As in **Fig. B.20.**, a phase shift is noticeable between AFDM and experimental data. The AFDM oscillations are delayed, and the amplitude is reduced.

Fig. B.22. shows the pressures at top middle. The impact at maximum pressures is later with AFDM compared to the experiment. It is also substantially lower. The experimental maximum is 1.9 MPa, the AFDM maximum is 1.5 MPa. The reasons for the discrepancy can be explained by looking at the two-phase bubble contours. **Fig. B.23.** shows six selected frames with the AFDM water contour lines (solid lines) and the experimental contours at the two-phase bubble interface to the liquid water pool (dotted lines). Although the differences between experimental and AFDM contours are not great, there is a noticeable change from SGI-29 (**Fig. B.15.**) to **Fig. B.23.**. In **Fig. B.15.**, the shape of the bubble top was flat for both, AFDM and the experiment. In **Fig. B.23.**, the AFDM contours are very similar to those of **Fig. B.15.**, but the experimental bubble has a more pointed top indicating that the experimental axial movement is slightly more dominant than the radial movement. The difference in bubble shapes lead to differences in the pressures. The faster axial advance of the experiment leads to an earlier impact on the vessel head. If AFDM numerical diffusion is very similar for both, SGI-29 and SGI-32, then less entrainment of SGI-32 affects the differences of experimental and AFDM pressure records.

RECALCULATIONS OF SGI-30

SGI-30 is similar to SGI-29, but with a reduced nozzle diameter of 6 cm. Therefore, the discharge of gas into the water pool is more confined to the center axis of the pool which has an effect on both, the pressure histories and the bubble shapes.

Because of the different nozzle size, the grid of cells of **Fig. B.11.** was changed to include 20 radial cell columns and 36 axial cell rows. The finer mesh set reduces numerical diffusion by 30 % to 60 %, a reduction which should have only minor effects on the calculation of the bubble shapes, as explained for SGI-29.

Fig. B.24. shows the comparison between AFDM pressure (solid line) and experimental pressure (broken line) in the pressure vessel. Both compare well except

that AFDM oscillation frequency and amplitude are slightly different with respect to experimental values. **Fig. B.25.** shows the nozzle pressures in the same notation. AFDM pressure changes are a fraction of a millisecond earlier. **Fig. B.26.** shows the pressures of the top center. The AFDM pressure peak comes slightly later, and a second peak is calculated after the slug impact at the upper corners. **Fig. B.27.** shows the pressures in the top corner. Here, the AFDM pressure deviate most. This is caused by the shape of the AFDM pool surface during the late transient.

The AFDM pool surface is domed in the middle, because AFDM axial bubble expansion is overestimated. This may be due to the lack of a turbulence model which would otherwise couple momentum in radial direction. The experimental pool surface is much flatter. The air is discharged through a rather small nozzle. However, the two-phase mixture quickly broadens, and water in some radial distance is coupled to the axial movement by diffusion of momentum. Therefore, SGI-30 demonstrates more clearly the differences between the experiment and AFDM.

Fig. B.28. shows four selected frames with the experimental interface (dotted lines) between the two-phase bubble and the pure water pool. Two AFDM contours at void fraction of 0.04 and 0.10 are given for comparison. AFDM axial penetration is overestimated, and reduces considerably the distance between bubble interface and pool surface at later times. Therefore, the AFDM bubble even speeds up increasing the discrepancy with respect to experimental contours.

THE SECOND GROUP OF RECALCULATIONS

The second group of recalculations is that of SGI-91, SGI-93, and SGI-95. **Fig. B.29.** shows the AFDM mesh set for these three experiments. Inside the water pool, there are now two specific structures which model components of the internals of a large sodium-cooled nuclear reactor. The small ring at the nozzle of the pressure vessel represents the upper part of the radial breeder zone, the long concentric cylindrical structure close to the vessel wall represents the biological shield. These structures have a substantial effect on the way the two-phase bubble penetrates the water pool, and on the shape of the pool surface.

RECALCULATION OF SGI-91

This is the experiment with the highest initial pressure (11 bar) of this group of experiments. To identify the effects of the new structures, it can be compared to SGI-29 where AFDM results were very close to experimental values. Several AFDM runs were performed. The first run was done with the standard grid of **Fig. B.29.**, of which the bubble contours are presented here. The following runs were done with a finer mesh set at the top of the pool. This was done to improve on calculating the pressure history of the top center.

Fig. B.30. shows the AFDM top center pressure (solid line) compared to the experimental value (broken line). It shows two AFDM pressure peaks, the first at the

experimental impact time, and a second after the impact of the AFDM pool surface on the radial top corner (see **Fig. B.33.**). The time between the two peaks depends on how much the AFDM pool surface was domed in the middle. A flat pool surface would produce only one peak. The experimental curve shows a very small second pressure peak at 8.6 ms indicating that the experimental pool surface is domed, but that the pressure wave following the impact at the top corner is reduced substantially on its way to the top center.

The AFDM pressure curve can still be improved. **Fig. B.31.** shows an additional calculation with all input parameters unchanged, but an artificial volume fraction of 10 % small gas bubbles in the water pool. This void fraction slows down the propagation of the pressure wave after the opening of the door to the pressure vessel. As the pressure propagates, the gas in the water is compressed which leads to an artificial additional mass exchange between cells. The net result is a minor difference in fluid movement inside the pool, a dampening of pressure waves, and a higher first AFDM pressure peak together with a lower second pressure peak which comes as late as for the base case of **Fig. B.30.**. In **Fig. B.31.**, the second AFDM pressure peak is at 8.65 ms rather than at 8.8 ms of the experiment. However, for AFDM and the experiment, the time lag between first and second peak is 1.2 to 1.3 ms. Although the dissipation of pressure waves is now increased in AFDM, the experiment shows an even larger dissipation at the pool top during slug impact.

The additional pressures calculated with the AFDM base case for SGI-91 are shown in **Figs. B.32.** and **B.33.** with the solid lines for AFDM and the broken lines for the experiment. There is a good agreement for both pressure histories. The lack of AFDM dissipation drives the top corner pressure beyond that reported by the experiment.

Fig. B.34. shows six selected frames with the two-phase bubble contours of the experiments (dots) and the first AFDM run (solid lines). AFDM contours show a trough-shaped top but experimental contours do not. The AFDM bubble is also slightly faster. Both observations are similar to those for SGI-32 (**Fig. B.23.**) but the discrepancies are larger for SGI-91.

RECALCULATION OF SGI-93

The geometry is the same as that of SGI-91, but the initial pressure in the lower gas vessel is 6 bar instead of 11 bar. The results of AFDM pressure histories are shown in **Figs. B.35.** to **B.38.**, with broken lines for experimental data and solid lines for AFDM. The differences between both set of curves is similar to those of SGI-91 and the same explanations apply.

However, the experimental contours of the expanding two-phase bubble are different to those of SGI-91. **Fig. B.39.** shows a set of six selected frames with dots for experimental contours, and solid lines for AFDM. Both shapes are similar, especially for the first 4 ms. Only later, after 6 ms, the experimental interface becomes domed in the middle whereas the AFDM contour remains trough-shaped at the top. Apparently, the code does not result in any different contour shapes if the driving pressure is almost doubled. But the experimental interface is flatter for the low pressure case, and its top is smoother for the high pressure case.

RECALCULATION OF SGI-95

The geometry is the same as that of SGI-91 and SGI-93. The initial pressure in the lower gas vessel is only 3 bar. Therefore, the distinctive pressure peak at slug impact at the top center has changed to a mild increase of all pressures at the vessel top. **Figs. B.40.** to **B.43.** show AFDM pressures (solid lines) and experimental pressures (broken lines). **Fig. B.40.** shows that the initial pressure of the experiment was slightly higher than that given for AFDM. Therefore, the experimental pressure of **Figs. B.41.** to **B.43.** rise to slightly higher peaks. The peaks also come slightly earlier which should not be due to the different initial pressures. By and large, the two sets of histories are similar.

Fig. B.44. shows six selected frames of the contours of the expanding two-phase bubble with solid lines for AFDM and dots for the experimental data. As for SGI-93, the shape of the AFDM contours is barely affected by the driving pressure, however, experimental contours are quite flat at the top with many "wrinkles". Even at late times, the doming in the middle does not extend beyond the outer edges of the otherwise trough-shaped center front in the experiment.

CONCLUSION OF THE AFDM CALCULATIONS

Seven SGI experiments, belonging to three groups of similar geometry, were recalculated by the two-dimensional AFDM code. For the two groups of gas discharge into a large open pool, the calculational results agreed well with the experimental data.

For the gas discharge into a straight tube (SGI-33), the deficiencies of the code were more pronounced. Here, it was found that the lack of a turbulence model cannot be compensated by an artificial increase of the wall friction factor. It was found that the numerical diffusion of the interface between water and gas inside the tube was independent of the interface velocity or acceleration. Using a higher order differencing method for space discretization, the interface was always smeared over three computational cells. This differencing method proved to be necessary to track the sharp interfaces.

The lack of a turbulence model is believed to be also a reason for the small discrepancies between AFDM and the experiments of large pool discharge. The pressure histories at water impact on the vessel head showed that the AFDM water surface was more domed in the middle. This leads to a different impact time at the vessel head corners. This discrepancy can be reduced by introducing an artificial void into the water which results into a more realistic momentum coupling perpendicular to the water velocity, because the compressibility of the void introduces additional mass and thus momentum exchanges with the neighbouring cells. Since the smearing of AFDM interfaces depends on the cell size, it was proven that the change of the radial cell size by more than 100% had an effect on the results. For all large pool recalculations, the shape of AFDM expanding gas bubbles were similar to each other, with either a flat or a trough-shaped bubble top. Only for SGI-30, the high pressure injection with a small nozzle diameter, the AFDM bubble was almost round at the top.

Since numerical diffusion of AFDM interfaces is about the same in radial and axial direction, the shapes probably depend heavily on the way the water moves. On the other hand, experimental results additionally depend on the entrainment processes that may vary with time and location. Good agreement of AFDM bubble shapes with the experiment was found for SGI-29 and SGI-32. For SGI-32, the experiment yields a bubble top which is almost round. For SGI-30, both bubbles are shaped similarly, but AFDM yields a faster axial penetration, probably because of a lack of momentum coupling to the sides. For SGI-91, the experiment shows a pointed bubble top which is different to the AFDM results. SGI-93 and SGI-95 show good agreement of bubble contours, but in the experiment, there is always a little peak on the center top of the bubble.

Summarizing these observations, the biggest discrepancies are found for the high pressure bubbles. The experimental bubbles are generally more pointed at the top. The discrepancies are too small and inconsistent to allow a general conclusion, except that the experimental entrainment is of the same order of magnitude as the smearing of AFDM bubble interfaces by numerical diffusion with a higher order space discretization method.

REFERENCES:

1. W.R.Bohl et al., Computational Methods of the Advanced Fluid Mathematics and Computation, Paris (1987), Vol.3,p.1625

2. N.I.Kolev, IVA2 Verification: Expansion Phase Experiment in SNR Geometry, First World Conference on Experimental Heat Transfer Fluid Mechanics and Thermodynamics, Dubrovnik (1988), also KfK-Report 4310, 1988

3. J.R.Moszynski, T.Ginsberg, Liquid Entrainment by an Expanding Gas or Vapor Bubble - A Review of Experiments and Models, Report BNL-NUREG-2B343, Brookhaven National Laboratory, USA (1980)

4. T.F.Theofanus, M.Saito, The Termination Phase of Core Disruptive Accidents in LMFBRs, Proc. of the Int. Meeting on Fast Reactor Safety Technology, Seattle (1979),Vol.III,p.1425

5. R.A.Rothrock, M.S.Kazimi, W.M.Rohsenow, Hydrodynamic Characteristic of a Gas Blowdown into a Two-dimensional Liquid Pool, Nuclear Engineering and Design 71, (1982) p.241-250

6. R.J.Tobin, D.J. Cagliostro, Effects of Vessel Internal Structures on Simulated HCDA Bubble Expansions, Technical Report No .5, SRI International (1978)

7. K.Küfner et al., Model Experiments for the Post disassembly Expansion Phase in LMFBRs and their Use for Code Validation. Proc. of the LMFBR Safety Topical Meeting, Lyon, France (1982) p. IV-99 .

8. W.Schütz et al, Wasser-Simulationsexperimente zum instantanen Quellterm beim schweren Brutreaktorstörfall, KfK 4249, (1987), Kernforschungszentrum Karlsruhe

9. M. J. Tan and J.M. Delhaye, An Experimental Study of Liquid Entrainment by Expanding Gas. J. Fluids Engineering, Vol. 109, pp.436-441, Dec. 1987.

10. D.Wilhelm, M.Kirsthaler, Versuchsanlage zur schnellen Gasinjection in einen wassergefüllten Behälter, KfK 4321, (1987), Kernforschungszentrum Karlsruhe

11. F.P. Ricou and D.B. Spalding, Measurements of Entrainment by Axisymmetrical Turbulent Jets. J. Fluids Mechanics, 11, p. 21 (1961)

12. L. Meyer and M. Kirstahler, Experimental Investigation of the Fluid Dynamics of a Gas Jet Expansion in a Liquid Pool, First World Conference on Experimental Heat Transfer, Fluid Mechanics and Thermodynamics, Dubrovnik, Yugoslavia, Sept. 4-9 (1988), Elsevier, New York, p. 864-871

13. W.R.Bohl, D. Wilhelm, The Advanced Fluid Dynamics Model Program: Scope and Accomplishment, Nuclear Technology, Vol.99, pp.309-317, 1992

14. D.Wilhelm, W.R.Bohl, The AFDM Models for Interfacial Areas and Their Test on Out-Of-Pile Experiments, Proc. of the Int. Fast Reactor Safety Meeting, Snowbird, August 1990, Vol.IV, 437-447

15. J.Berthier, D.Wilhelm, W.R.Bohl, AFDM Heat-Transfer and Momentum-Exchange Coefficients, Vol.III of W.R.Bohl compiler, An Advanced Fluid Dynamics Model, Los Alamos National Laboratory report LA-11692-MS, September 1990

nozzle diameter [cm]	initial pressure [bar abs]	inner vessel diameter [cm]		
		9	23	33
9	3	*37*	*95*	
	6		*93*	*32*
	11	*33*	*91*	*29*
6	11		*21*	*30*

Table A.1: Experimental parameters and denotation of 9 experiments

Test No.	$p_{initial}$ [bar abs]	p_{max} [bar abs]			t_{max} [ms]		
		corner	middle	center	corner	middle	center
95	0.3	0.47	0.48	0.48	17.7	17.7	17.7
93	0.6	1.44	2.86	4.80	11.36	10.68	10.18
91	1.1	3.40	8.00	11.8	8.52	7.50	7.37
21	1.1	2.10	7.50	11.4	8.10	7.04	6.80
32	0.6	1.96	1.97	1.93	10.0	10.1	9.96
29	1.1	6.00	6.43	7.24	7.22	7.12	7.00
30	1.1	3.43	5.70	7.50	7.67	7.28	7.02
33	0.3	-	1.70	2.60	-	14.2	13.8
37	1.1	-	5.48	10.3	-	7.80	7.42

Table A.2 : Maximum pressures at three positions at the vessel cover and their time of arrival

No.	t [ms]	a [m/s²]	q_e [m³/s]	λ_{cr} [mm]	D [cm]
33	1.5 - 4.75	7580	.009 - .017	0.62	3.4 - 4.6
37	2.75-8.61	2510	.010 - .013	1.07	4.0 - 4.6
91	2.49-5.38	7570	.082 - .180	0.62	10.2 - 15.1
93	3.20-6.94	4290	.069 - .111	0.82	10.0 - 12.7
95	5.15-11.7	1290	.045 - .074	1.50	9.4 - 12.1
21	1.20-3.86	6140	.083 - .133	0.69	10.5 - 13.3
29	1.25-6.94	2120	.057 - .332	1.17	10.0 - 24.0
30	1.54-7.50	2100	.091 - .346	1.17	12.6 - 24.5
32	1.40-8.98	1210	.070 - .094	1.55	11.8 - 13.7

Table A.3. Comparison of experimental results with Eq.(4)

initial pressure	bar	5	11	22	44	11
cell length		single				double
acceleration	m/s²	3500	4300	13000	30600	6429
void gradient	1/m	29.4	29.4	27.8	26.3	16.1
time the void front is at 0.4 m	ms	9.9	6.2	4.3	3.1	5.8
velocity of front	m/s	28	42	55	85	40
void gradient times cell length		0.32	0.32	0.31	0.29	0.35

Table B.1. AFDM data of numerical diffusion for SGI-33

P1 pressure vessel
P2 nozzle
P3 top center
P4 top middle
P5 top corner
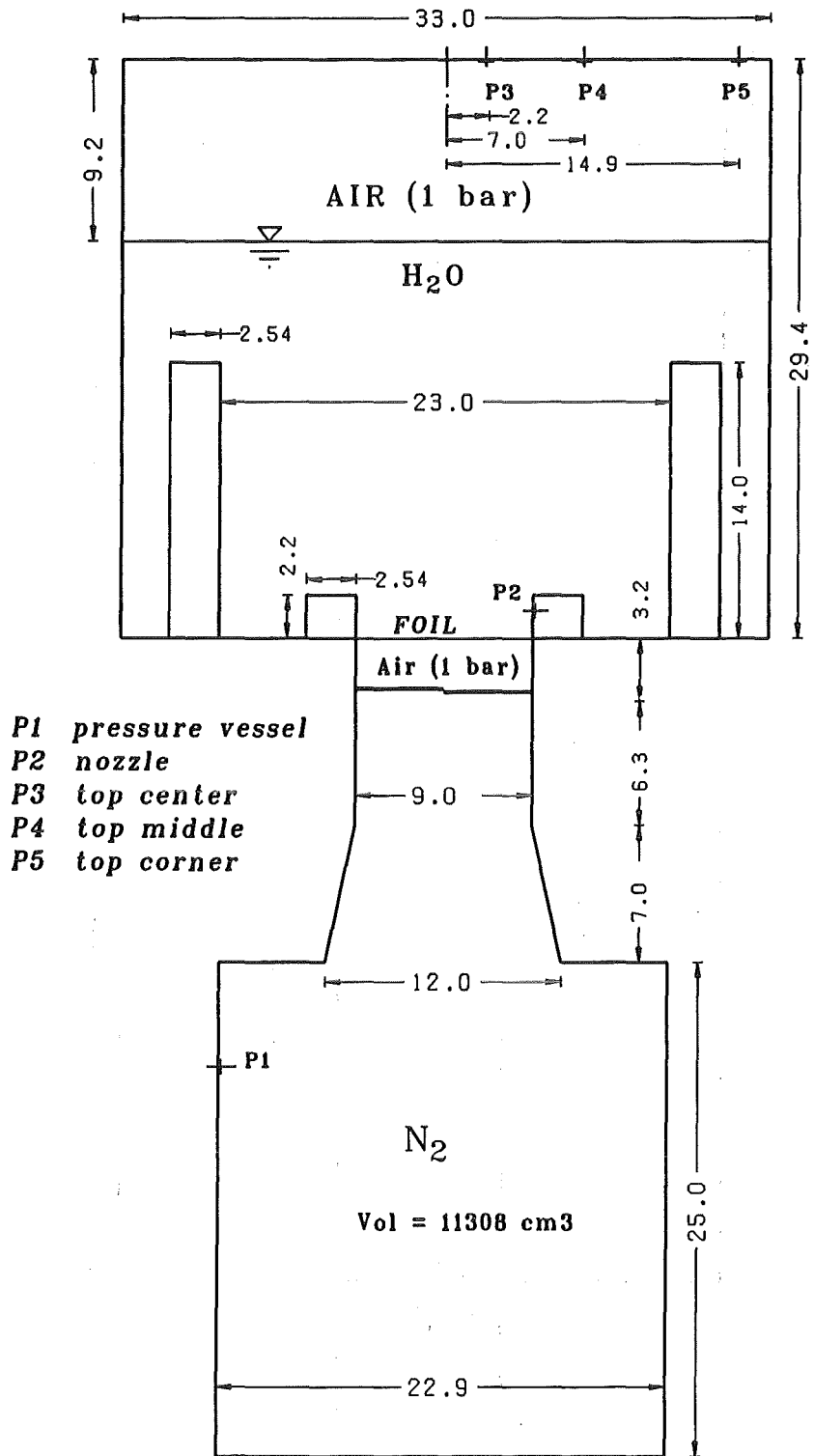
Fig. A.1 Scheme of experimental apparatus
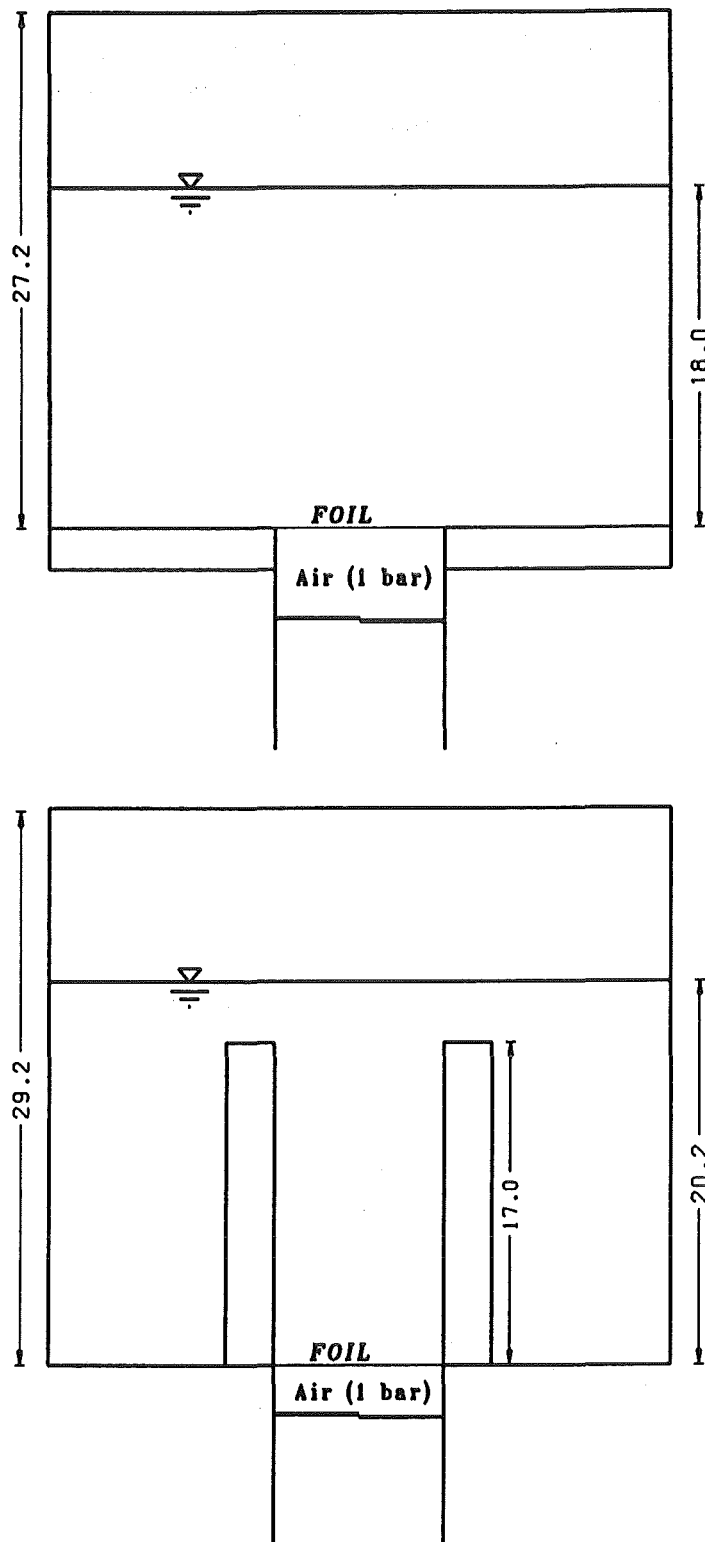
Fig. A.2 (a) top: vessel geometry in tests No. 29, 30 and 32, (b) bottom: vessel geometry in tests No. 33 and 37
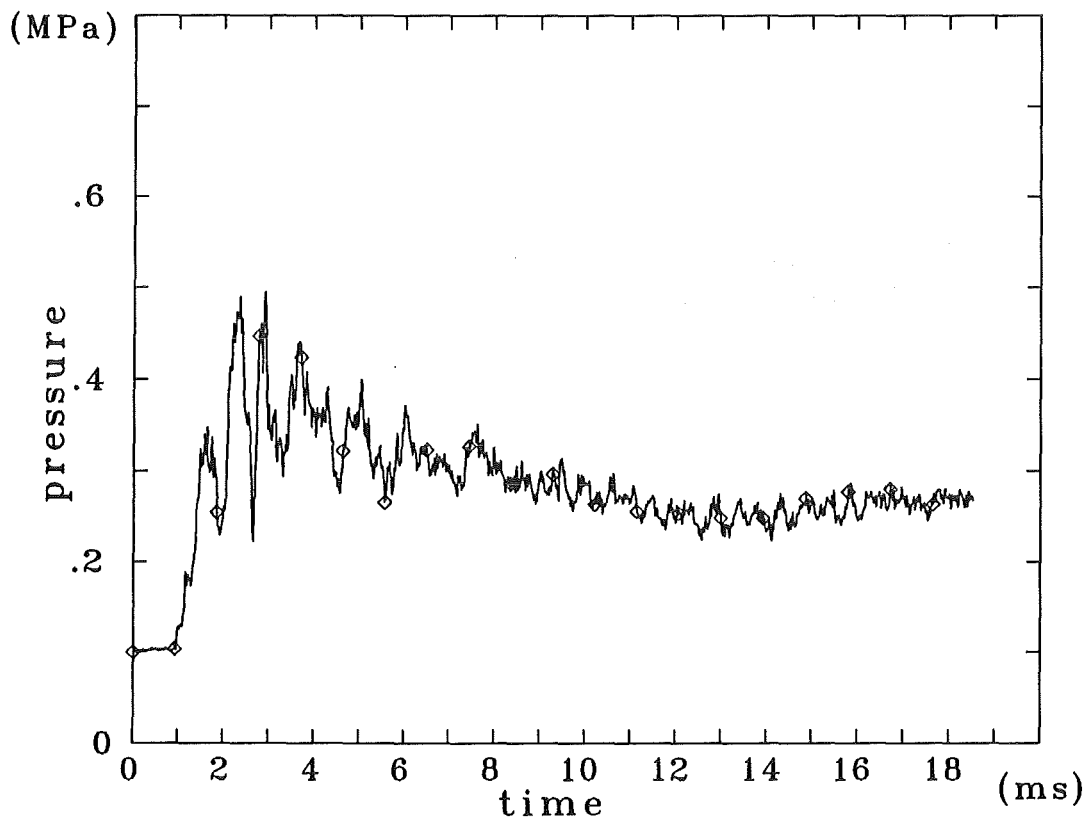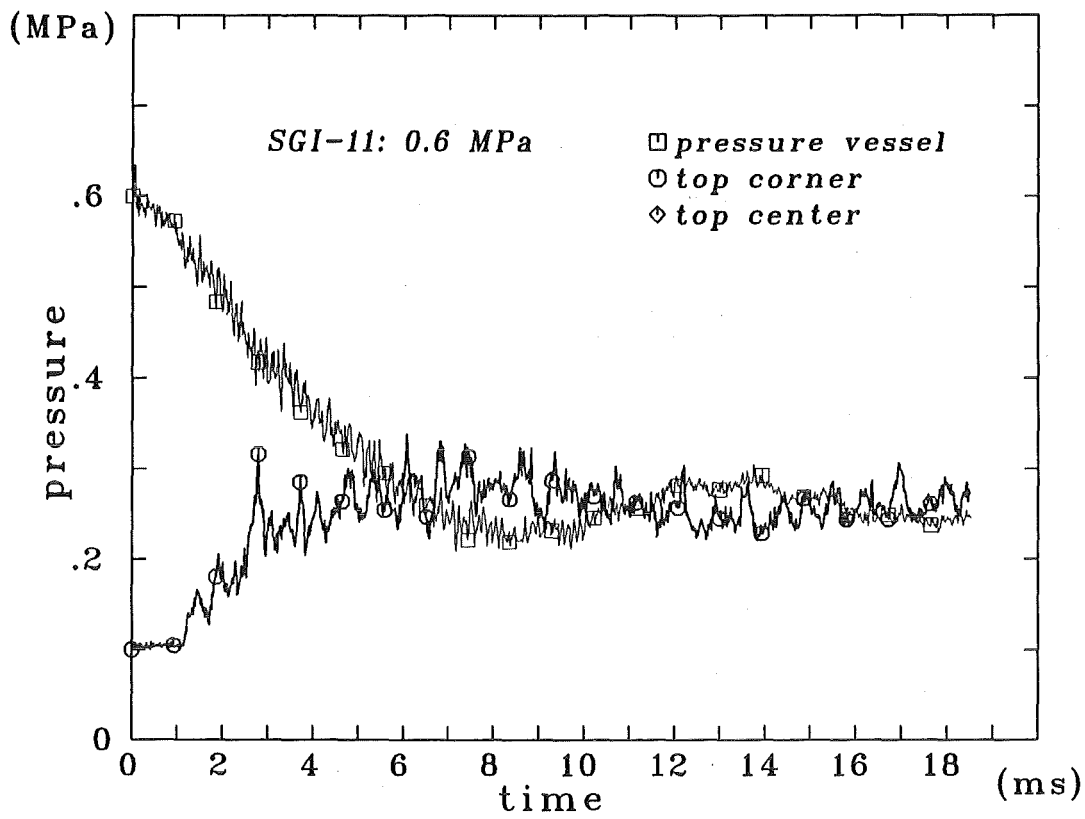
Fig. A.3 Pressures in a test without water in the upper vessel
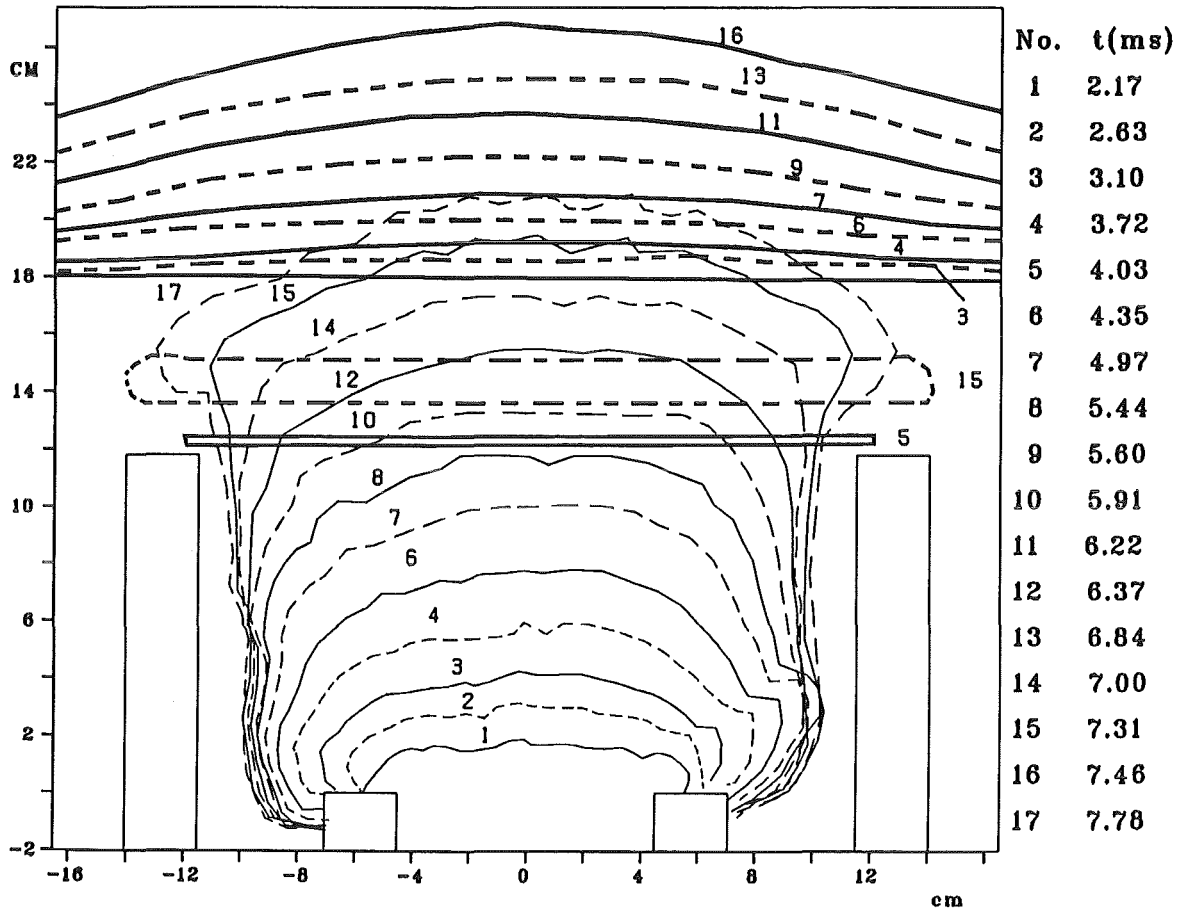
Fig. A.4 Contour plot of expanding bubble surface, vortex ring and water surface in a 1.1 MPa experiment
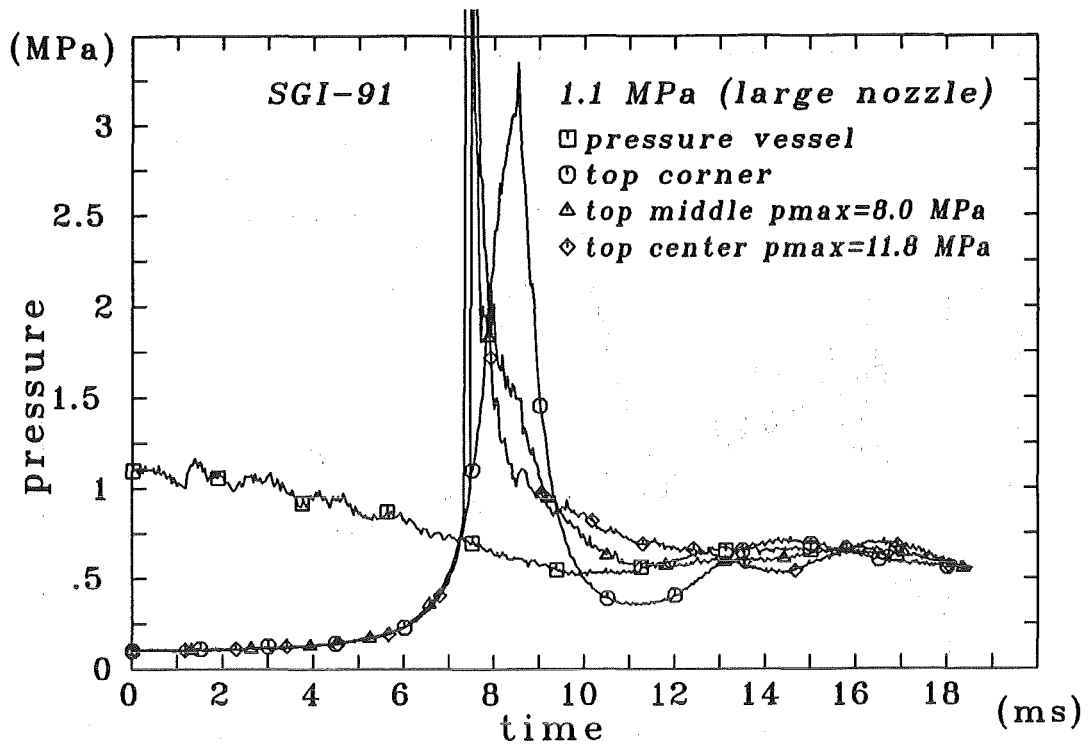
Fig. A.5 Pressures in test No. 91
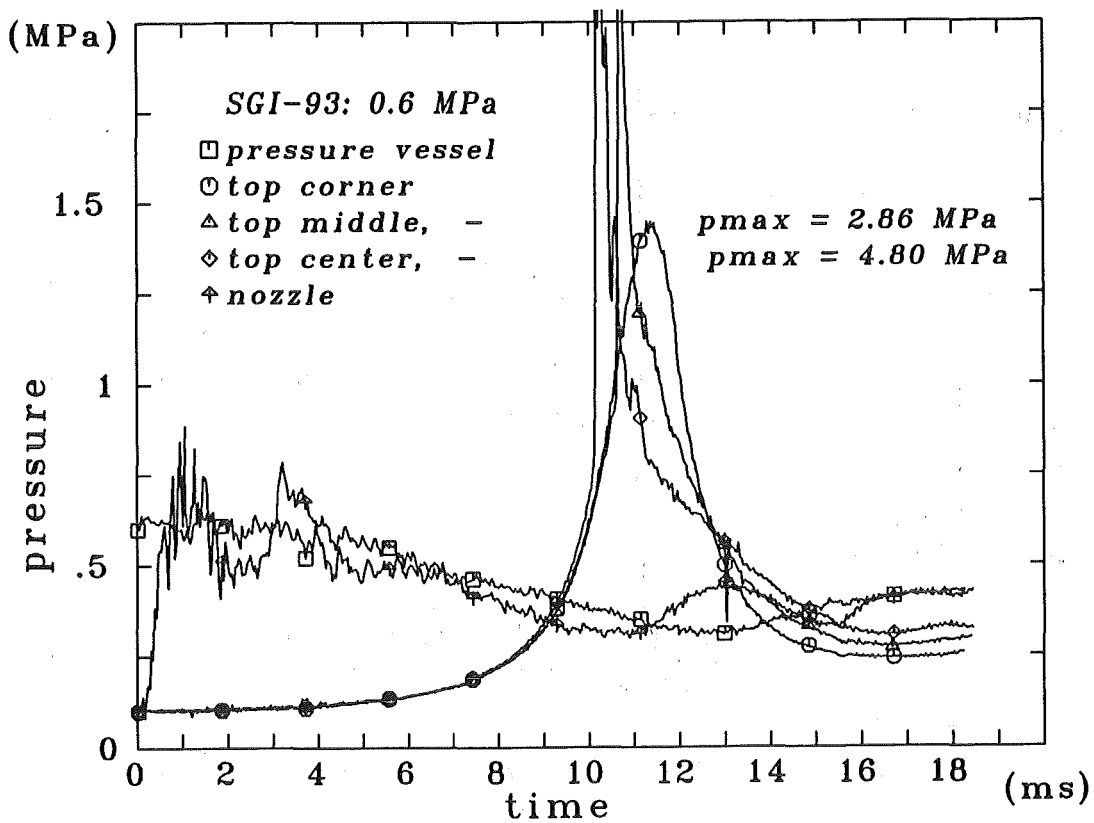
Fig. A.6 Pressures in test No. 93
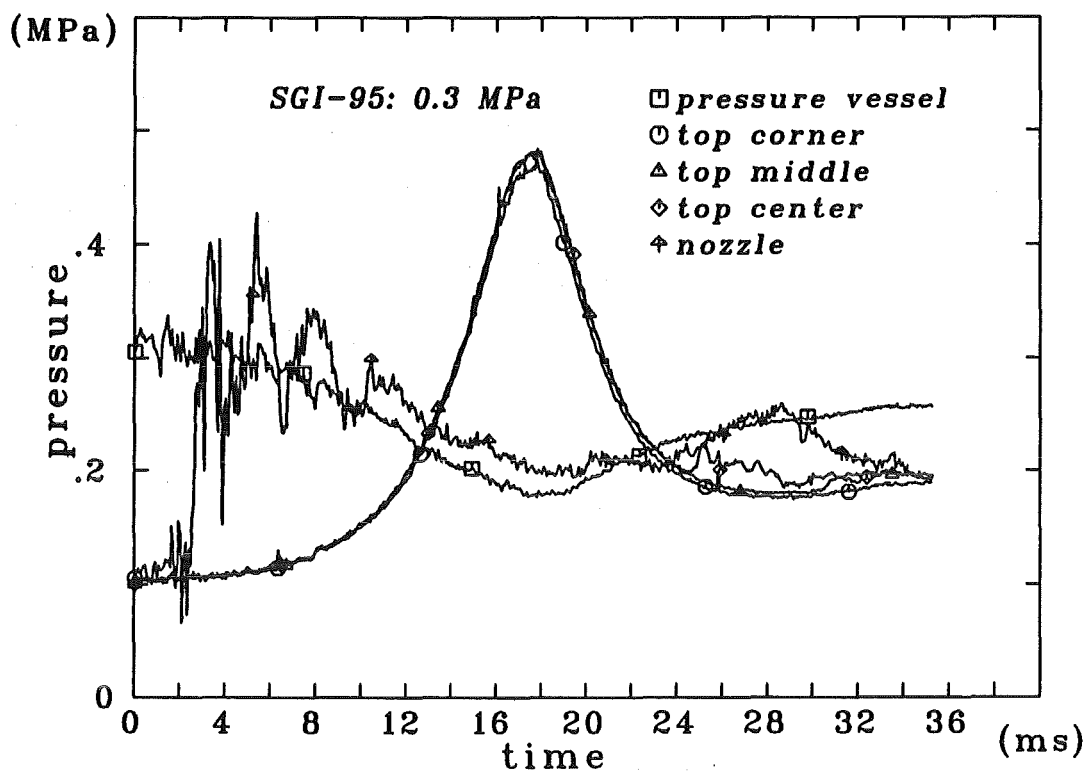
Fig. A.7 Pressures in test No. 95
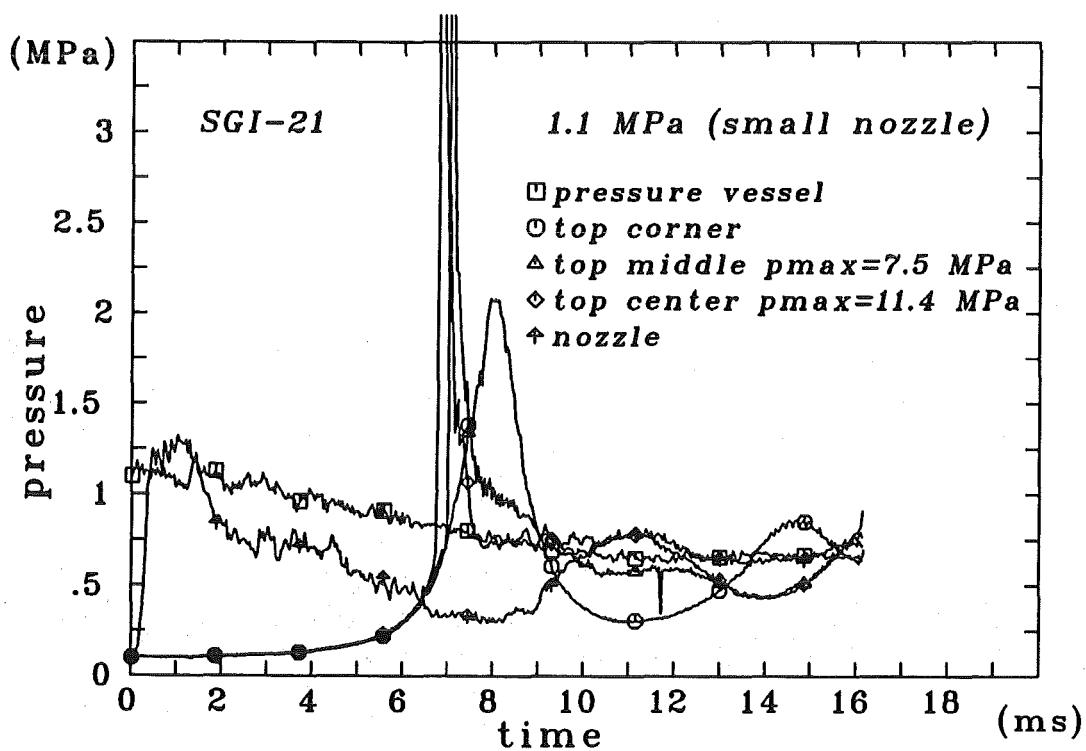
Fig. A.8 Pressures in test No. 21
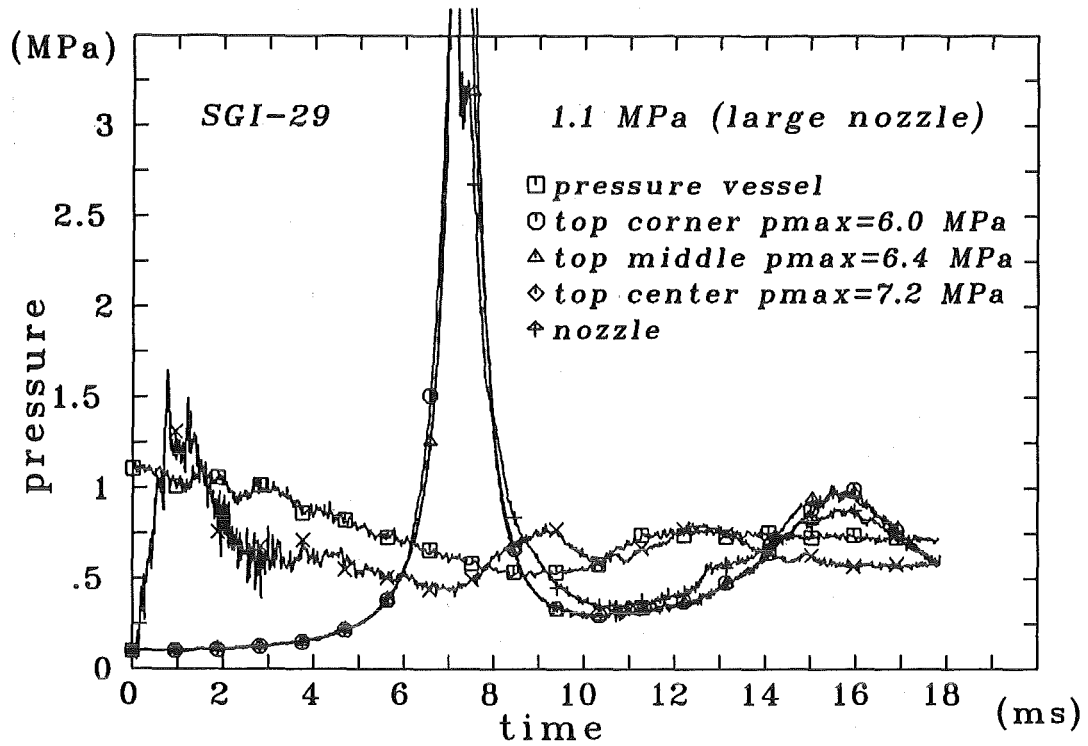
Fig. A.9 Pressures in test No. 29
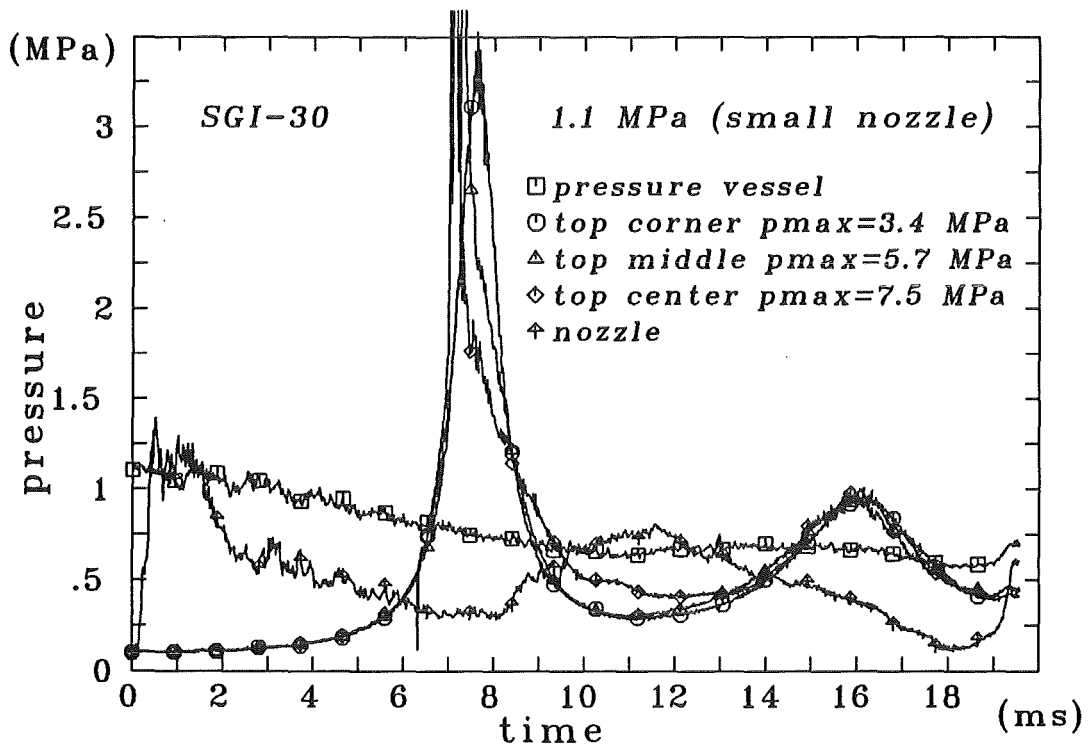
Fig. A.10 Pressures in test No. 30
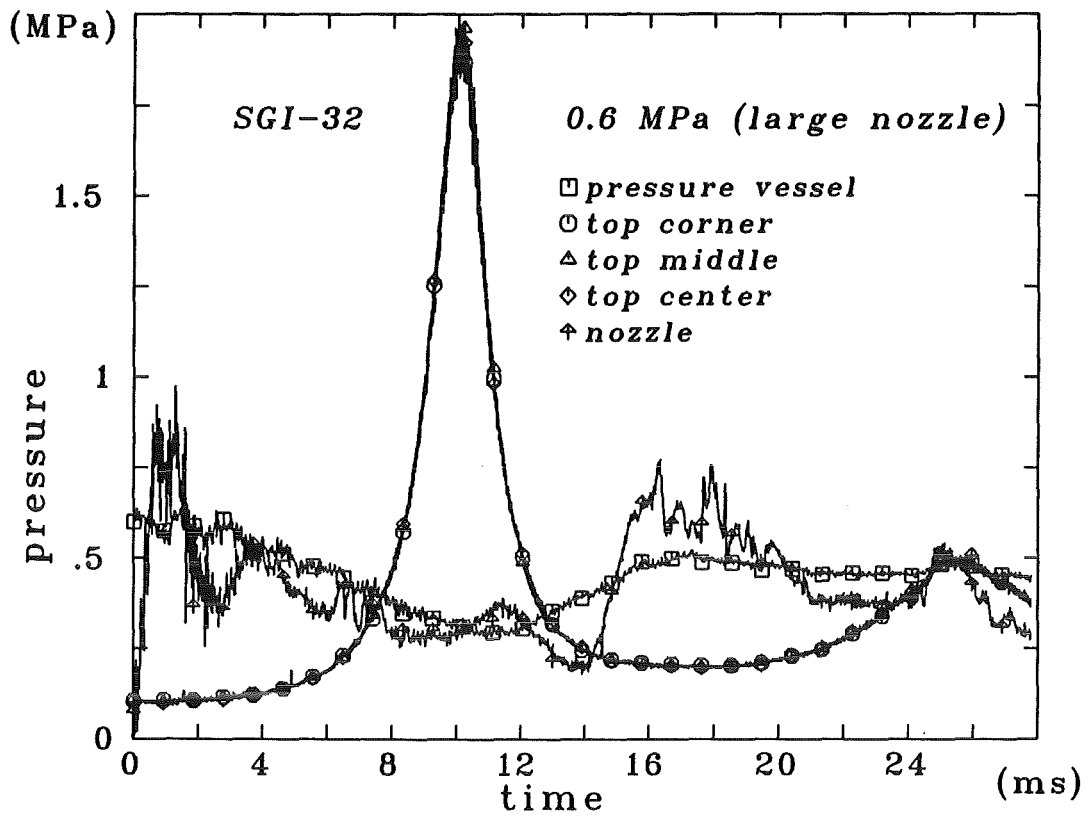
Fig. A.11 Pressures in test No. 32
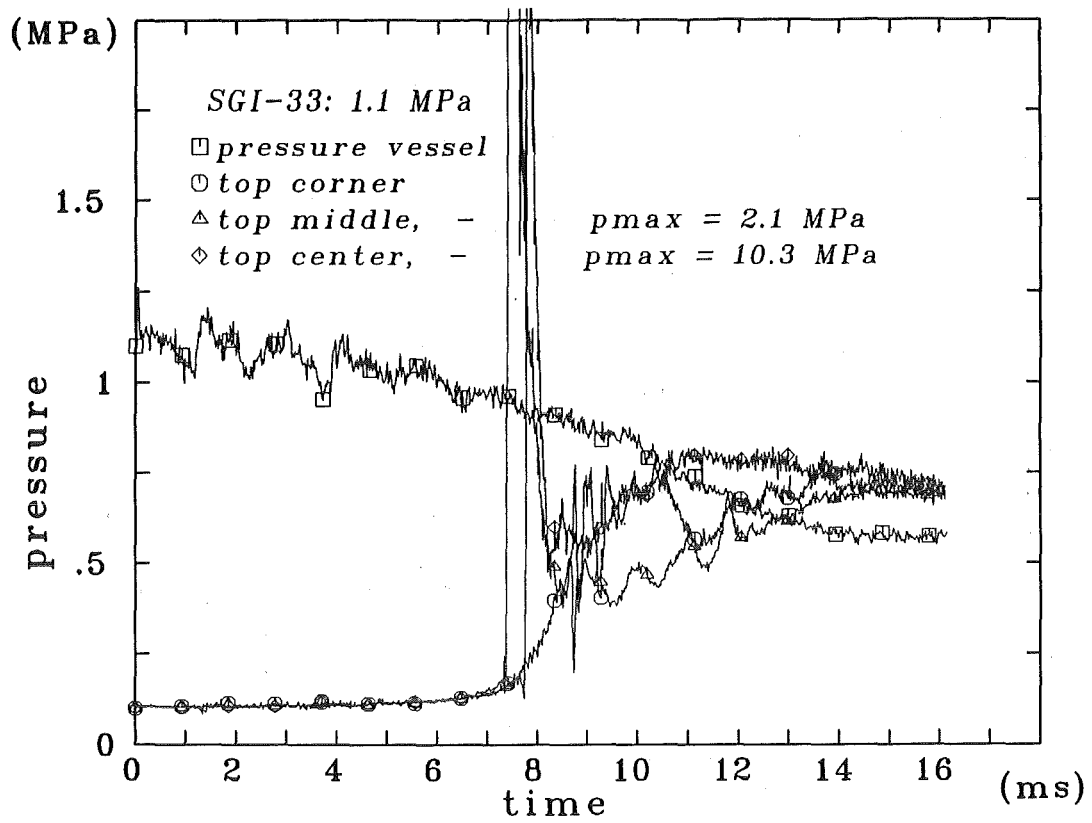
Fig. A.12 Pressures in test No. 33
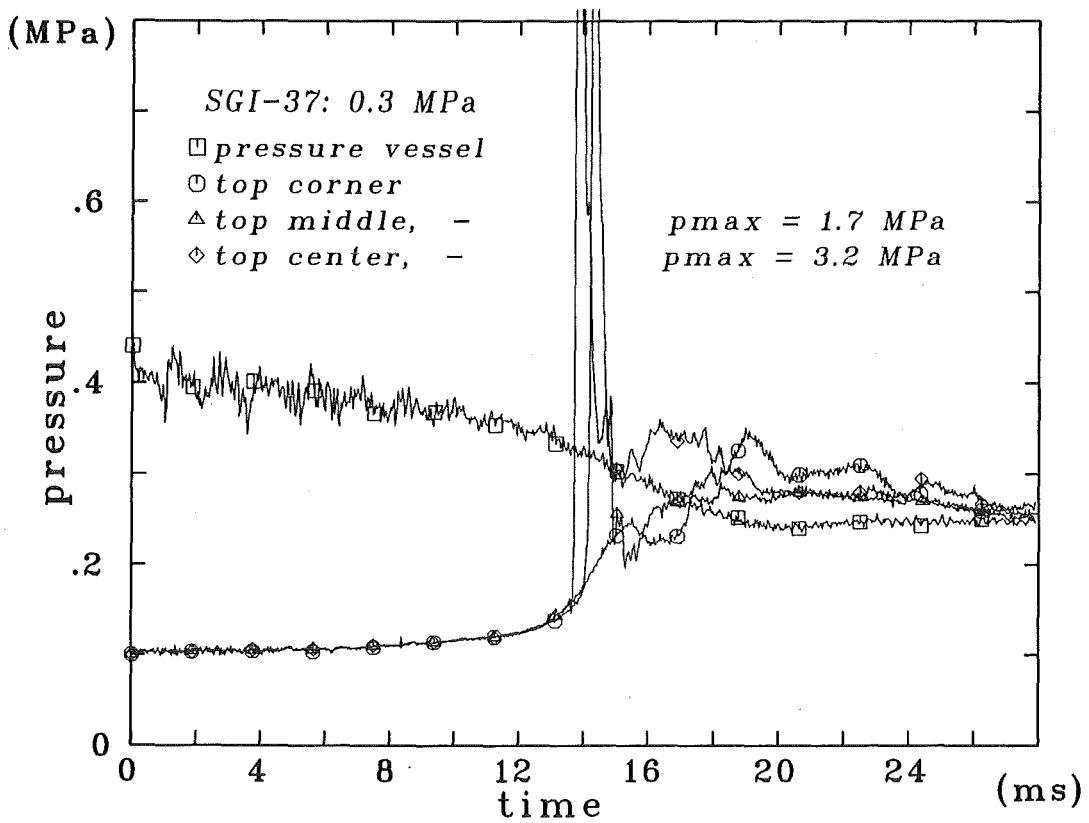
Fig. A.13 Pressures in test No. 37
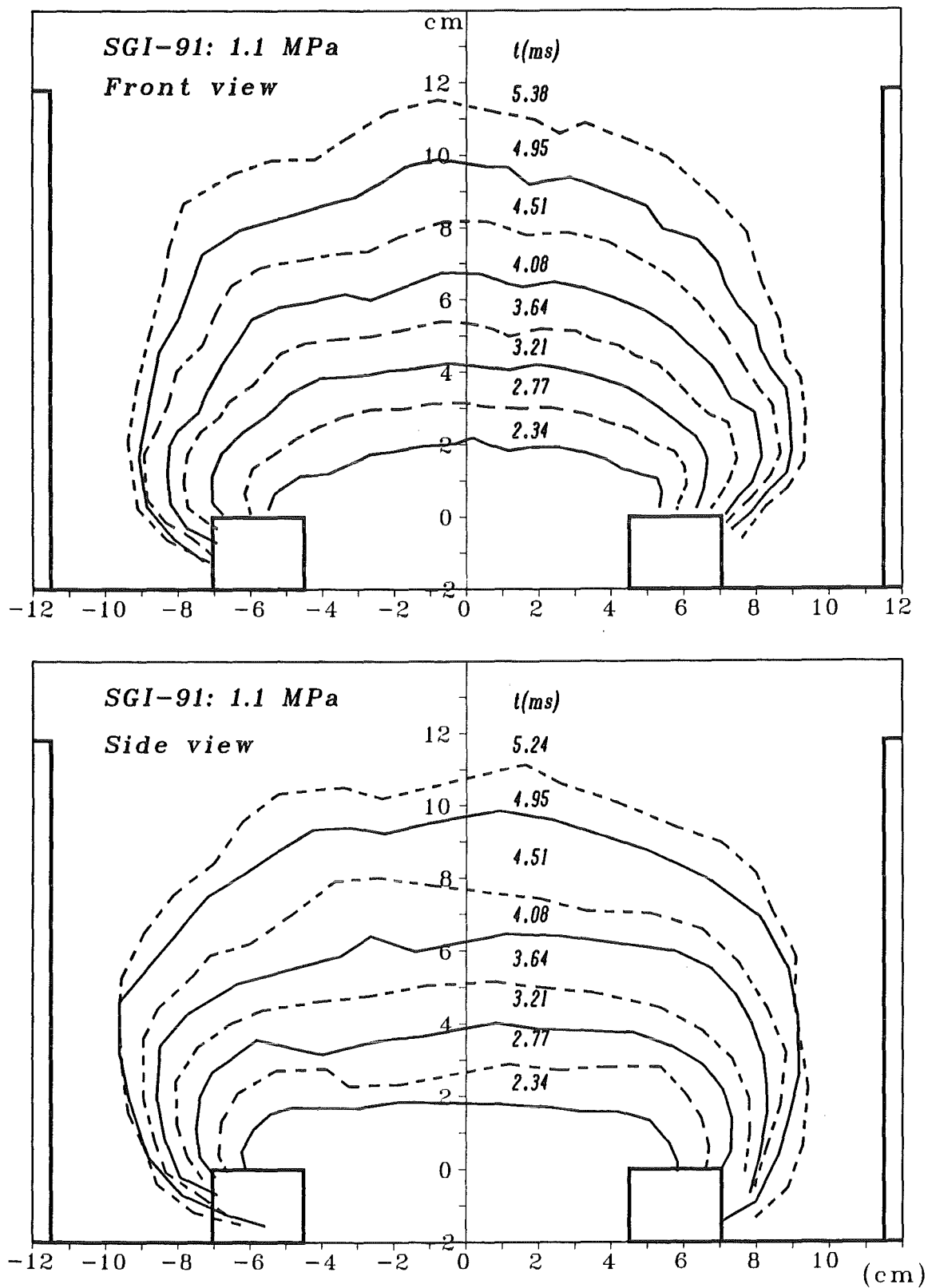
Fig. A.14 Contour plot of bubble surface at different times in test No. 91
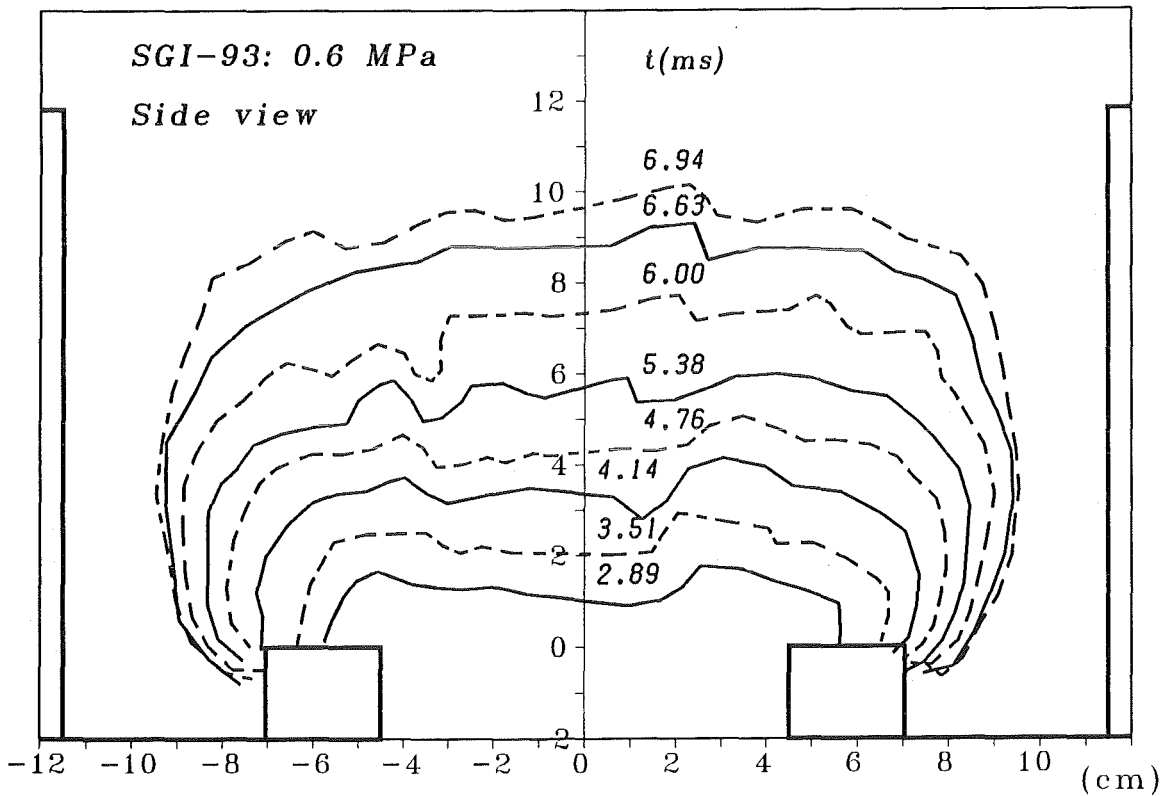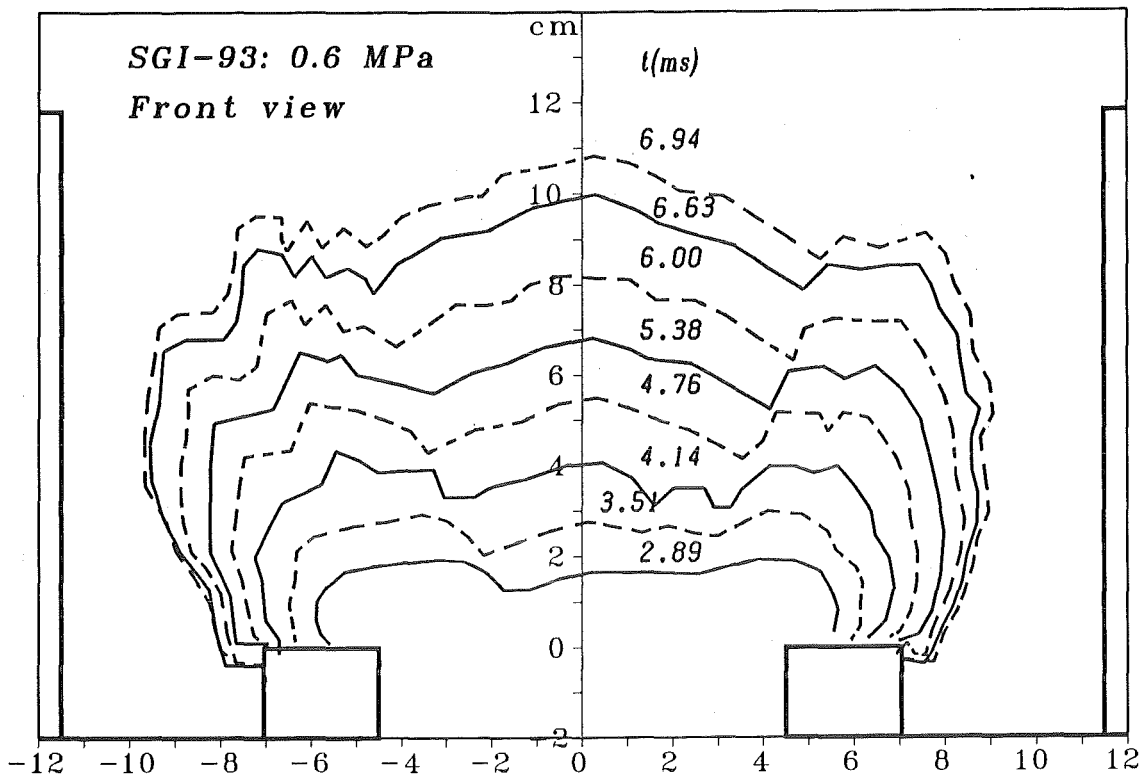
Fig. A.15 Contour plot of bubble surface at different times in test No. 93
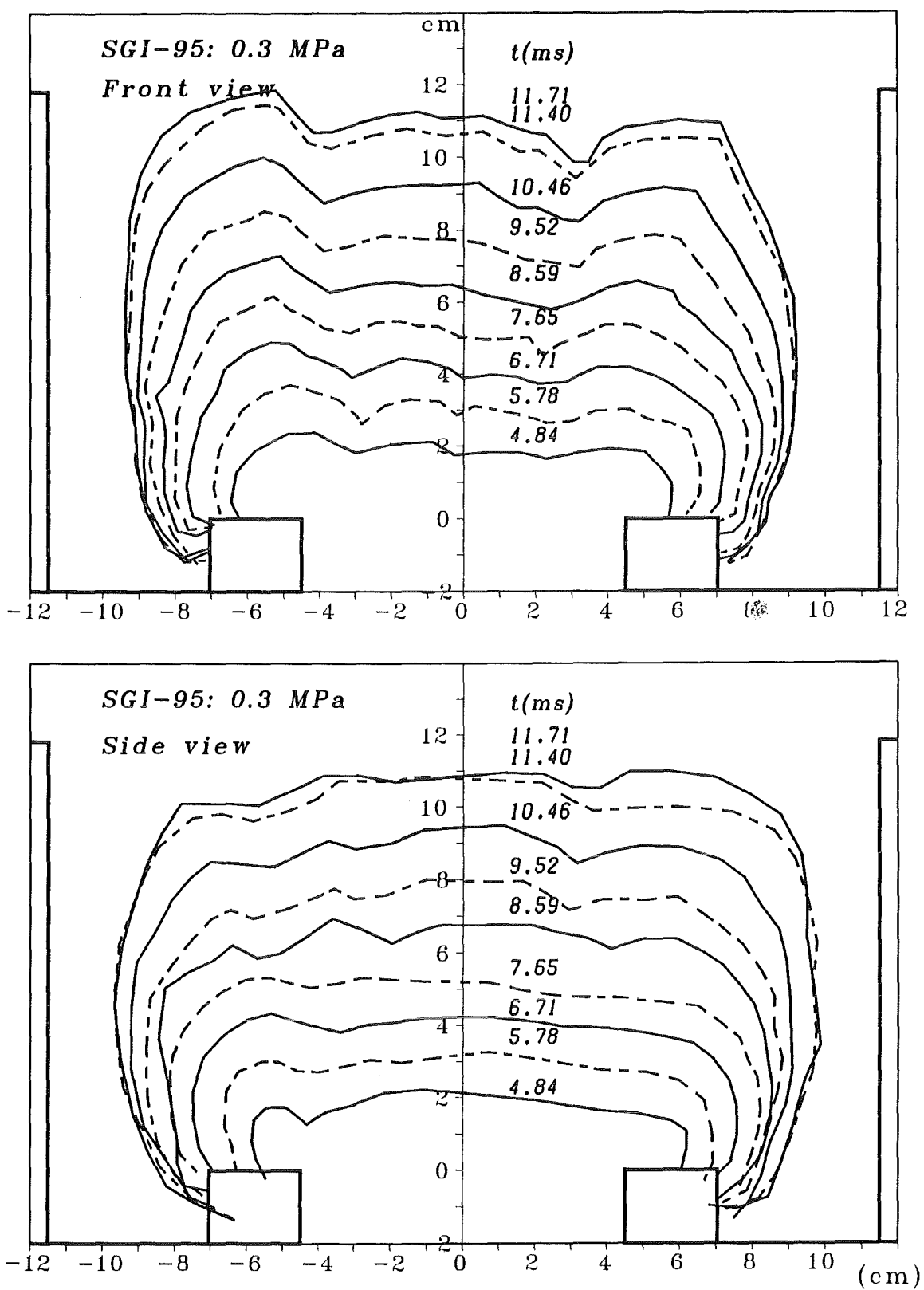
Fig. A.16 Contour plot of bubble surface at different times in test No. 95
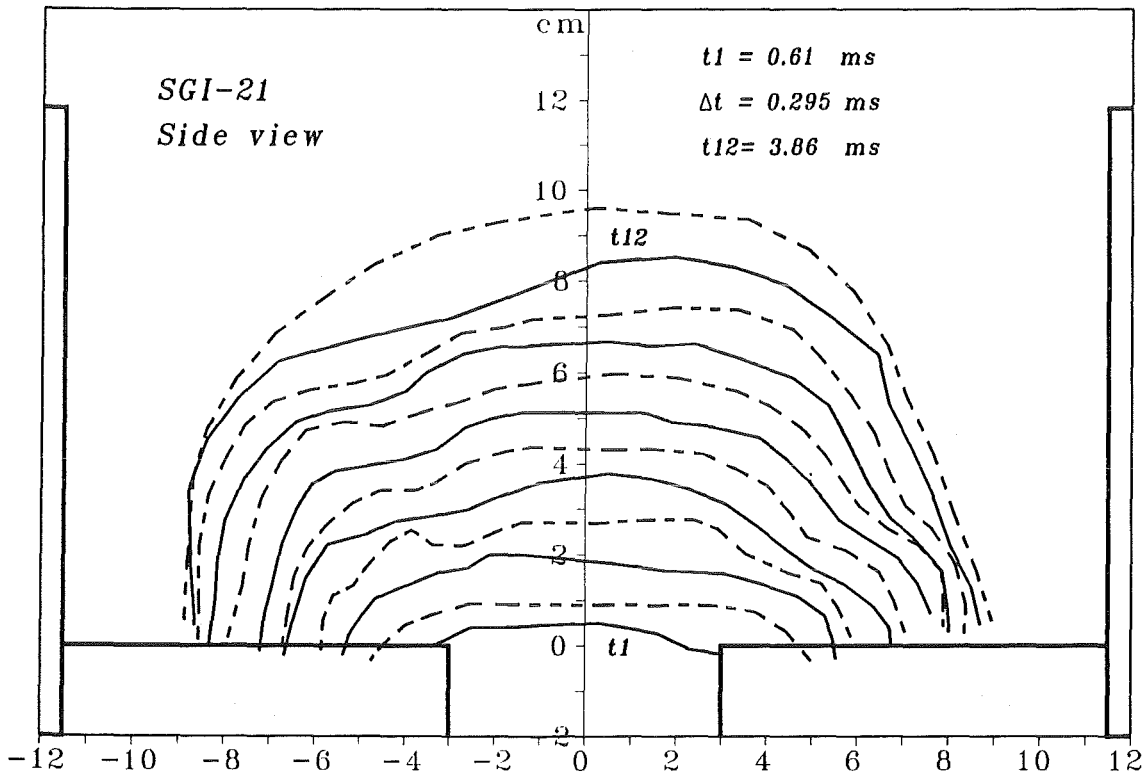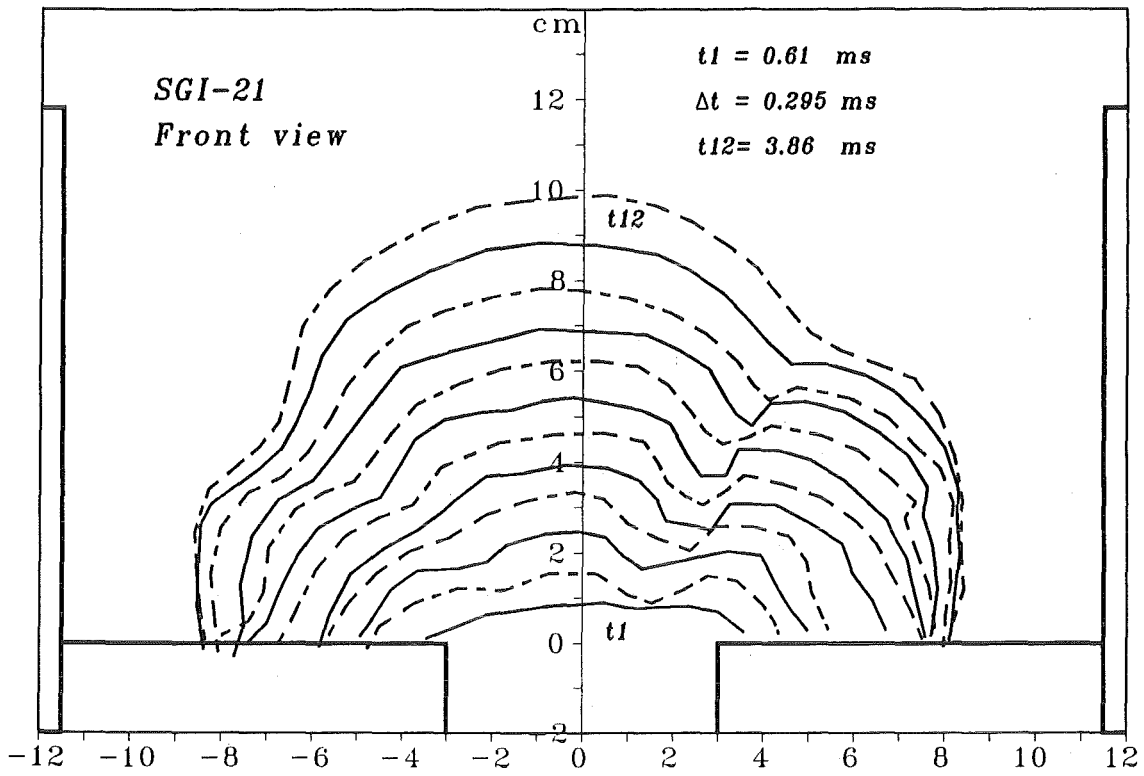
Fig. A.17 Contour plot of bubble surface at different times in test No. 21
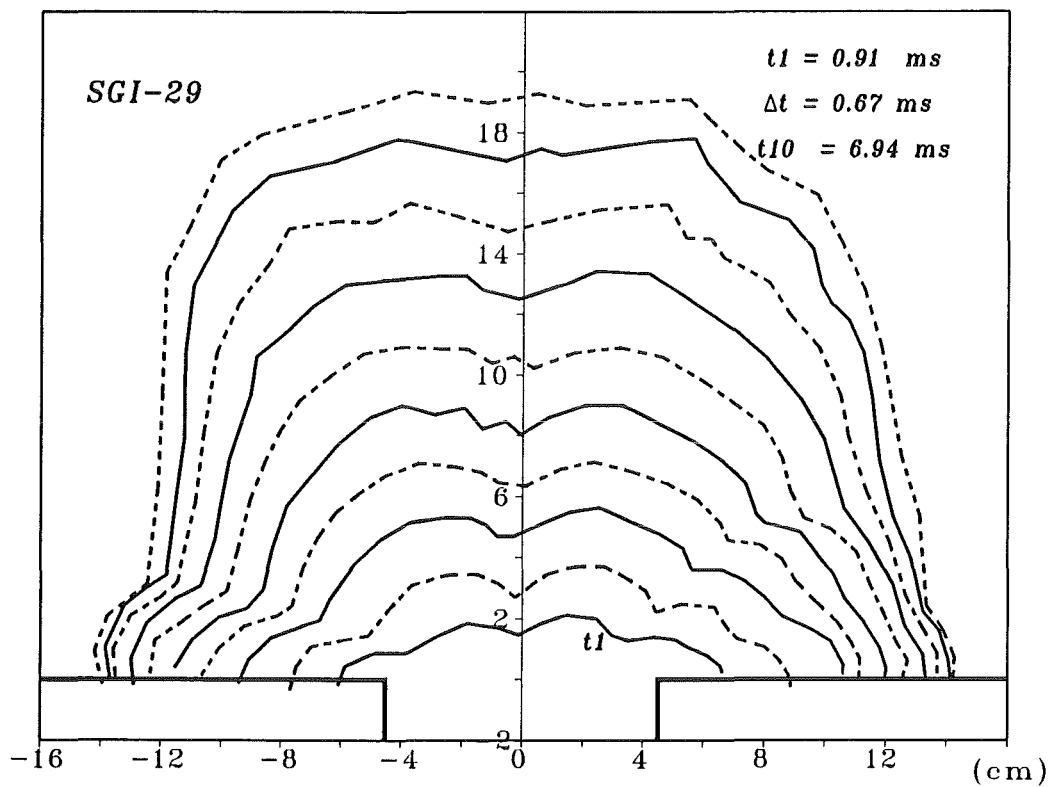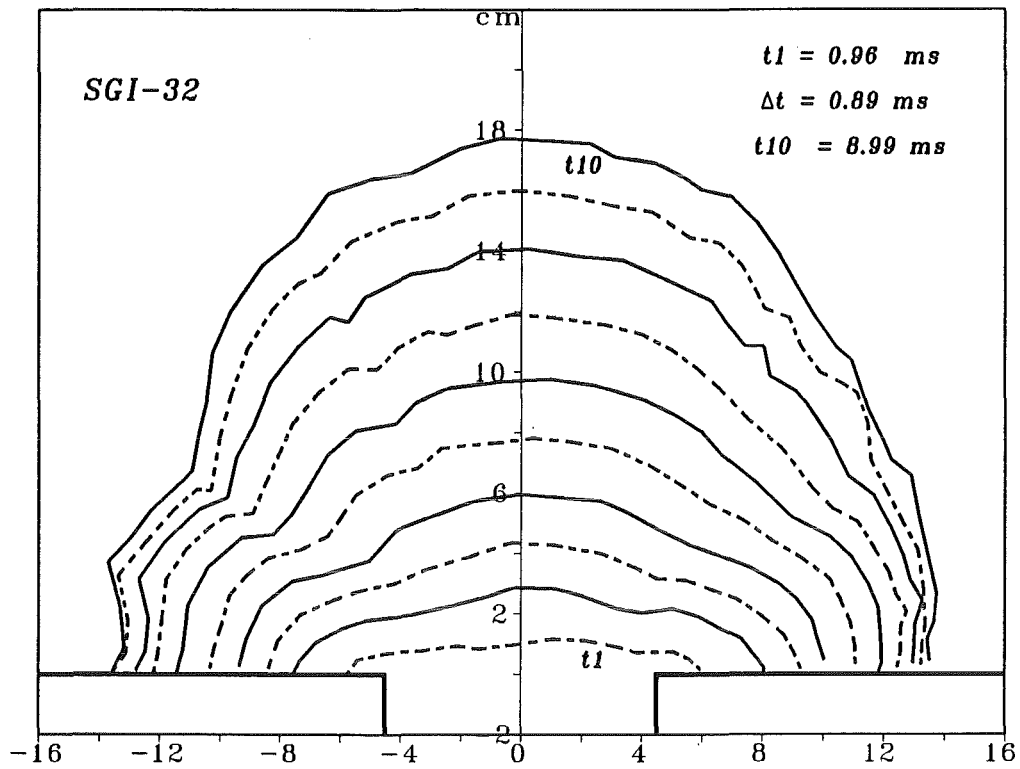
Top: **Fig. A.18** Contour plot of bubble surface at different times in test No. 32

Bottom: **Fig. A.19** Contour plot of bubble surface at different times in test No. 29
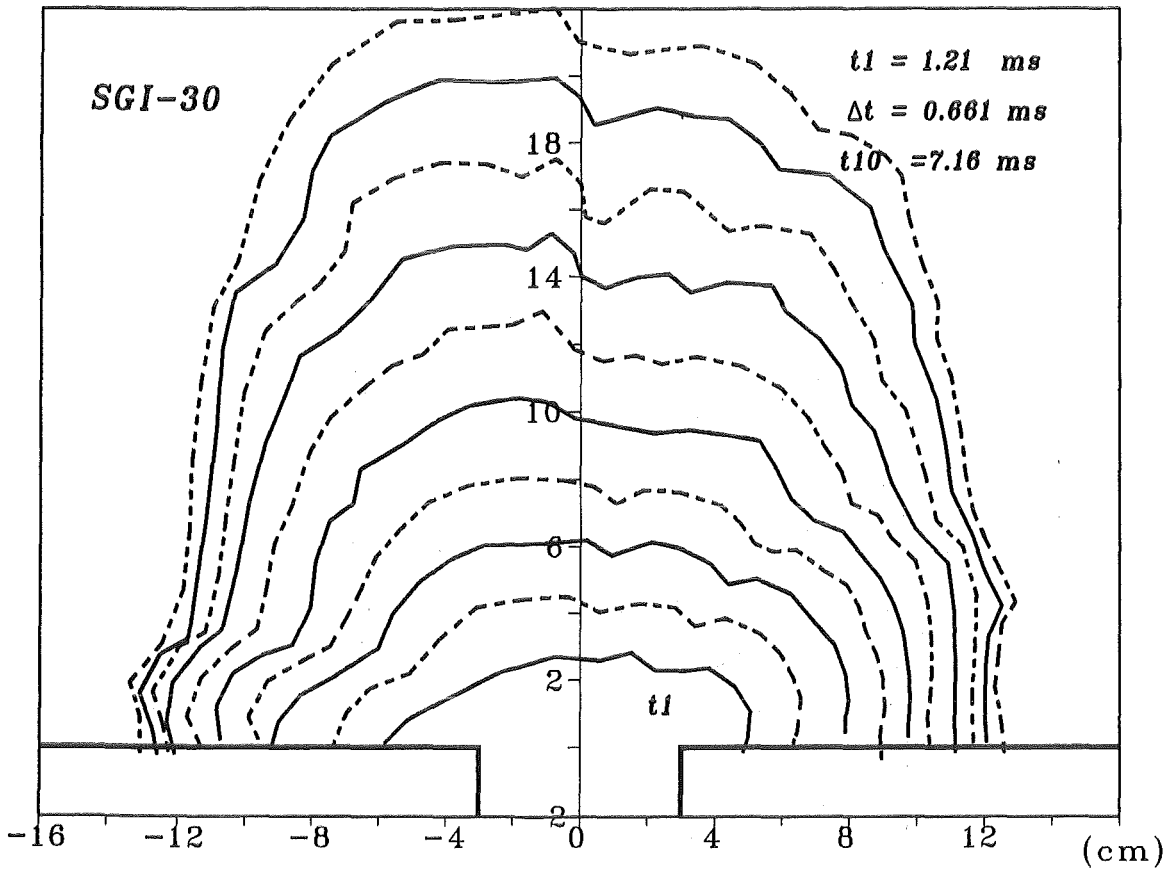
Fig. A.20 Contour plot of bubble surface at different times in test No. 30
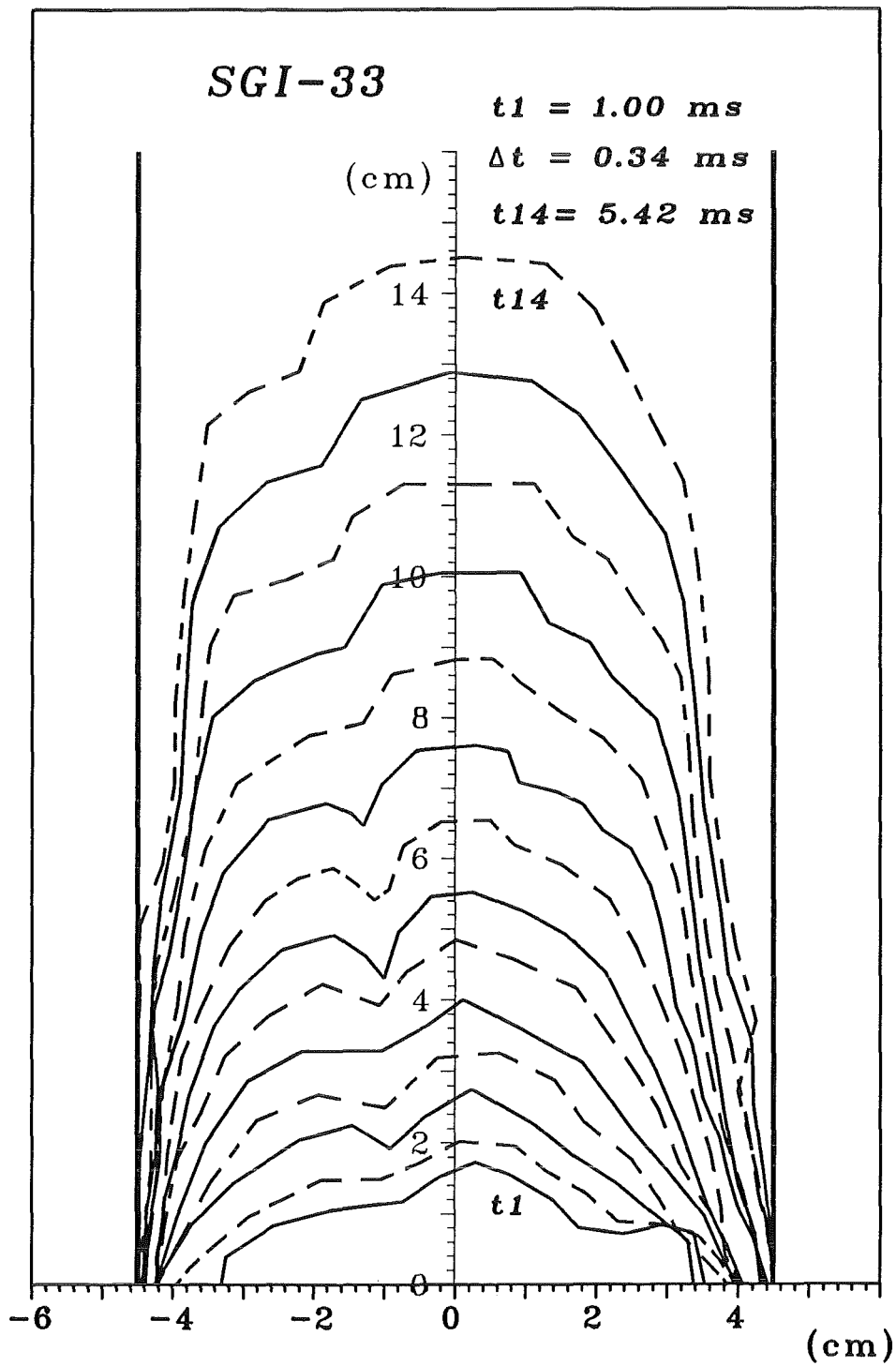
Fig. A.21 Contour plot of bubble surface at different times in test No. 33
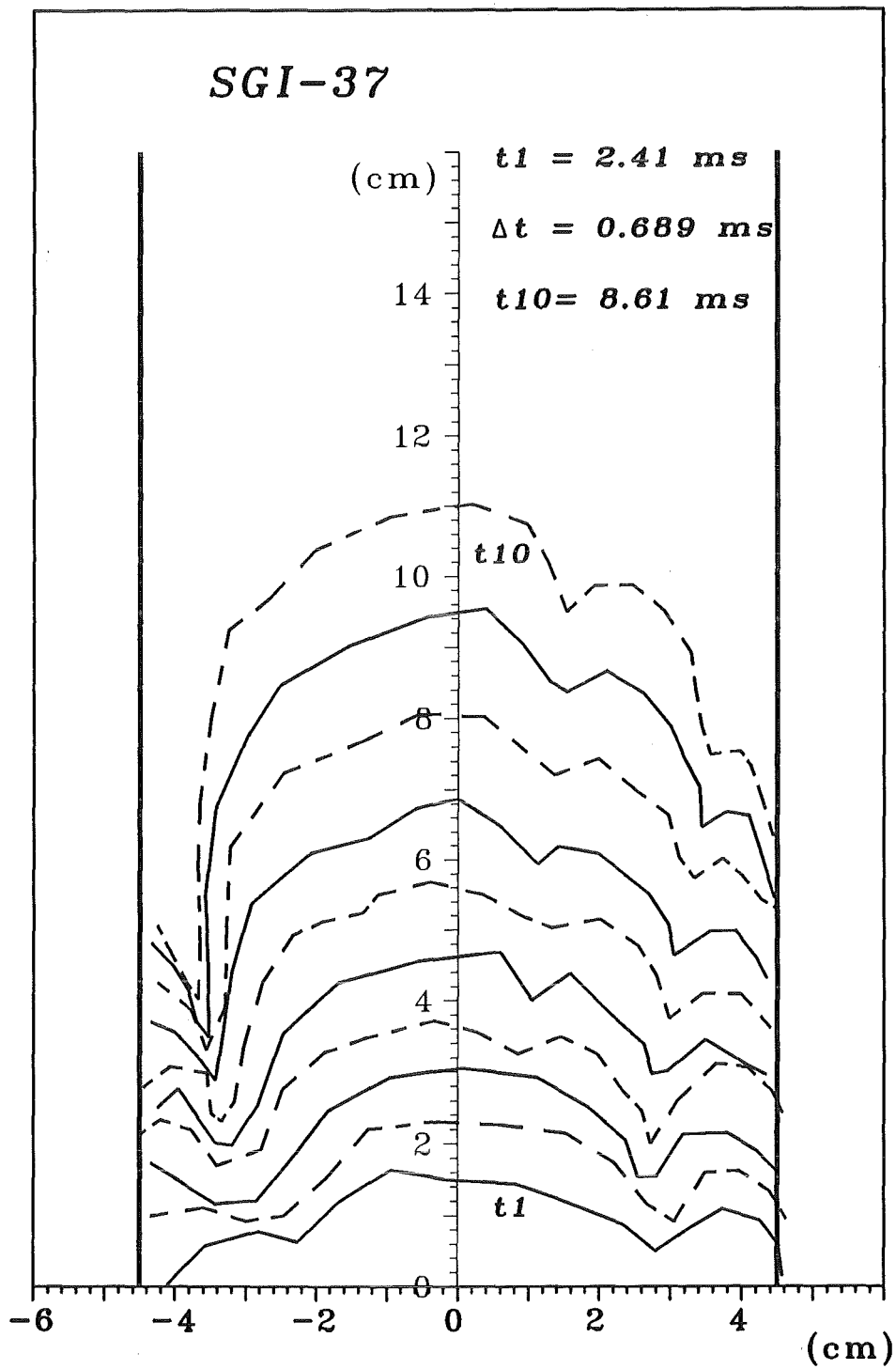
Fig. A.22 Contour plot of bubble surface at different times in test No. 37
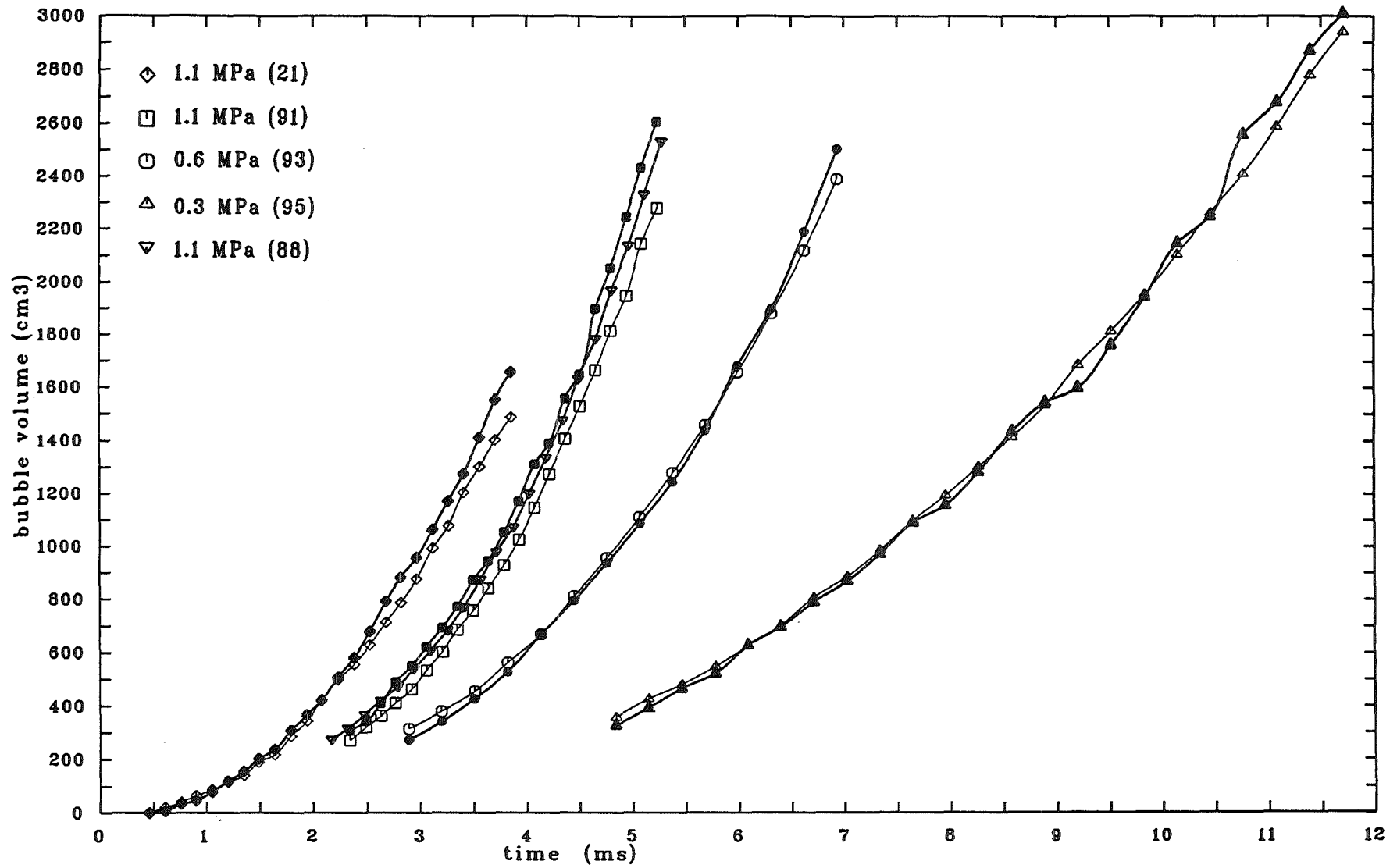
Fig. A.23 Bubble volumes versus time, derived from front view and side view
(open symbols: front view, full symbols: side view)
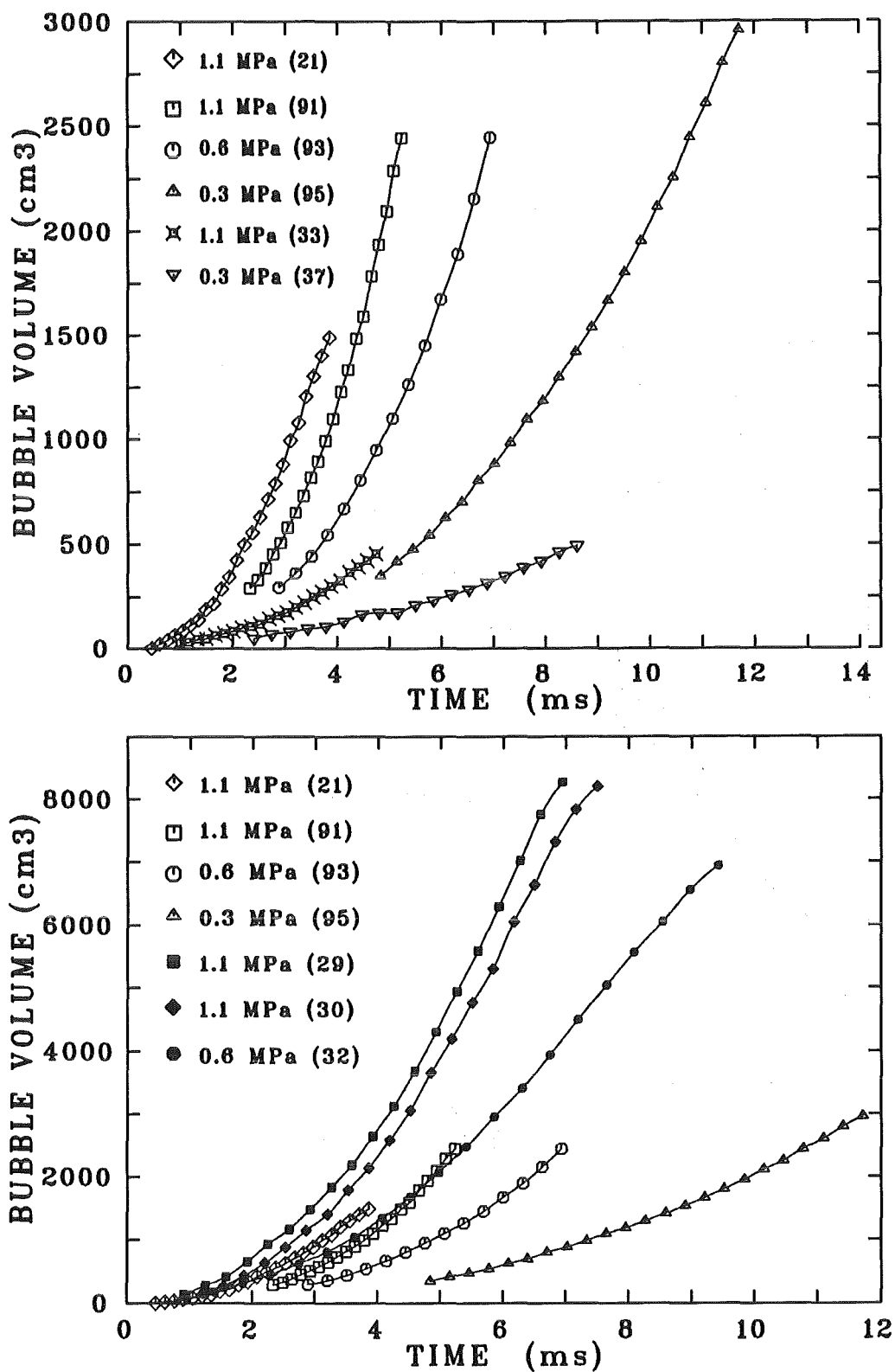
Fig. A.24 Bubble volumes versus time
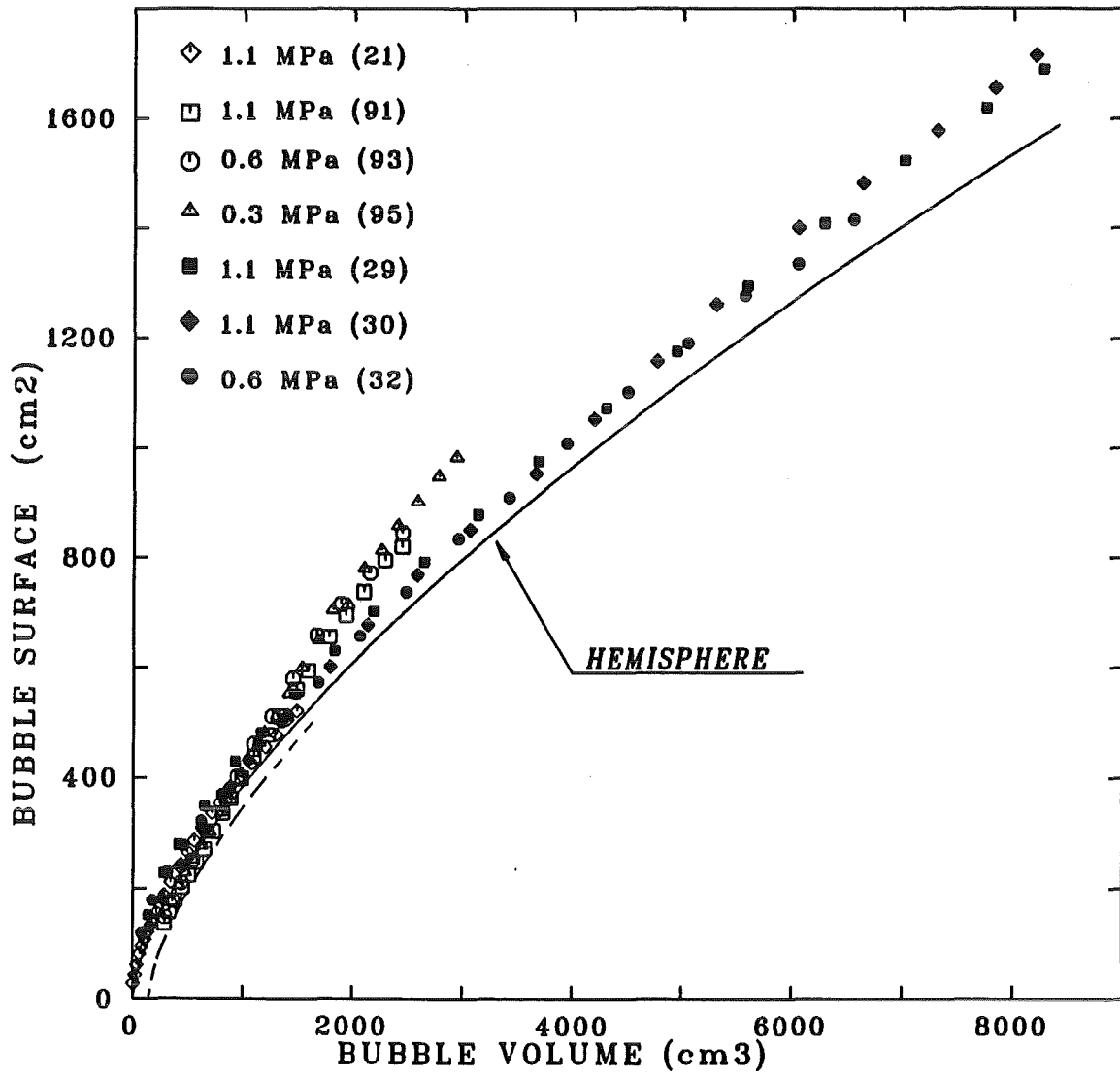
Fig. A.25 Bubble surface versus bubble volume

SGI-91: 1.1 MPa
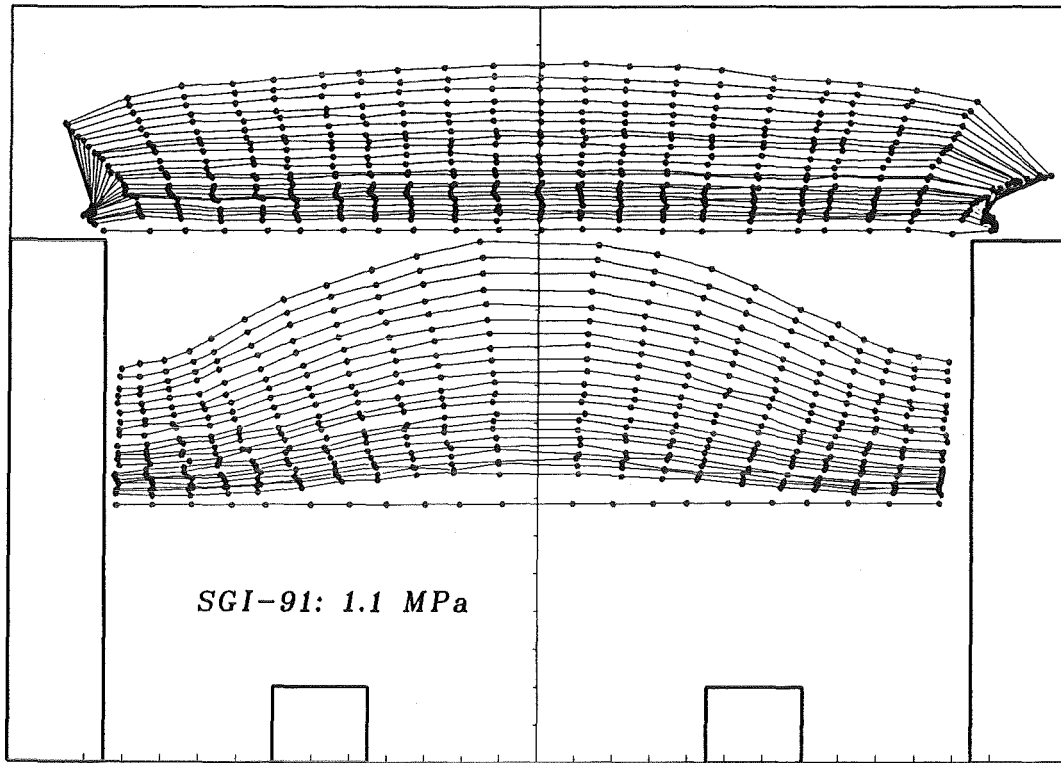
Fig. A.26 Bead positions in the water at different times in test No.91
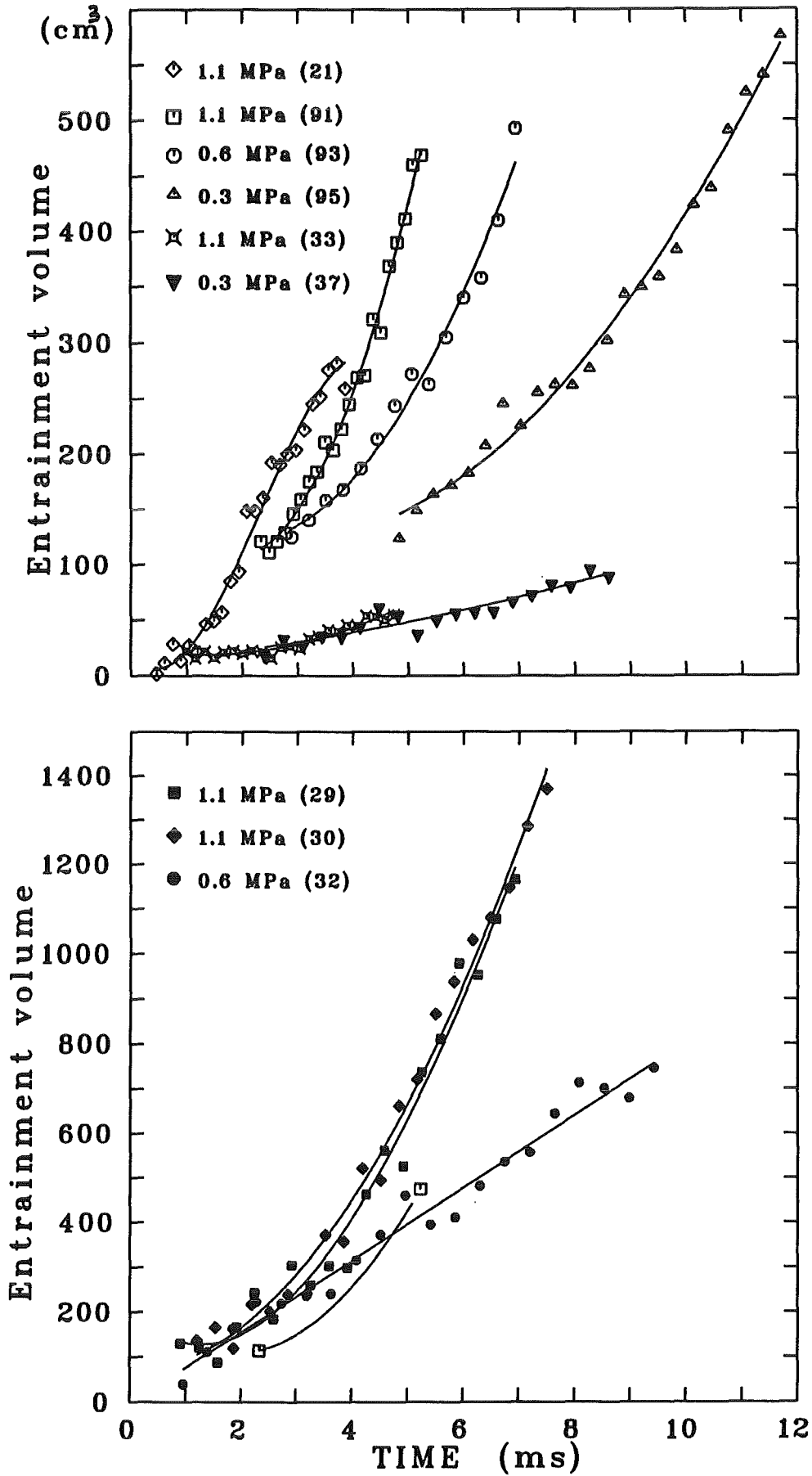
Fig. A.27 Entrainment volume versus time
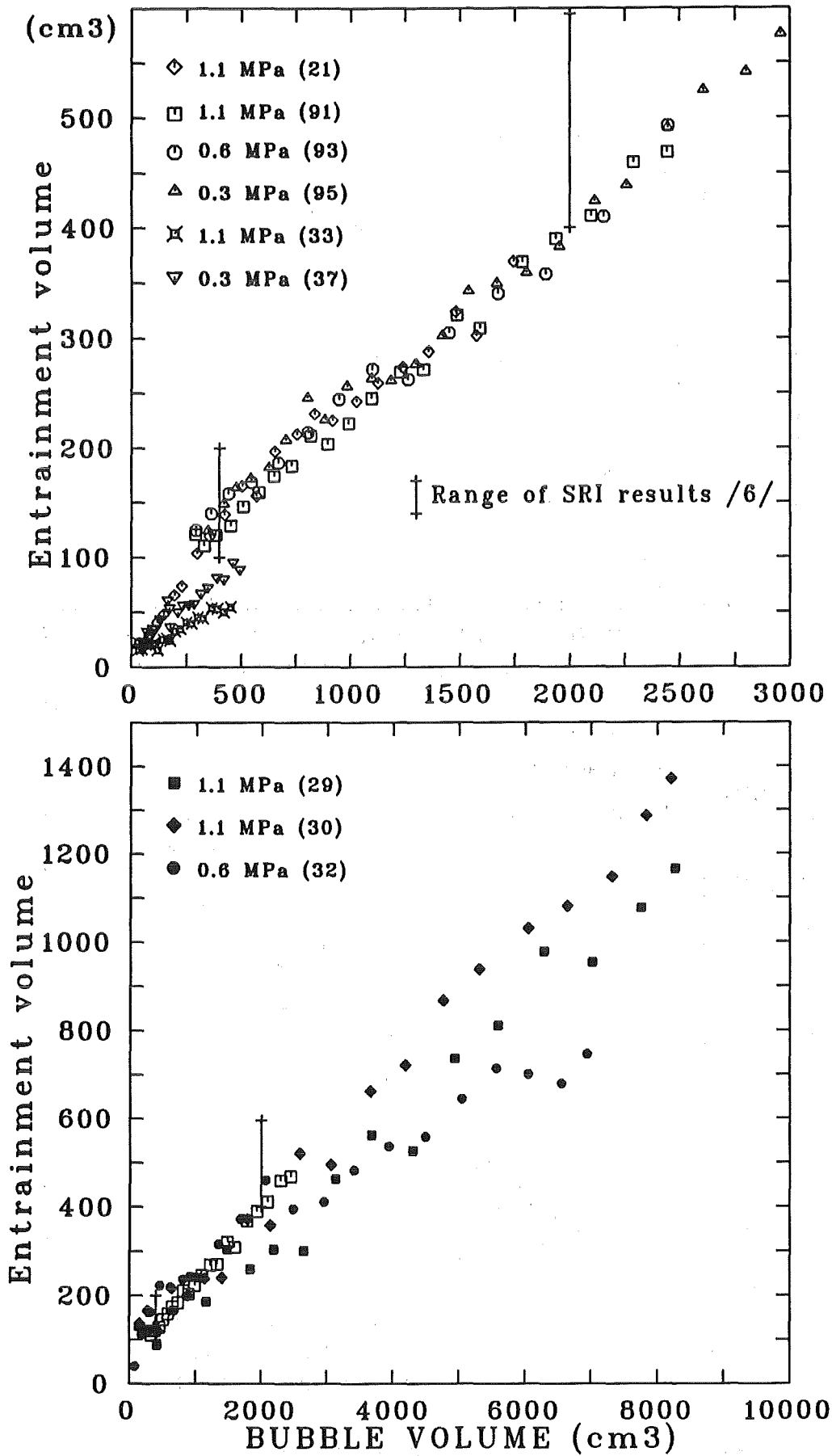
Fig. A.28 Entrainment volume versus bubble volume
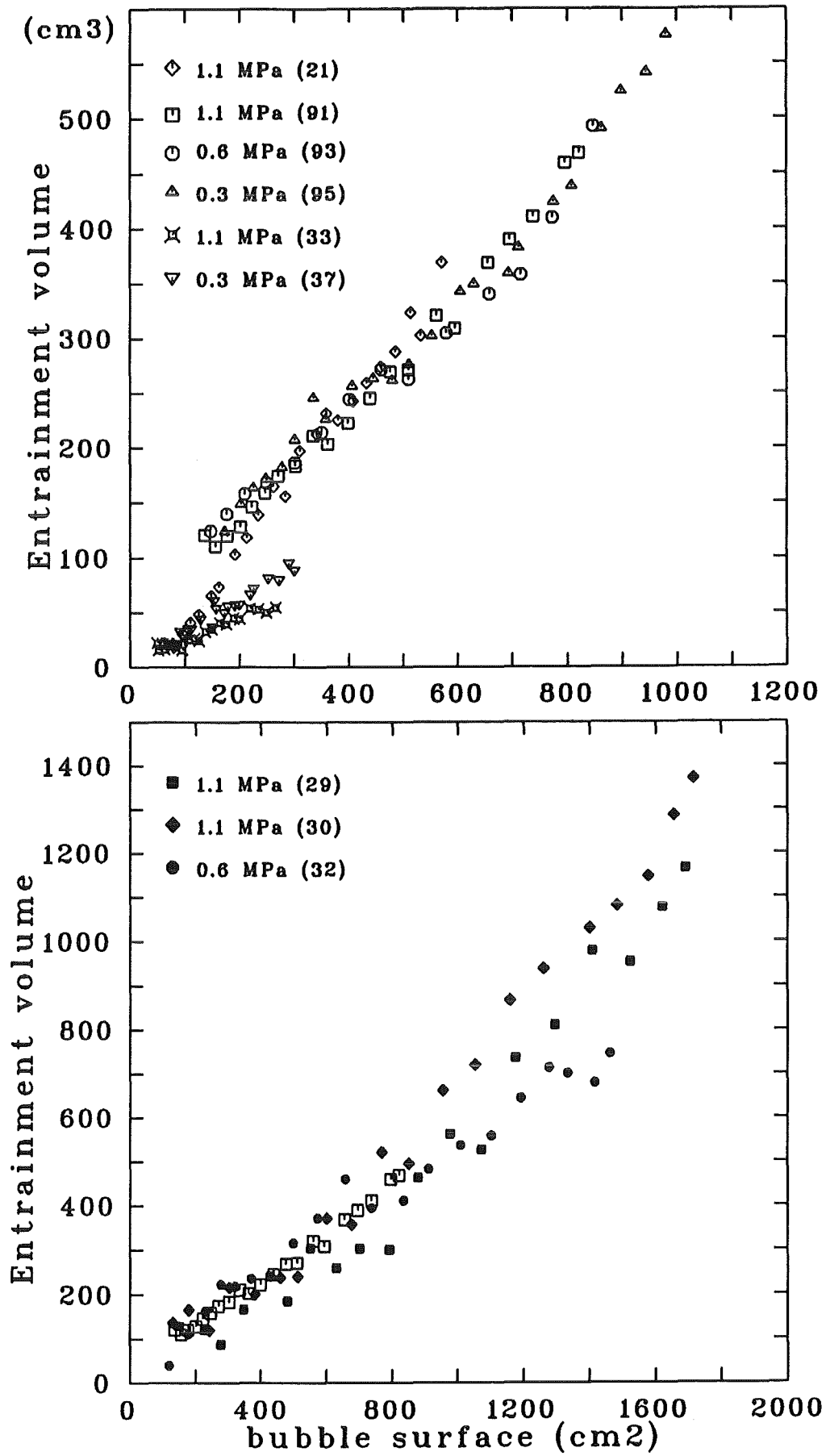
Fig. A.29 Entrainment volume versus vubble surface
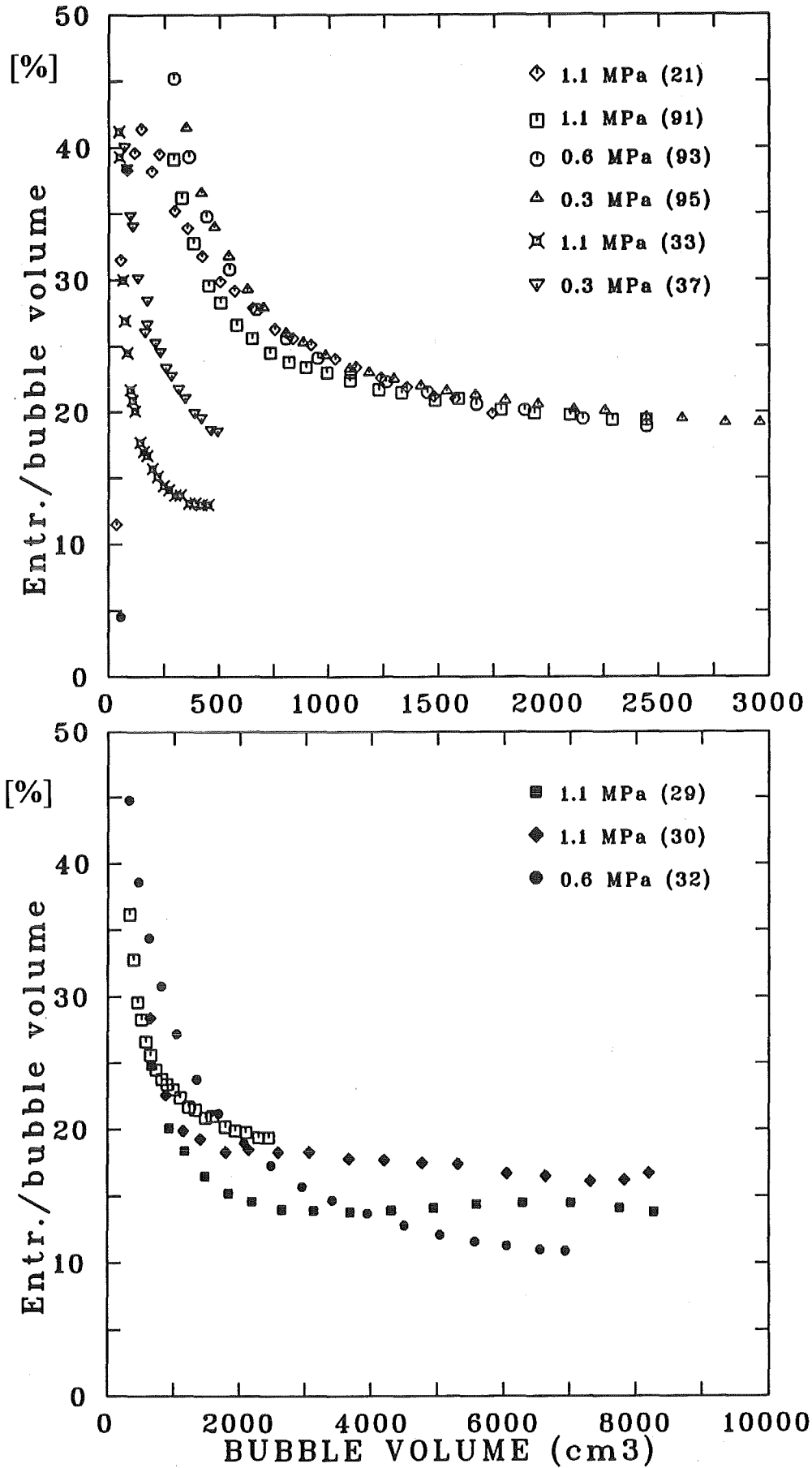
Fig. A.30 Relative entrainment volume versus bubble volume
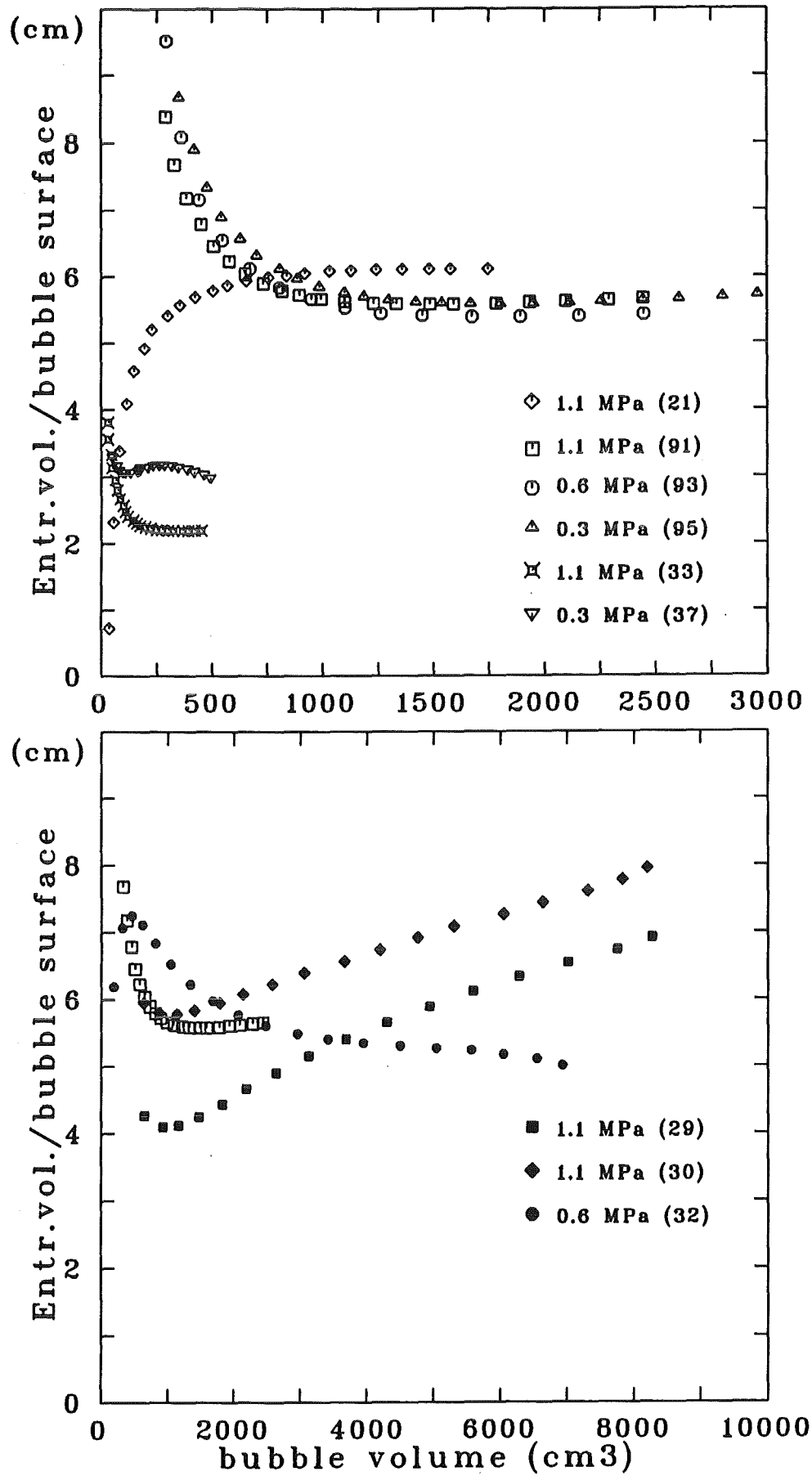
Fig. A.31 Entrainment thickness versus bubble volume
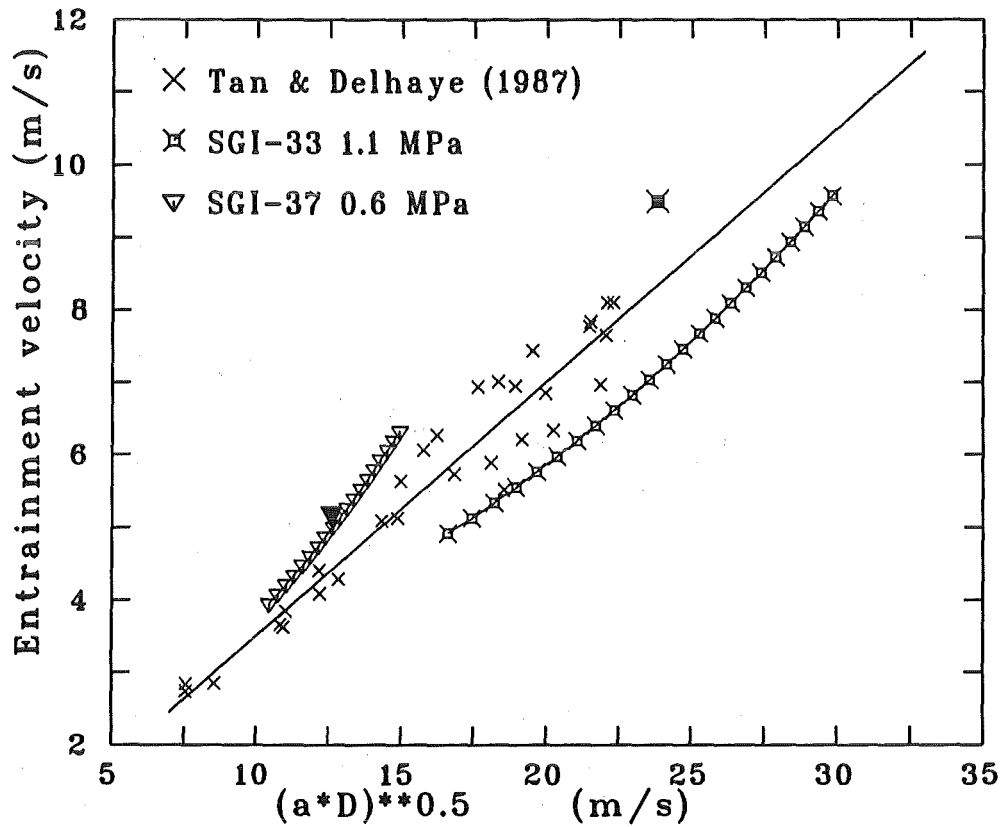
Fig. A.32 Entrainment velocity versus a function of acceleration and tube diameter according to Tan and Delhaye [9].
Open symbols : data of interface positions fitted by a third degree polynomial; full symbols and symbol ×: thickness (x_L-x_U) fitted by a linear function, water interface position x_U fitted by second order polynomial.
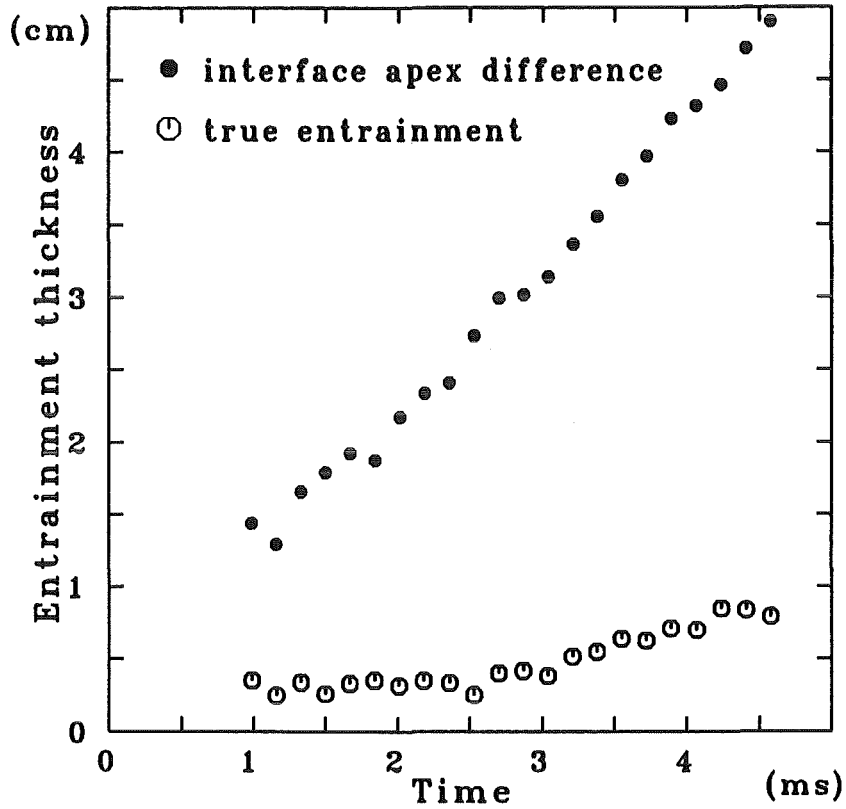
Fig. A 33 Comparison of two definitions of entrainment in test No.33:
full symbols: $(x_L - x_{Lo}) - (x_U - x_{Uo})$, according to Tan and Delhaye [9],
(index o stands for x at time zero); open symbols difference between
bubble volume and displaced water volume.
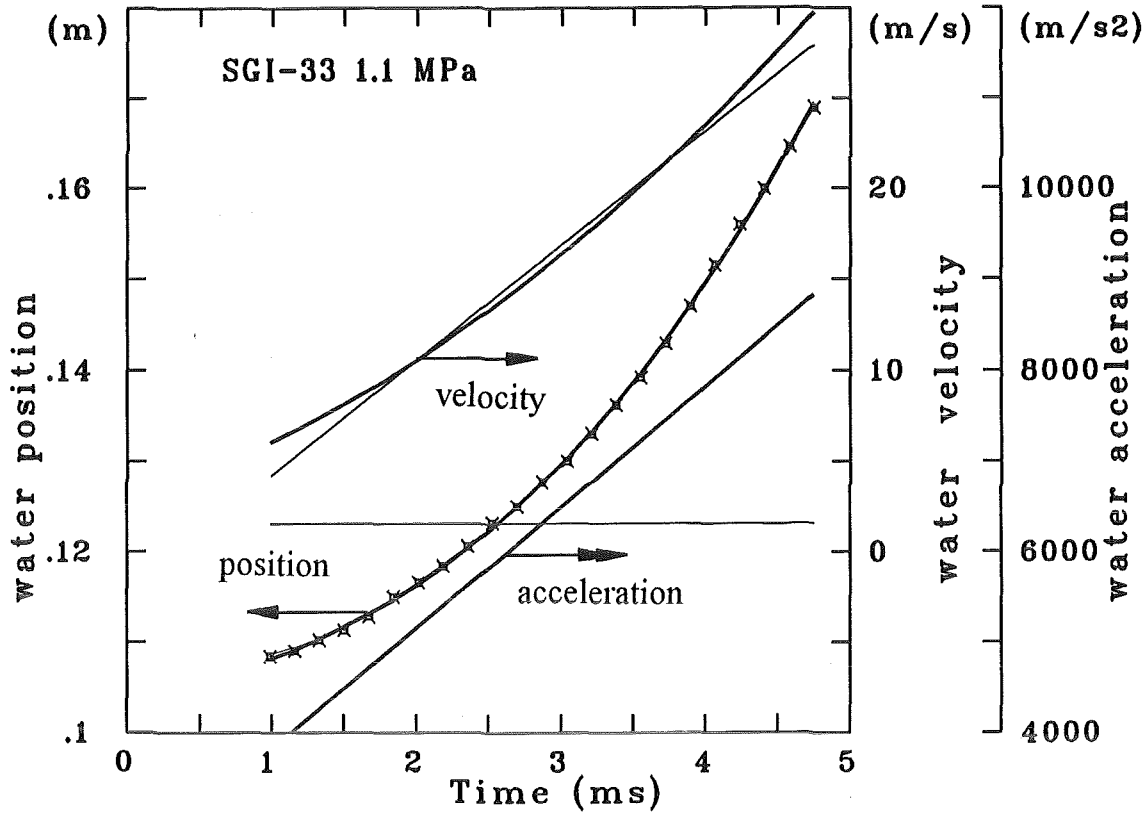
Fig. A34 Upper water interface positions x_U in test No.33 fitted by a second degree polynomial (thin lines) and by a third degree polynomial (thick lines), and their first and second derivations, the water velocity and acceleration, respectively.
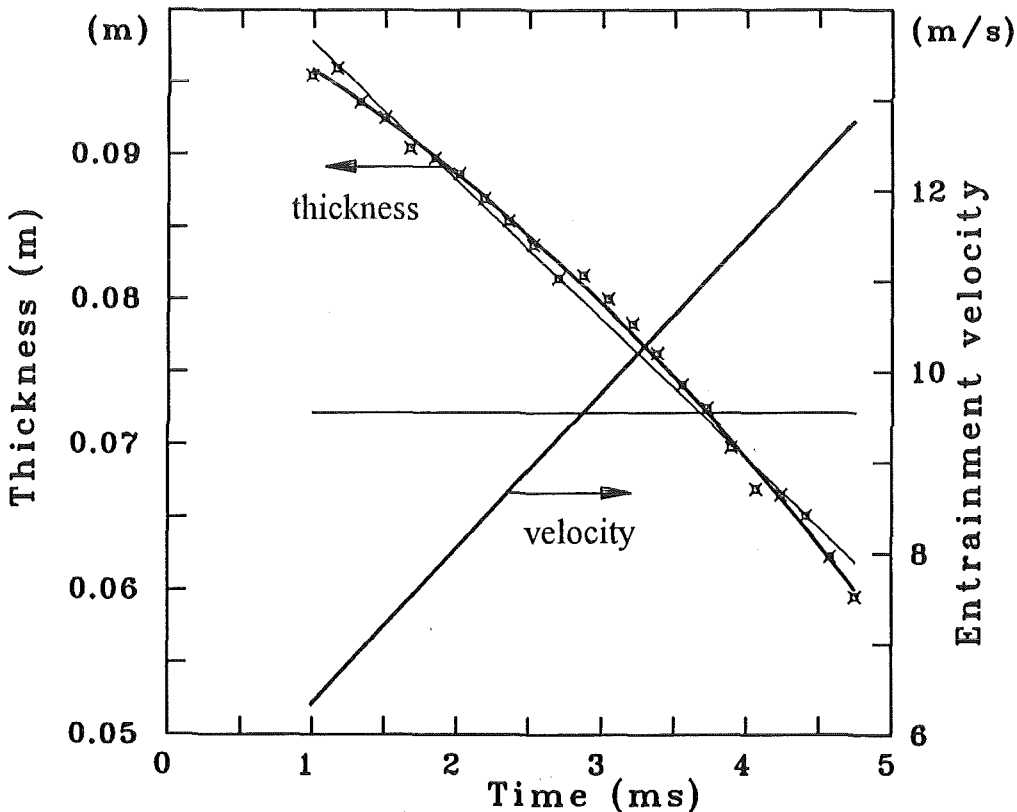
Fig. A.35 Water thickness $-(x_L-x_U)$ in test No.33 fitted by linear function (thin lines) and by second order polynomial (thick lines), and its derivation, the entrainment velocity, according to Tan and Delhaye.
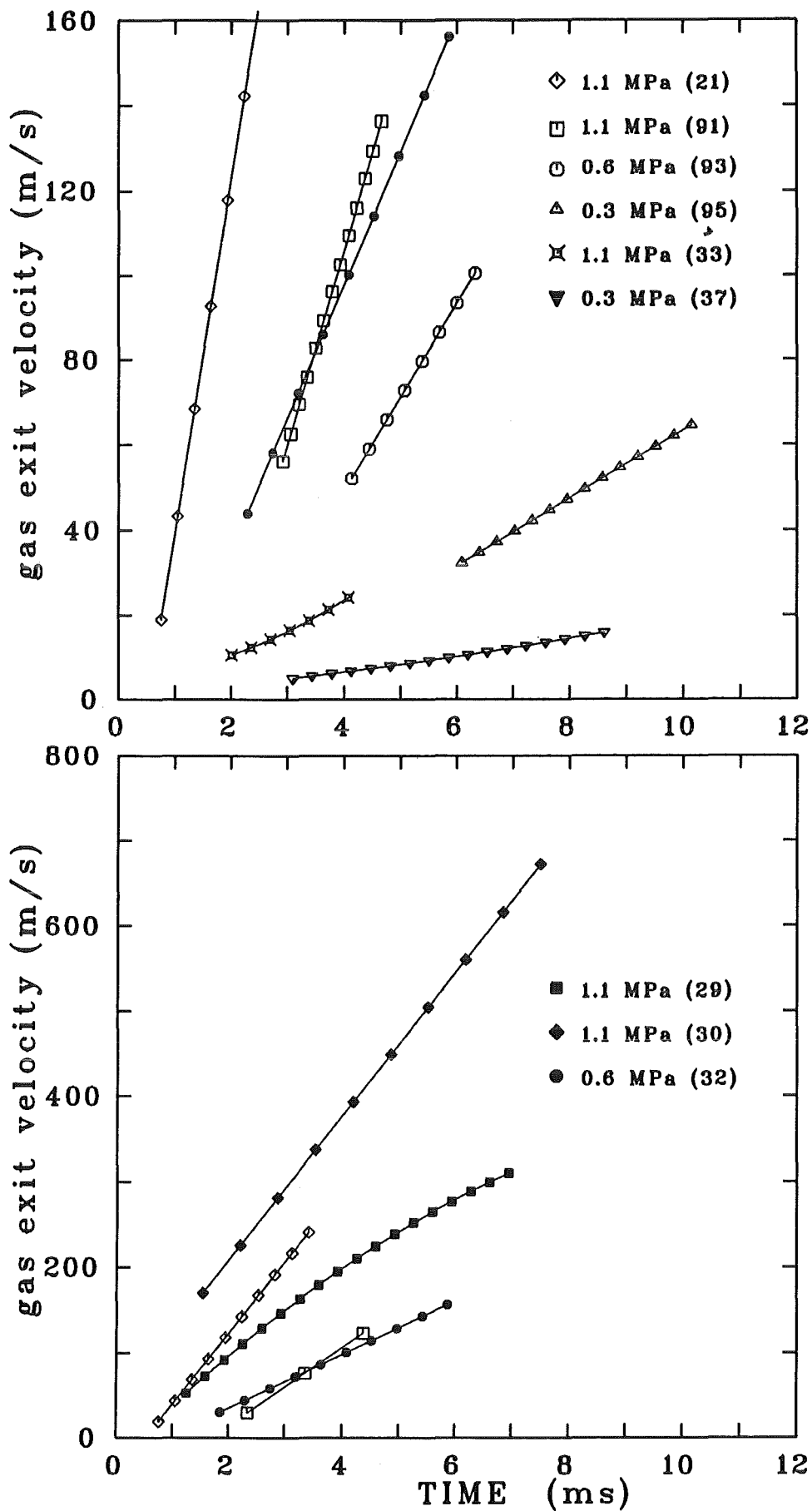
Fig. A.36 Gas velocity at nozzle exit
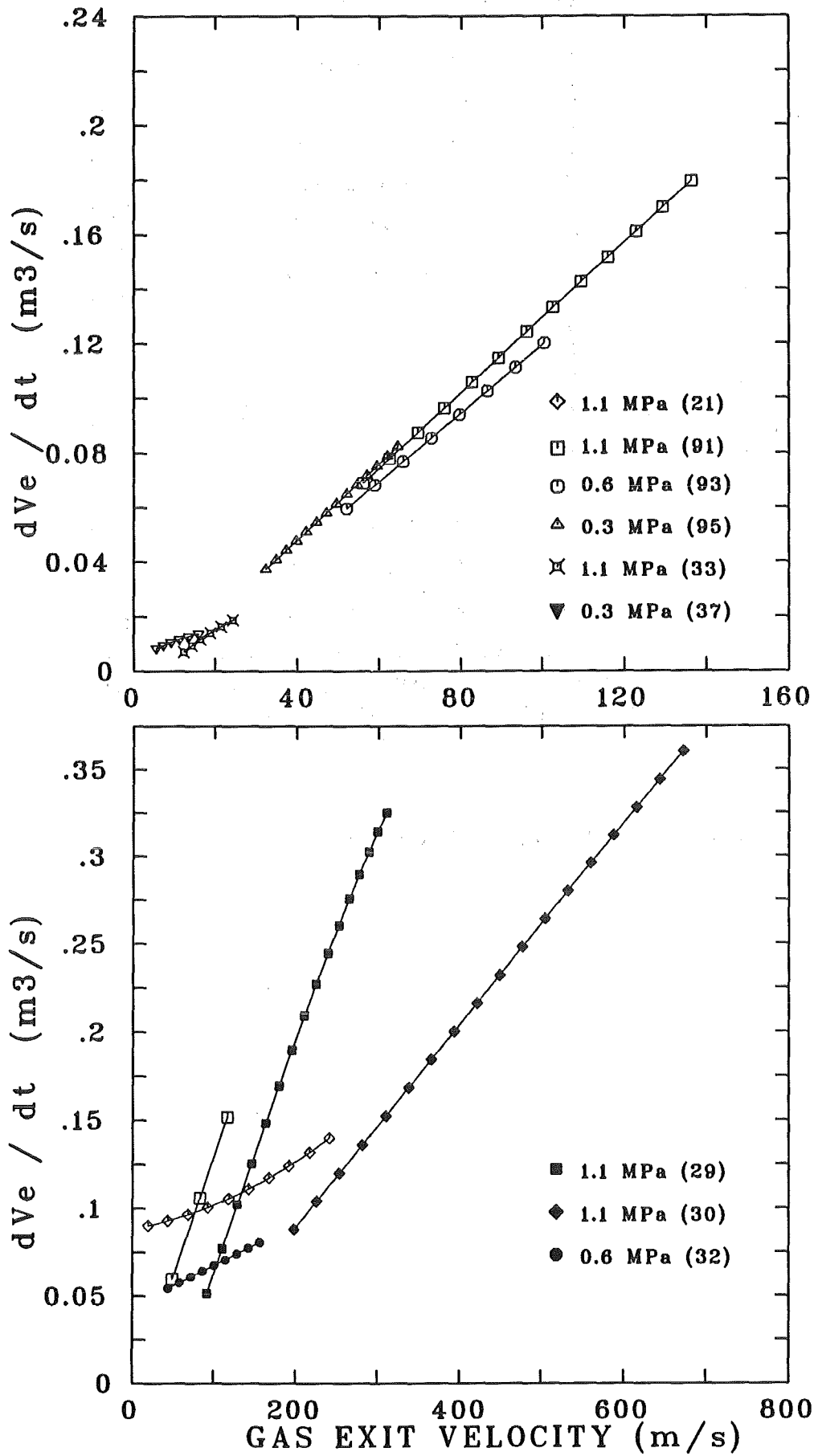
Fig. A.37 Volumetric entrainment rate versus gas velocity at nozzle exit
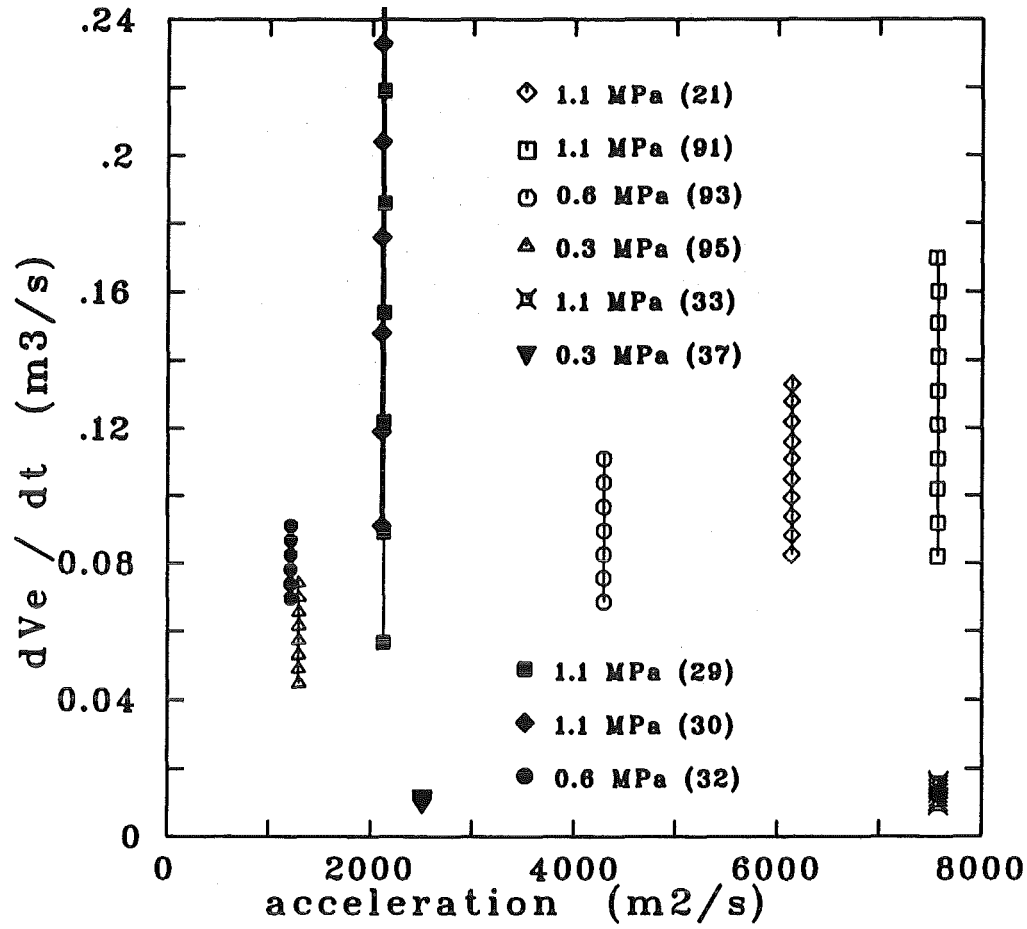
Fig. A.38 Volumetric entrainment rate versus axial acceleration of bubble interface

SGI-33

TIME = .0033 s

VAPOR VELOCITIES
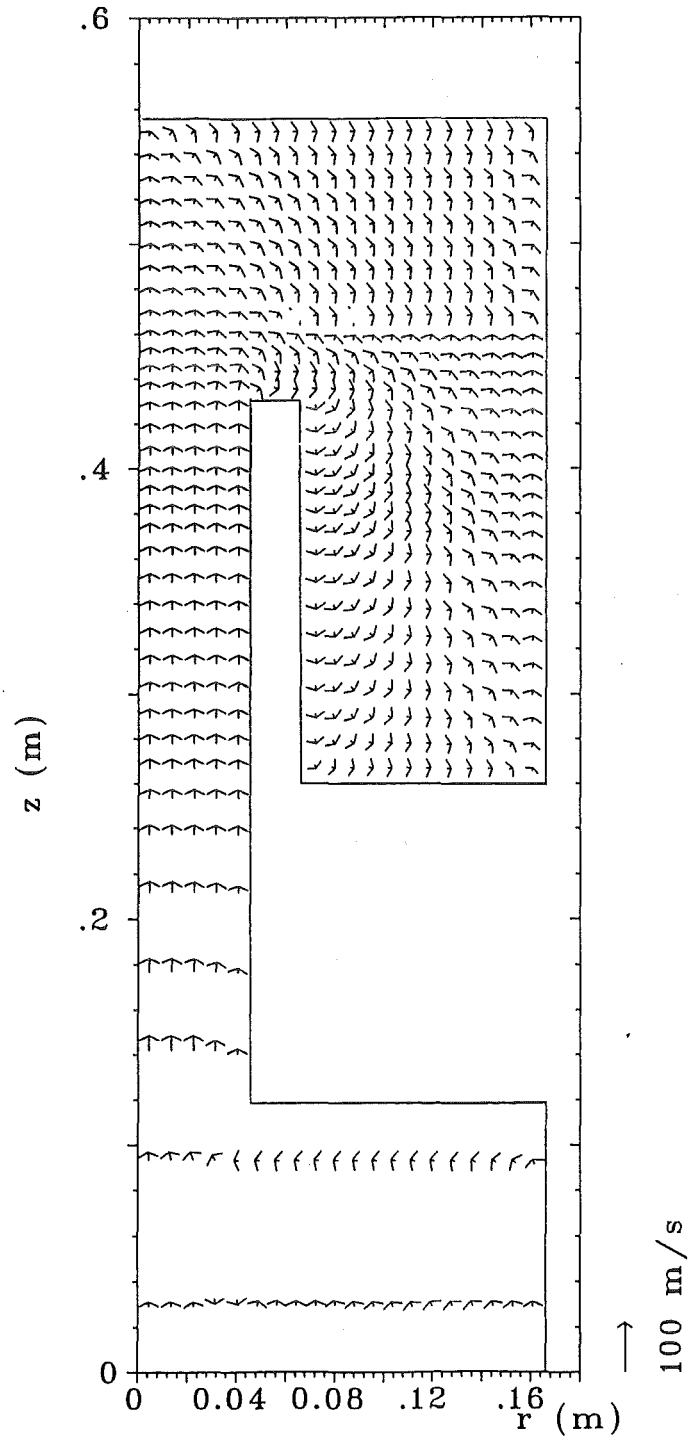
Fig. B.1. Cross section of the right side of the AFDM model for SGI-33 with velocity vectors
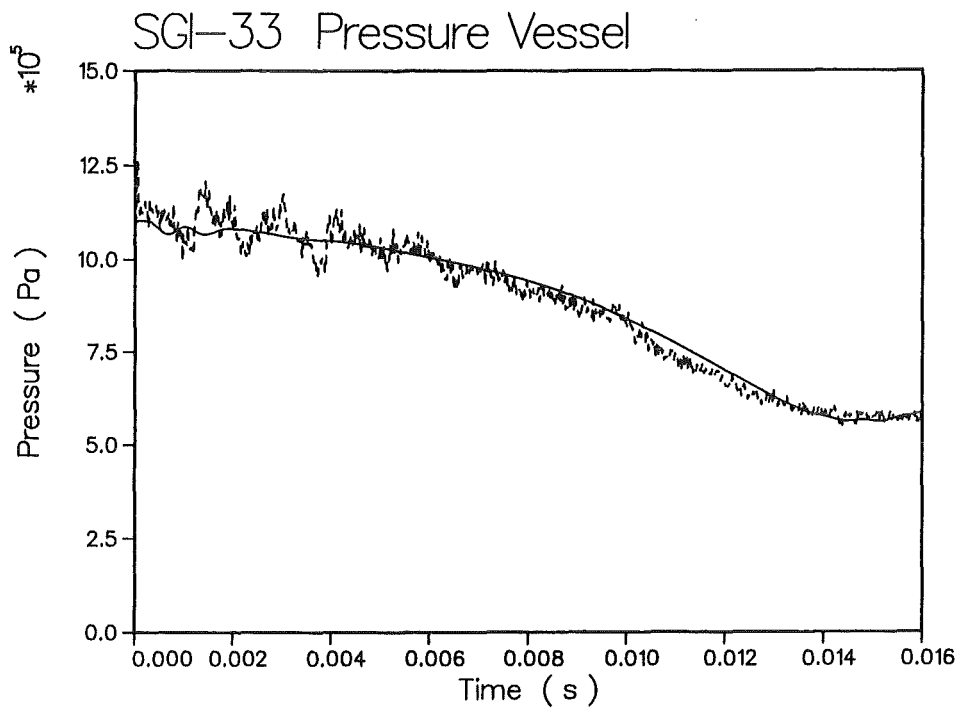
Fig. B.2. AFDM pressure (solid line) and experimental pressure (dashed line) for SGI-33
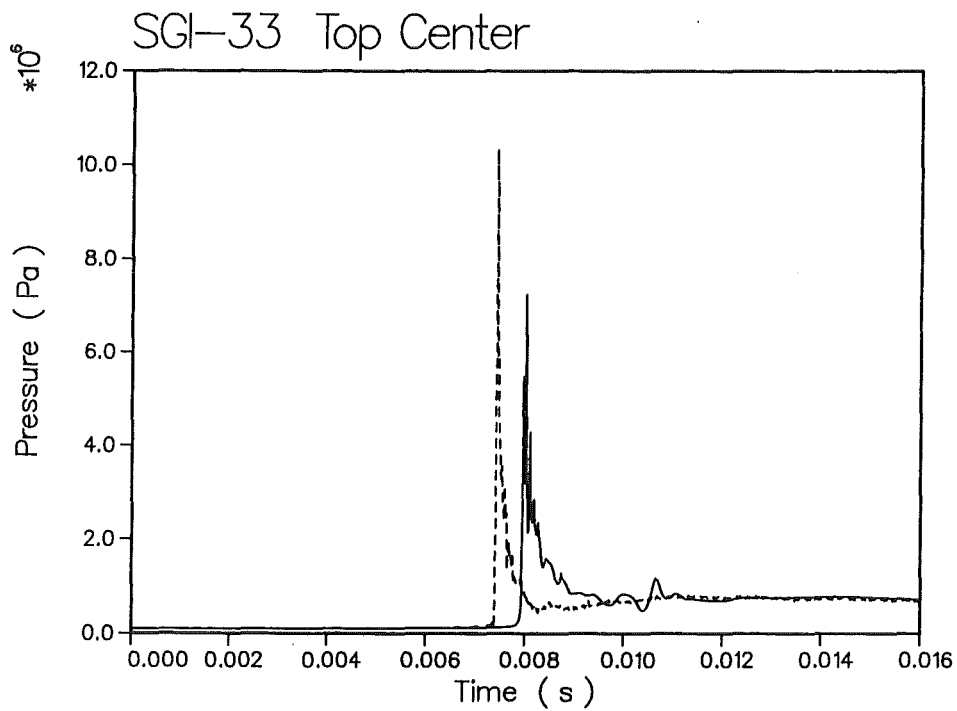
Fig. B.3. AFDM pressure (solid line) and experimental pressure (dashed line) for SGI-33
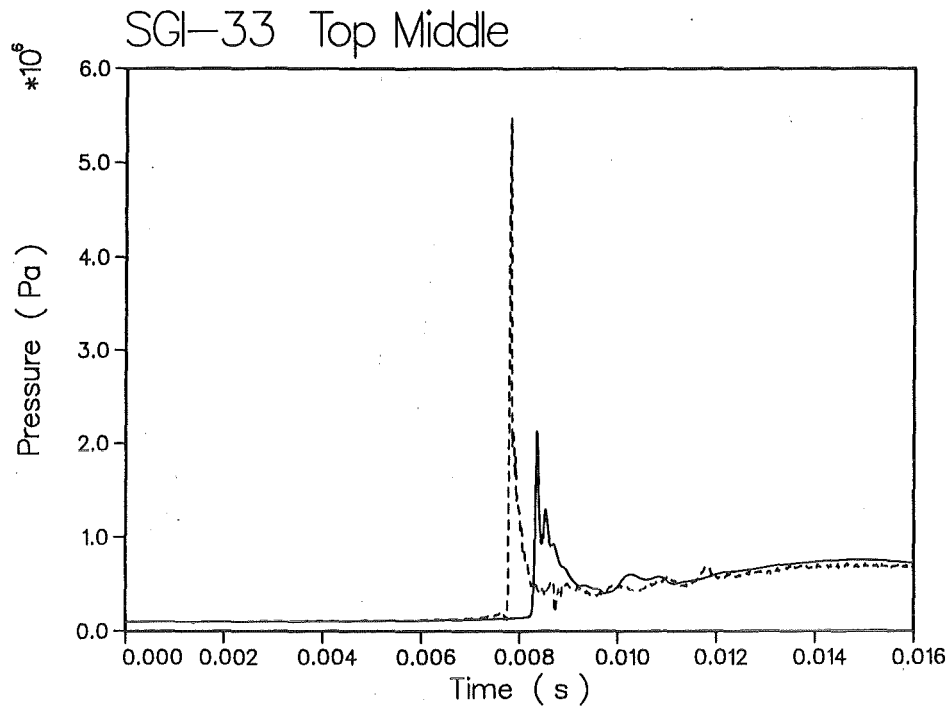
Fig. B.4. AFDM pressure (solid line) and experimental pressure (dashed line) for SGI-33
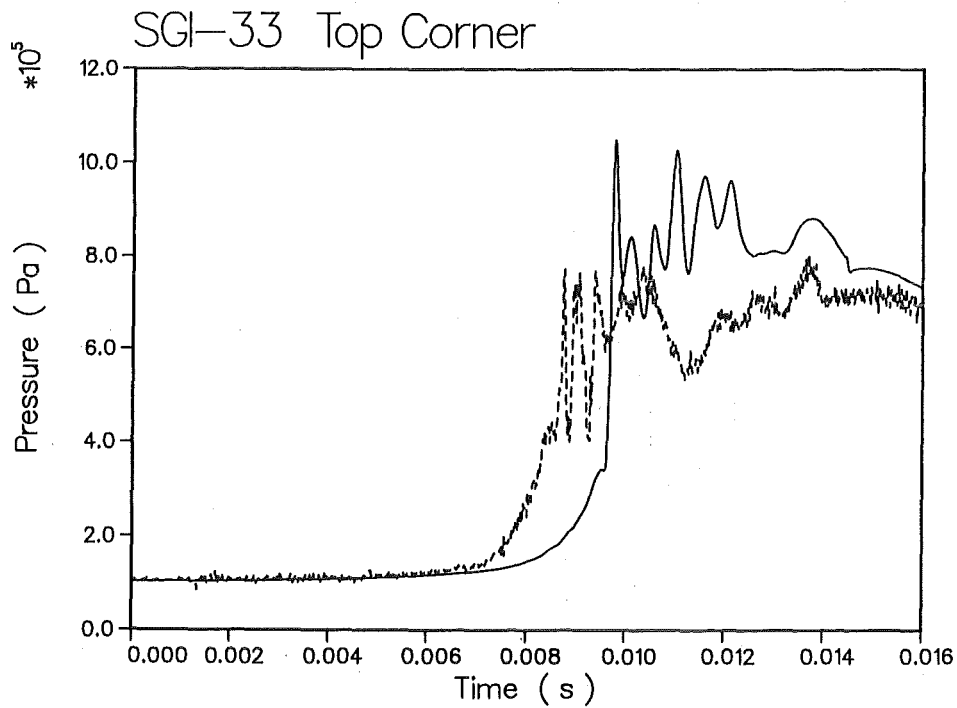
Fig. B.5. AFDM pressure (solid line) and experimental pressure (dashed line) for SGI-33

SGI-33

Time at: .0035, .0040, .0045, .0050, .0055 s

Traverse at Radius: .004
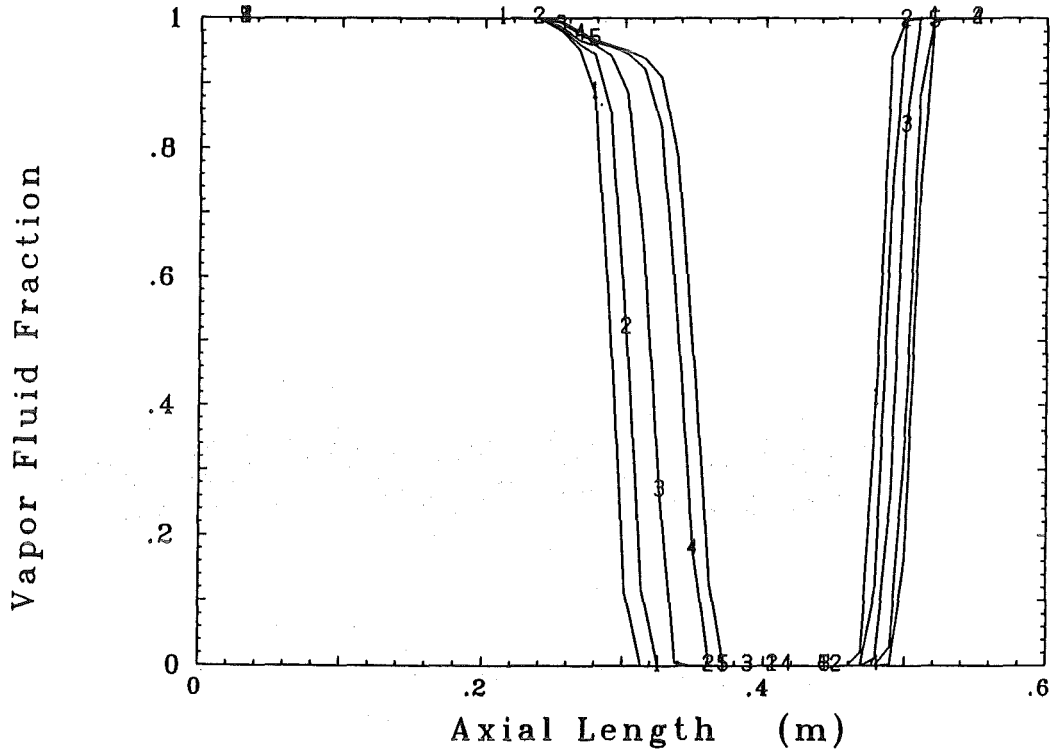
Fig. B.6. AFDM void fractions at different times for SGI-33

SGI-33   Time: .0055 s

vapor fluid fraction
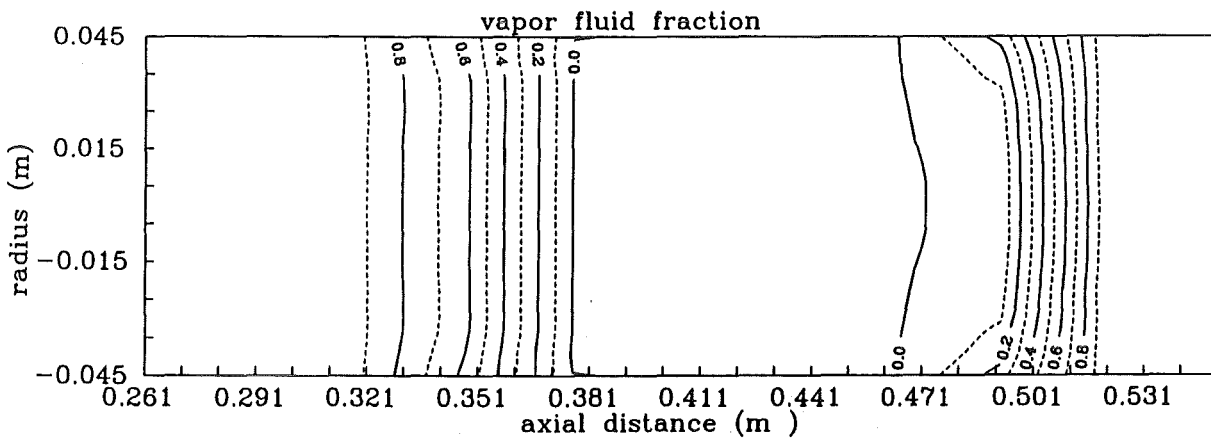
Fig. B.7. AFDM void fraction contours at 5.5ms for SGI-33

SGI−33
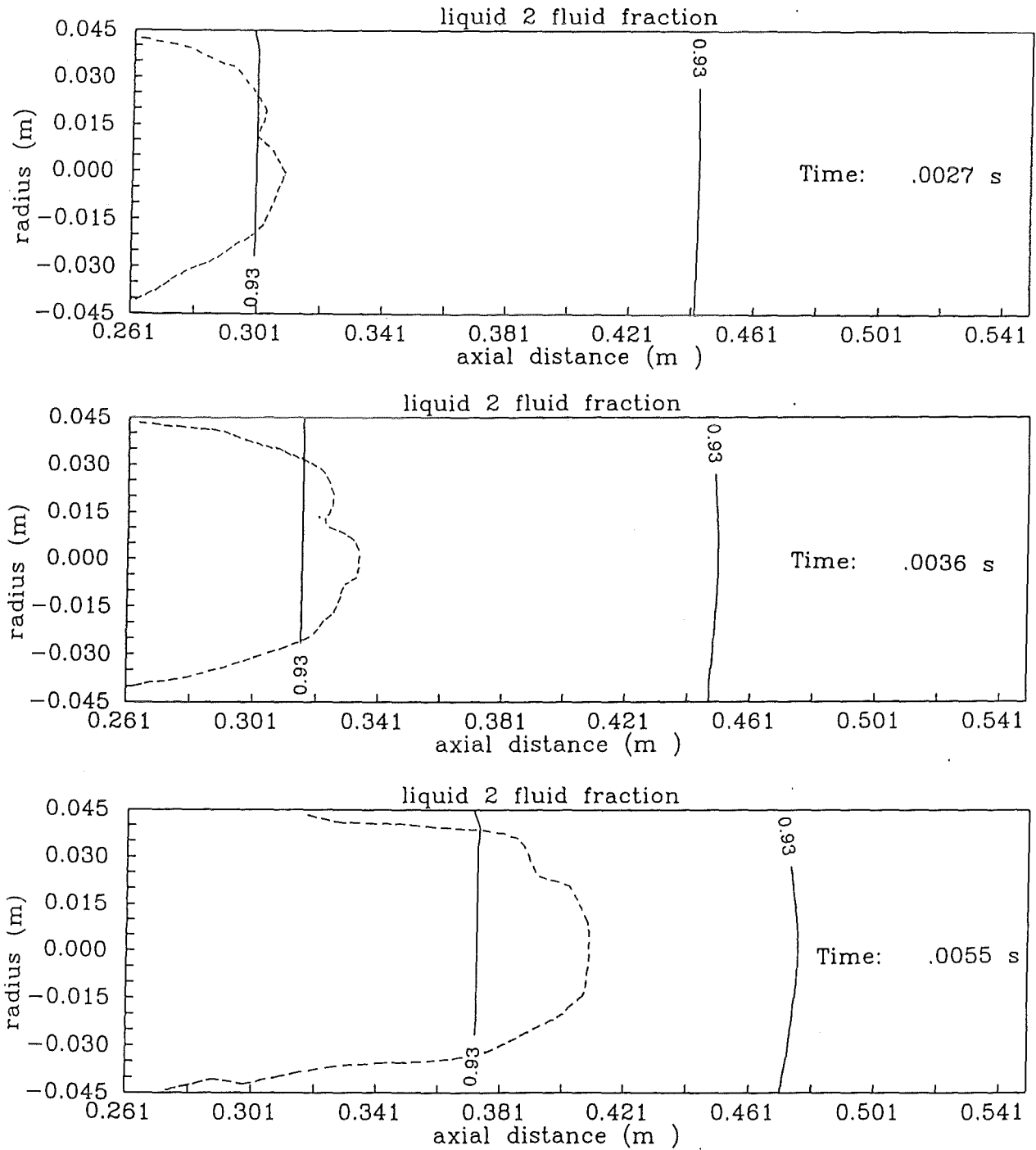
Fig. B.8. Comparison of SGI-33 void fraction contours between experiment (dashed) and AFDM (solid lines)

SGI-33   Time: .0058 s

liquid 2 fluid fraction
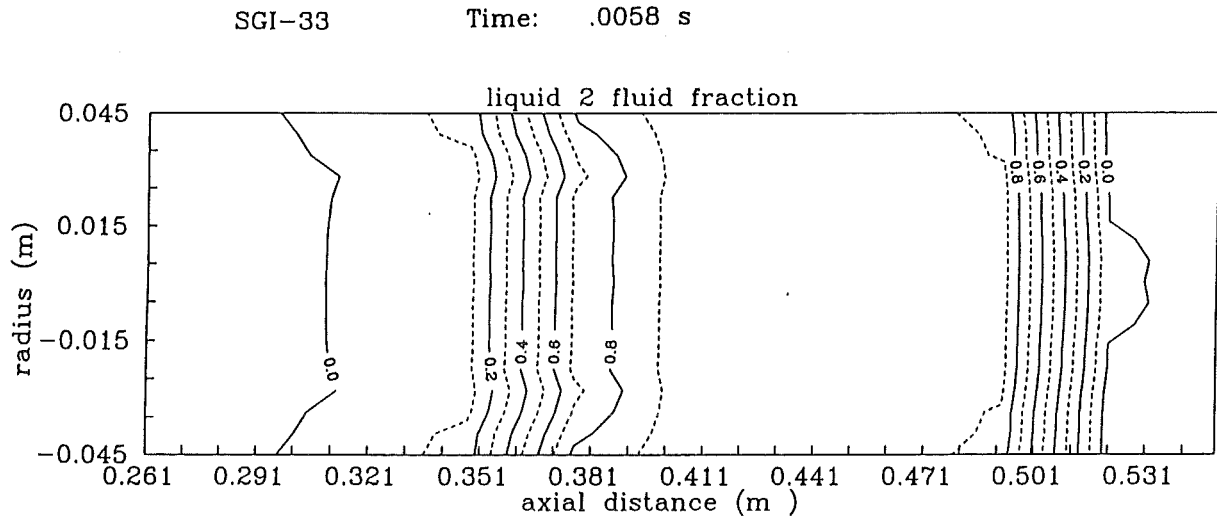
Fig. B.9. AFDM water volume fraction contours at 5.8ms for SGI-33 with non standard wall model

SGI-33
  Time at: 9.9, 6.2, 4.3, 3.1 ms
  Traverse at Radius: .004 m

- - - - 0.5 MPa, 9.9 ms
——— 1.1 MPa, 6.2 ms
—·—·· 2.2 MPa, 4.3 ms
- - - - - - - 4.4 MPa, 3.1 ms
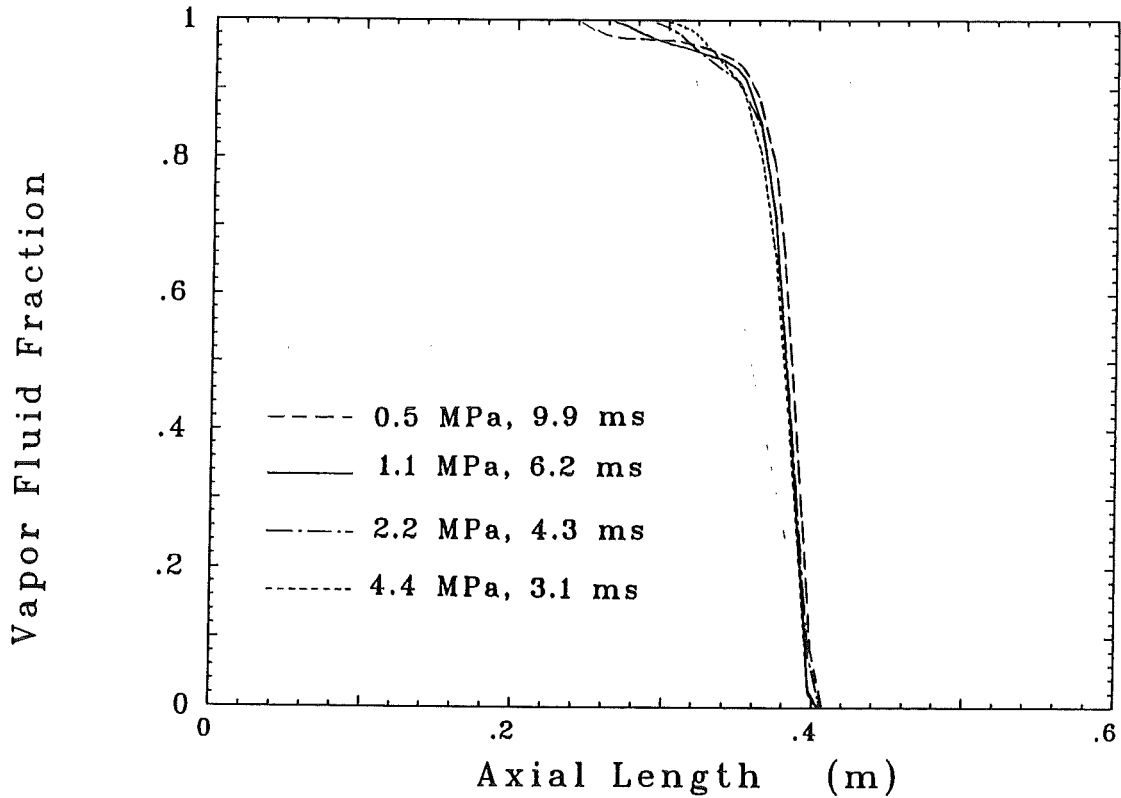
Fig. B.10. AFDM void fractions for different accelerations

SGI-29

FLUID MESH
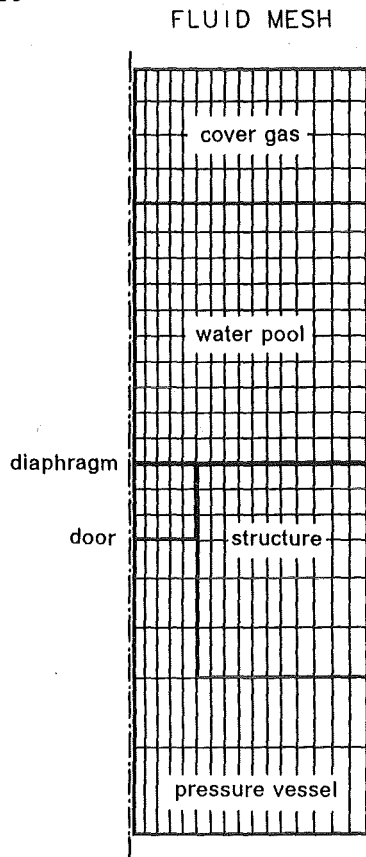
Fig. B.11. AFDM mesh cell set for SGI-29, right side of cylinder

CELL TRACE- SGI-29   PRESSURE VESSEL
1(1, 1)
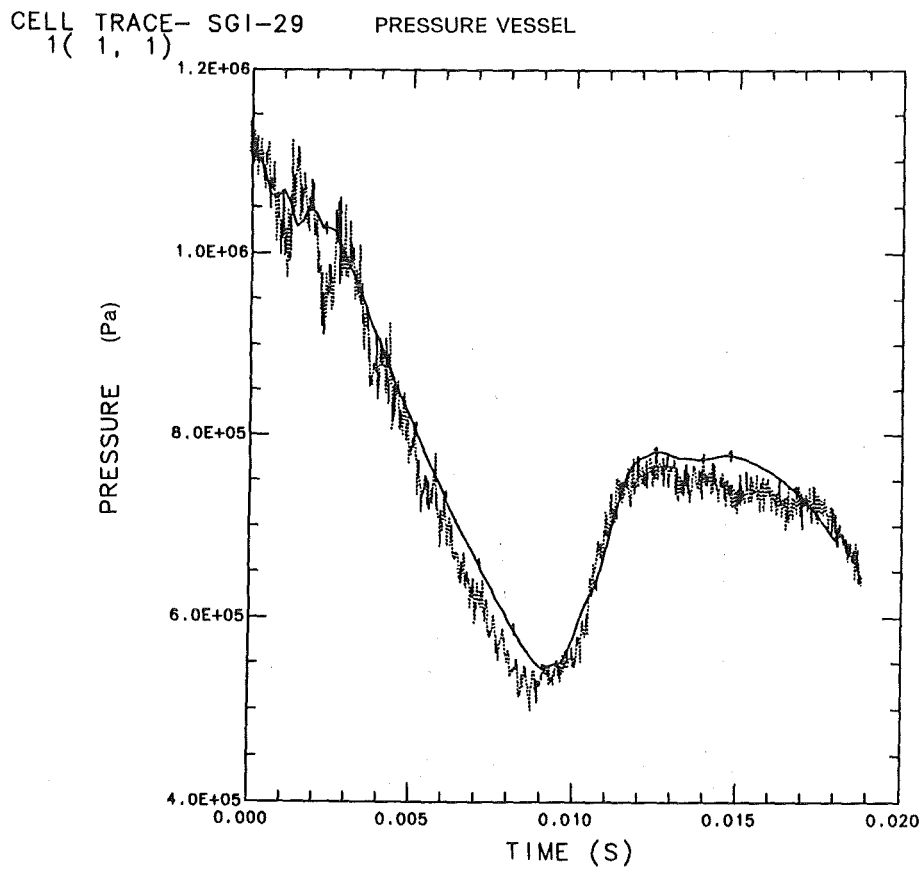
Fig. B.12. AFDM pressure (solid line) and experimental pressure (dashed line) for SGI-29

CELL TRACE- SGI-29.   NOZZLE
  1(5, 7)
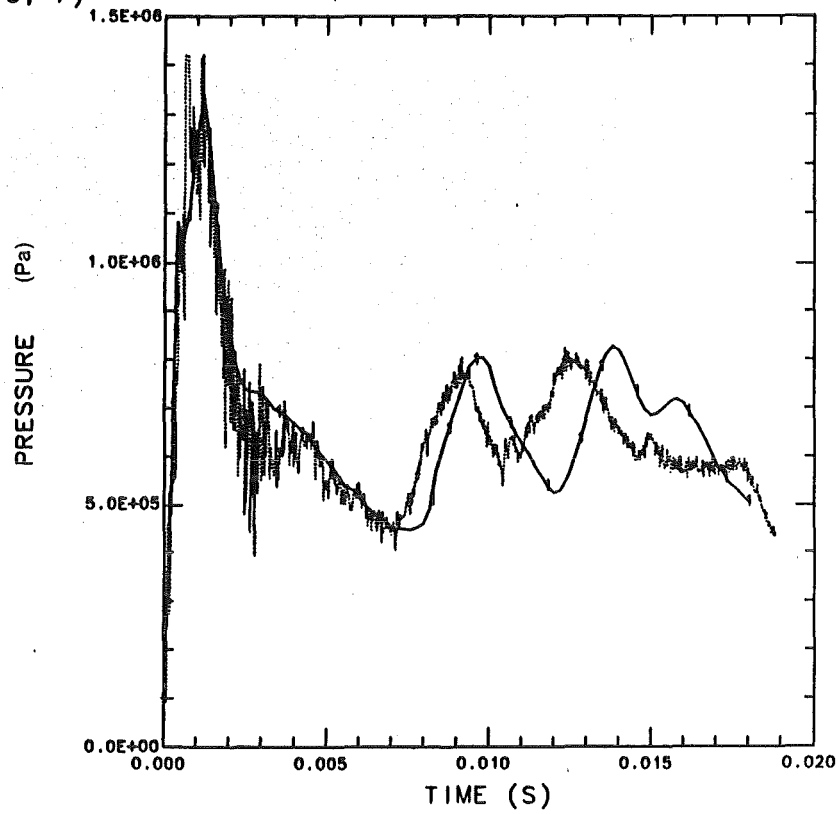
Fig. B.13. AFDM pressure (solid line) and experimental pressure (dashed line) for SGI-29

CELL TRACE- SGI-29   TOP CENTER
  1(1,22)

Fig. B.14. AFDM pressure (solid line) and experimental pressure (dashed line) for SGI-29

TIME   0.910 MS
SGI-29 LIQUID VOLUME FRACTION CONTOUR

TIME   2.250 MS
SGI-29 LIQUID VOLUME FRACTION CONTOUR

The dotted line is the outer edge of the
two-phase bubble clearly visible in the experiment

AFDM contours (solid lines) are
defined at void fractions 0.04 and 0.07

TIME   3.590 MS
SGI-29 LIQUID VOLUME FRACTION CONTOUR

TIME   4.930 MS
SGI-29 LIQUID VOLUME FRACTION CONTOUR

TIME   5.600 MS
SGI-29 LIQUID VOLUME FRACTION CONTOUR

TIME   6.940 MS
SGI-29 LIQUID VOLUME FRACTION CONTOUR
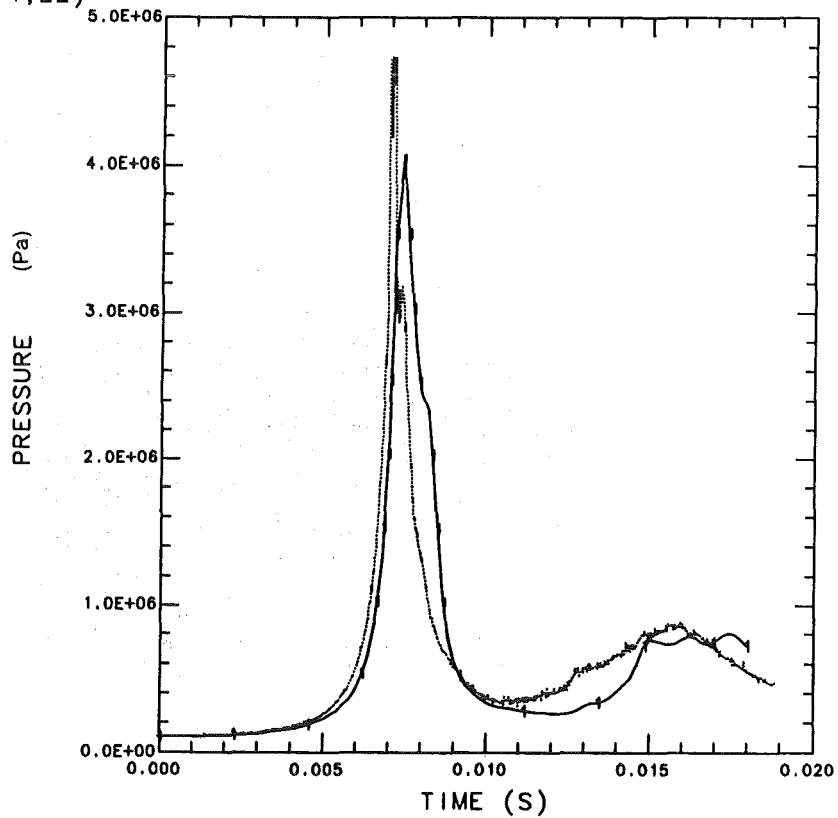
Fig. B.15. Comparison of SGI-29 void fraction contours between experiment and AFDM

SGI-29 16x22
Time= .0056s
 Traverse at Length: .310, .328, .346, .364, .382, .400
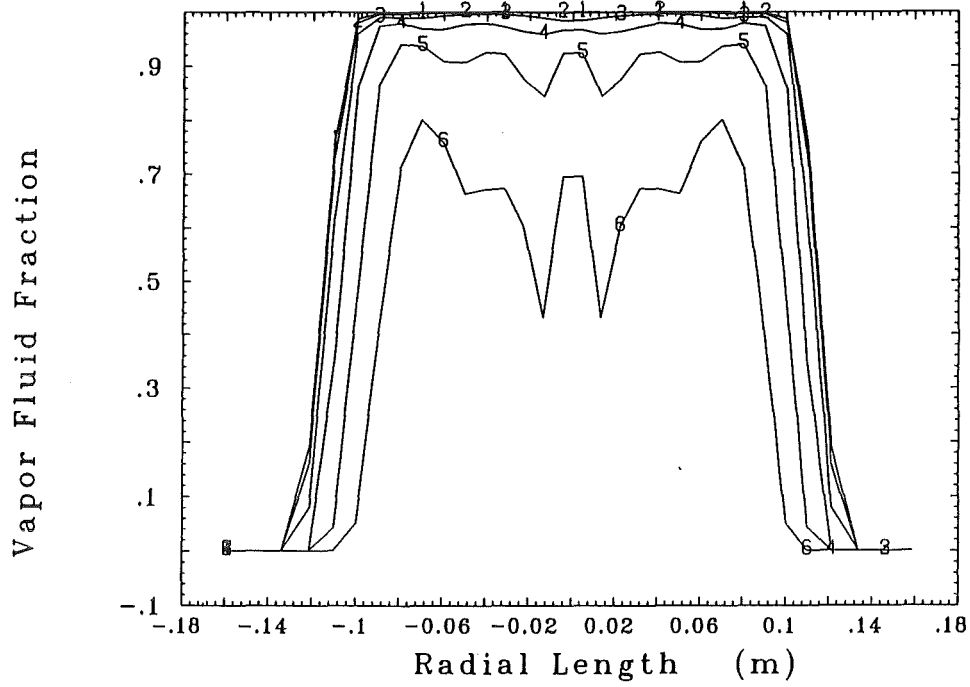
Fig. B.16. AFDM radial void fraction distribution for standard mesh size

SGI-29 5x22
Time= .0056s
 Traverse at Length: .310, .328, .346, .364, .382, .400
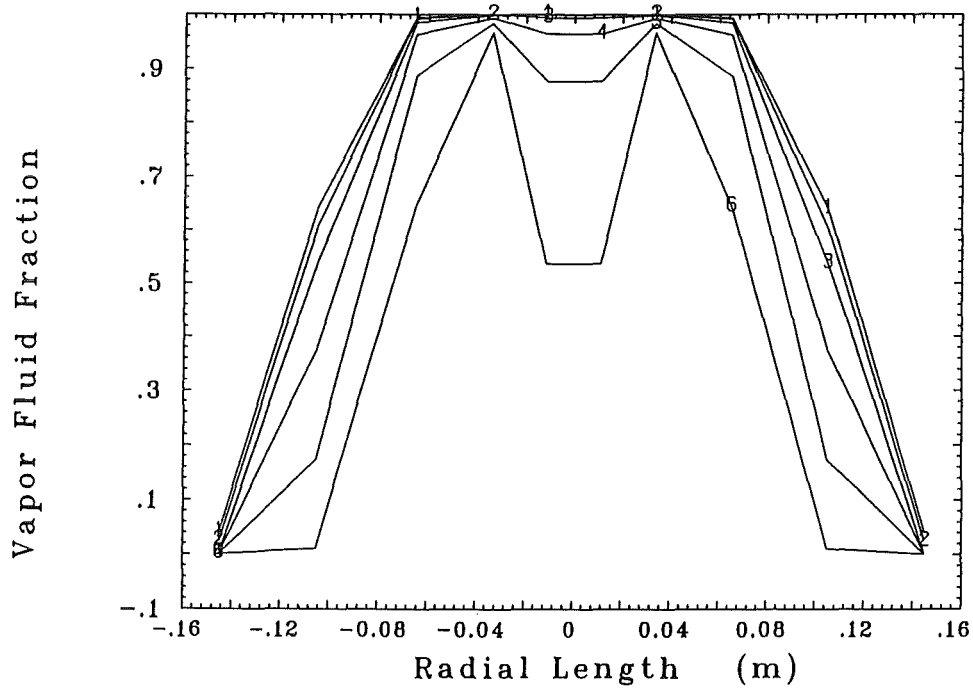
Fig. B.17. AFDM radial void fraction distribution for coarse mesh size

Time: .0056 s
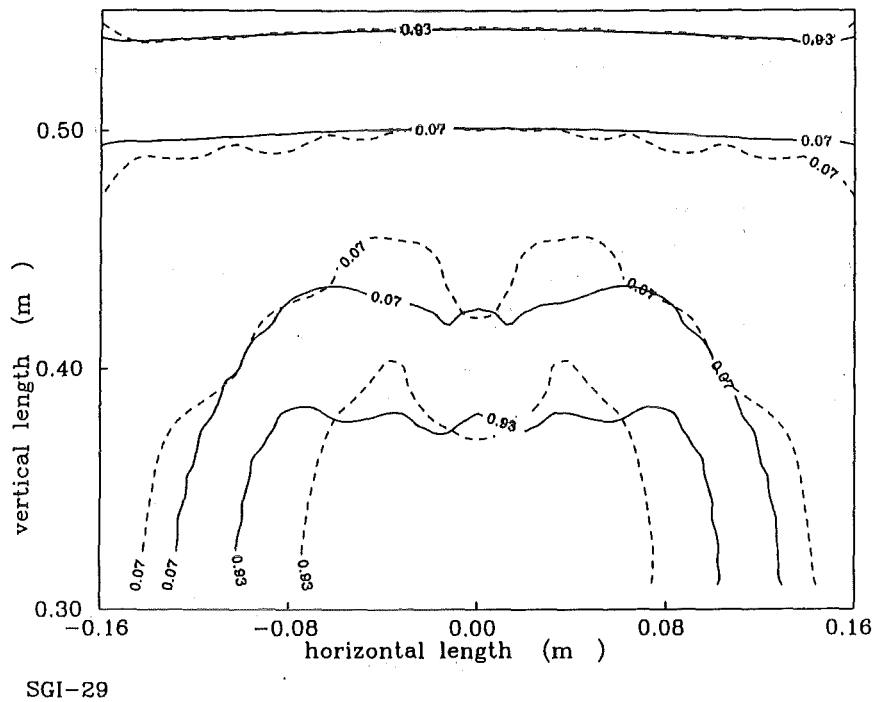
SGI-29

Fig. B.18. Comparison of AFDM void fraction contours between standard (solid) and coarse mesh (dashed lines) of SGI-29
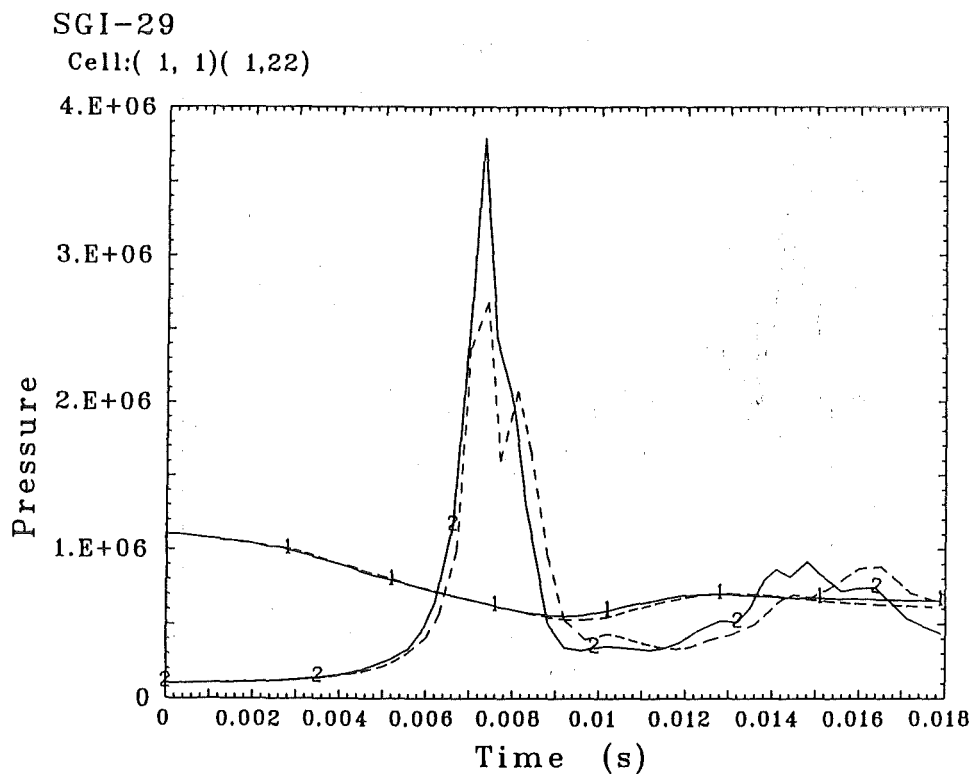
SGI-29
Cell:(1, 1)(1,22)

Fig. B.19. Comparison of AFDM pressures between standard (solid) and coarse mesh (dashed lines) of SGI-29
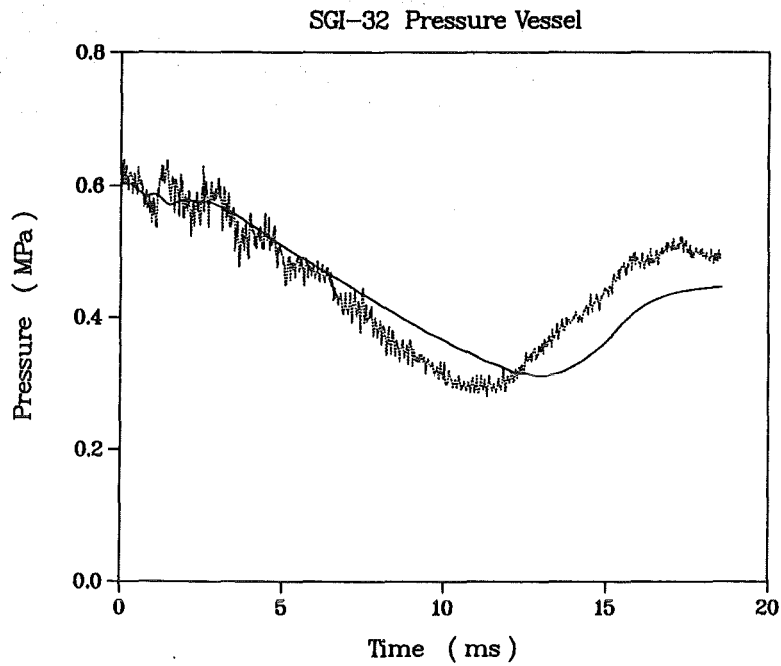
Fig. B.20. AFDM pressure (solid line) and experimental pressure (dotted line) for SGI-32
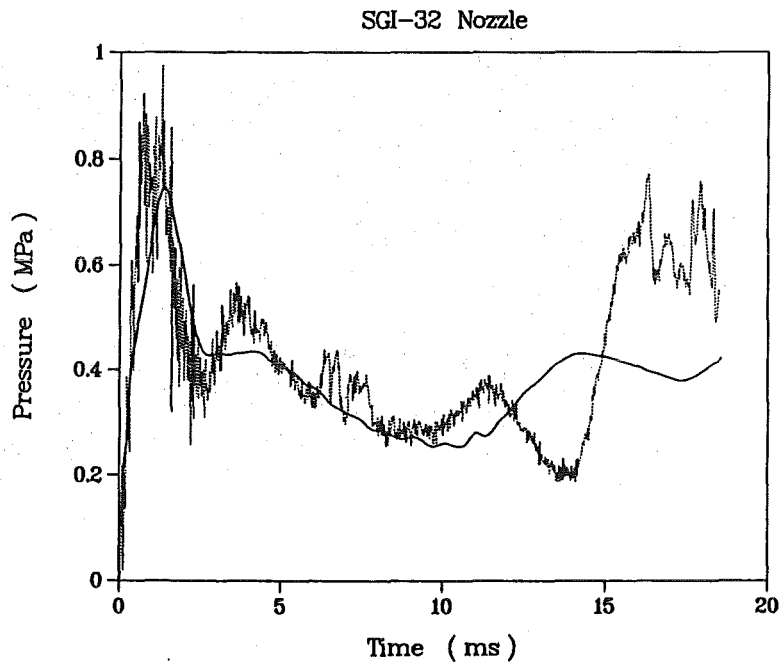
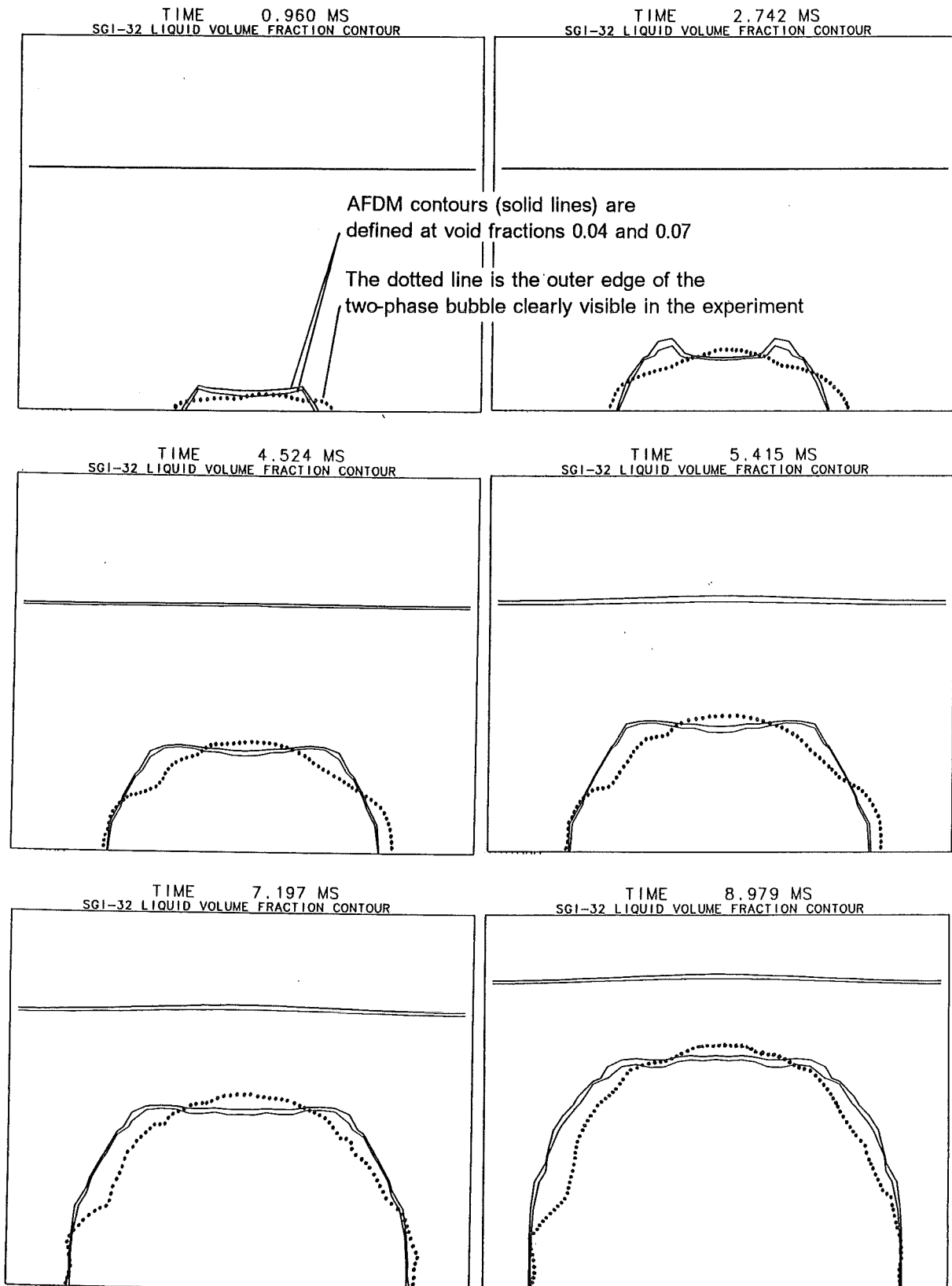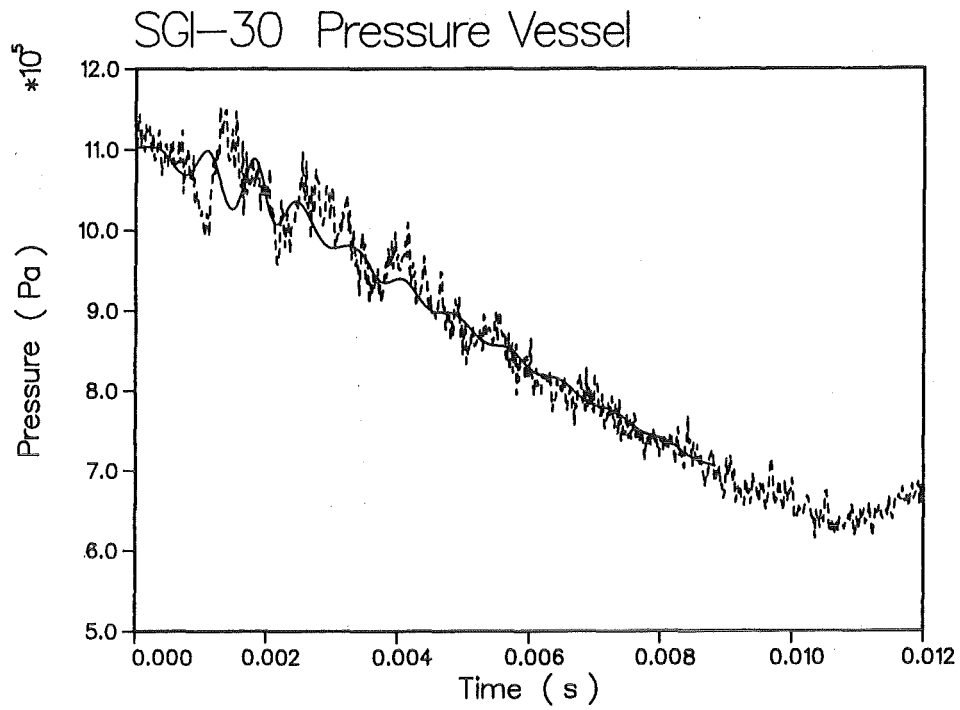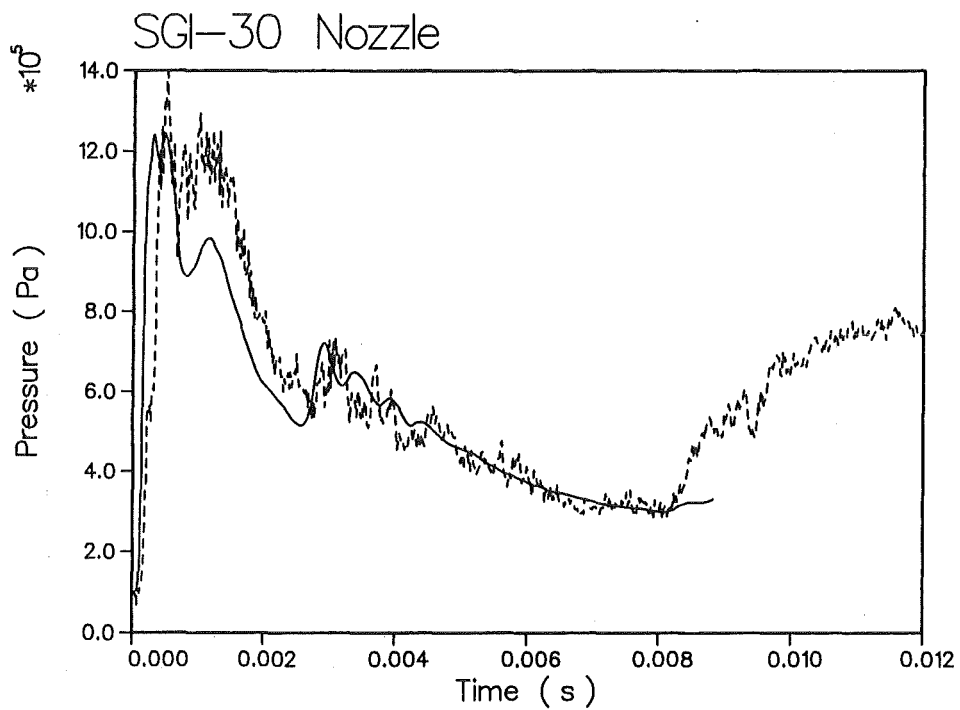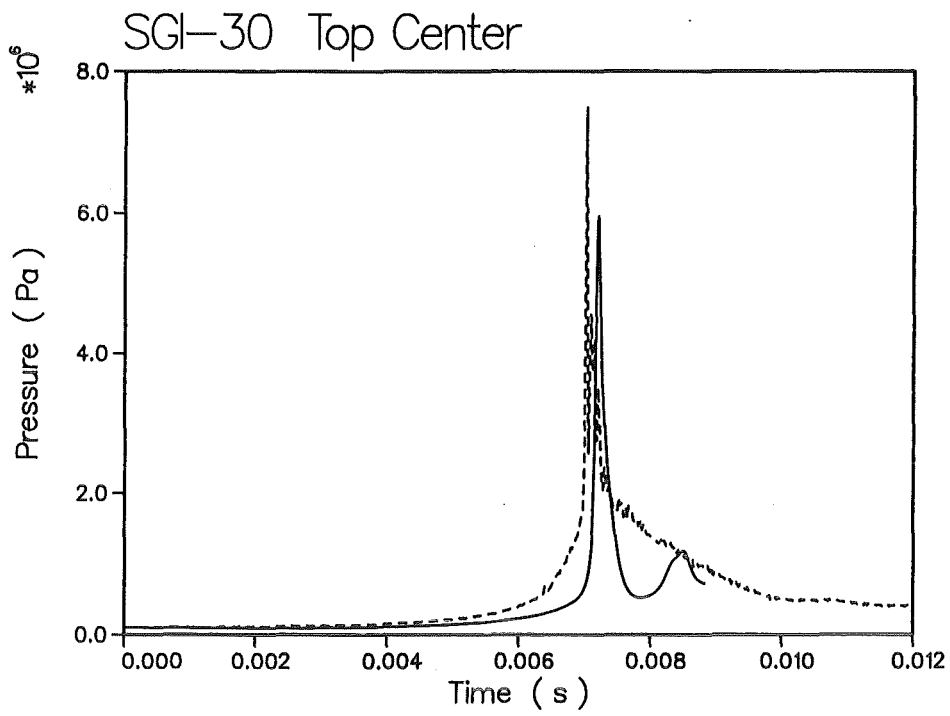**Fig. B.21.** AFDM pressure (solid line) and experimental pressure (dotted line) for SGI-32
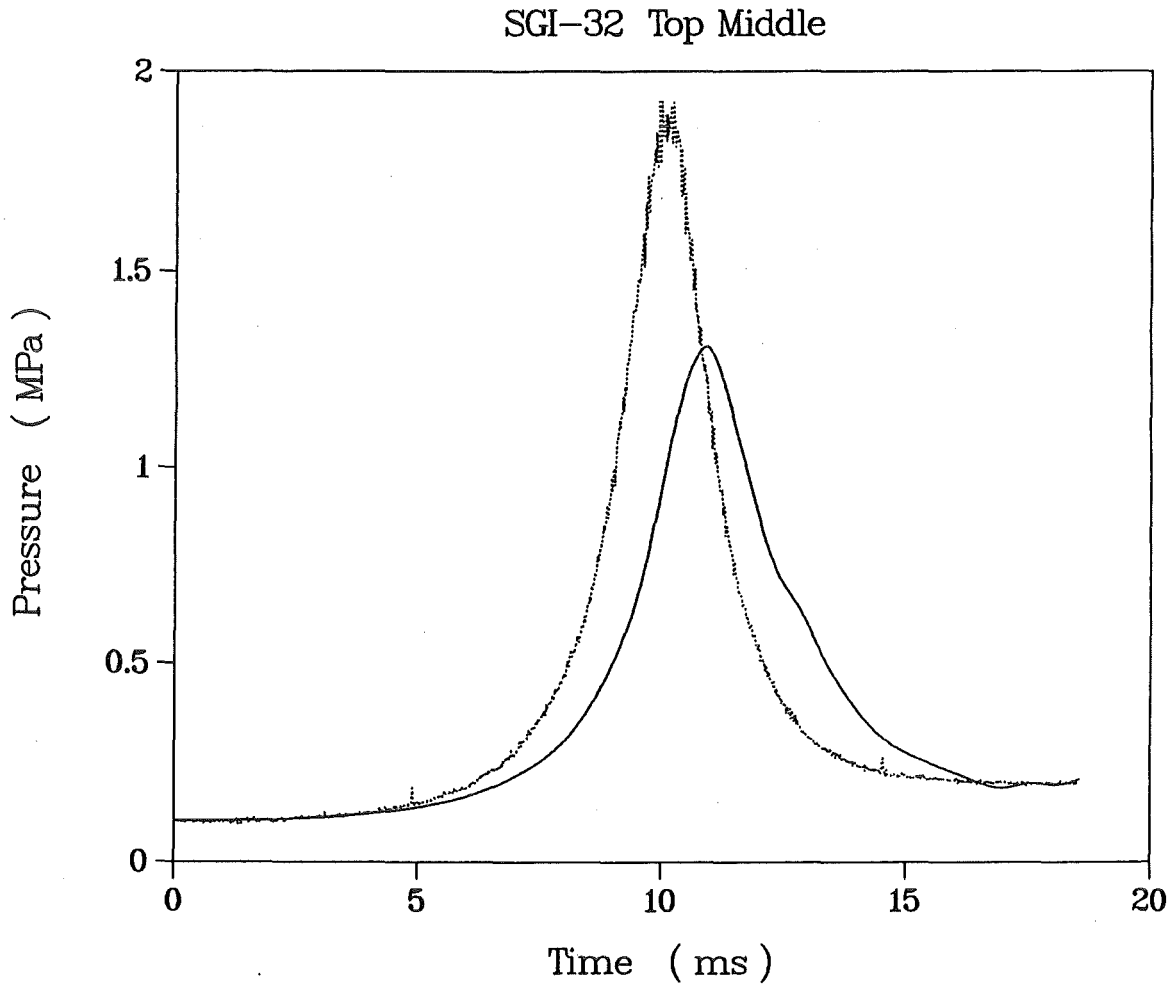
SGI–32 Top Middle

Fig. B.22. AFDM pressure (solid line) and experimental pressure (dotted line) for SGI-32

TIME   0.960 MS
SGI-32 LIQUID VOLUME FRACTION CONTOUR

TIME   2.742 MS
SGI-32 LIQUID VOLUME FRACTION CONTOUR

AFDM contours (solid lines) are
defined at void fractions 0.04 and 0.07

The dotted line is the outer edge of the
two-phase bubble clearly visible in the experiment

TIME   4.524 MS
SGI-32 LIQUID VOLUME FRACTION CONTOUR

TIME   5.415 MS
SGI-32 LIQUID VOLUME FRACTION CONTOUR

TIME   7.197 MS
SGI-32 LIQUID VOLUME FRACTION CONTOUR

TIME   8.979 MS
SGI-32 LIQUID VOLUME FRACTION CONTOUR

Fig. B.23. Comparison of SGI-32 void fraction contours between experiment and AFDM

Fig. B.24. AFDM pressure (solid line) and experimental pressure (dashed line) for SGI-30

Fig. B.25. AFDM pressure (solid line) and experimental pressure (dashed line) for SGI-30

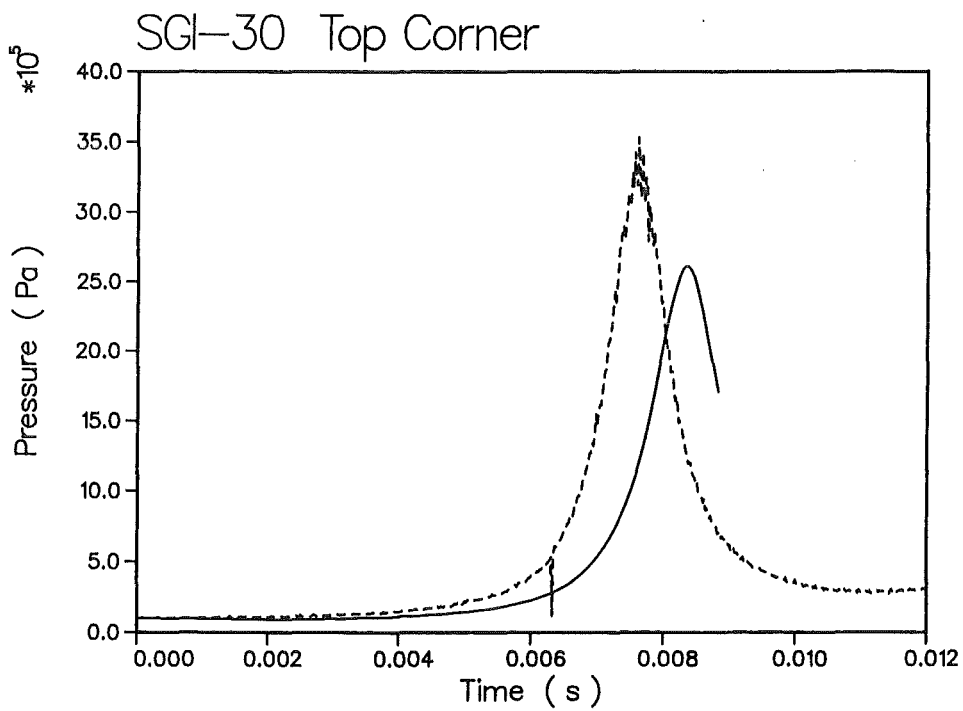**Fig. B.26.** AFDM pressure (solid line) and experimental pressure (dashed line) for SGI-30

Fig. B.27. AFDM pressure (solid line) and experimental pressure (dashed line) for SGI-30
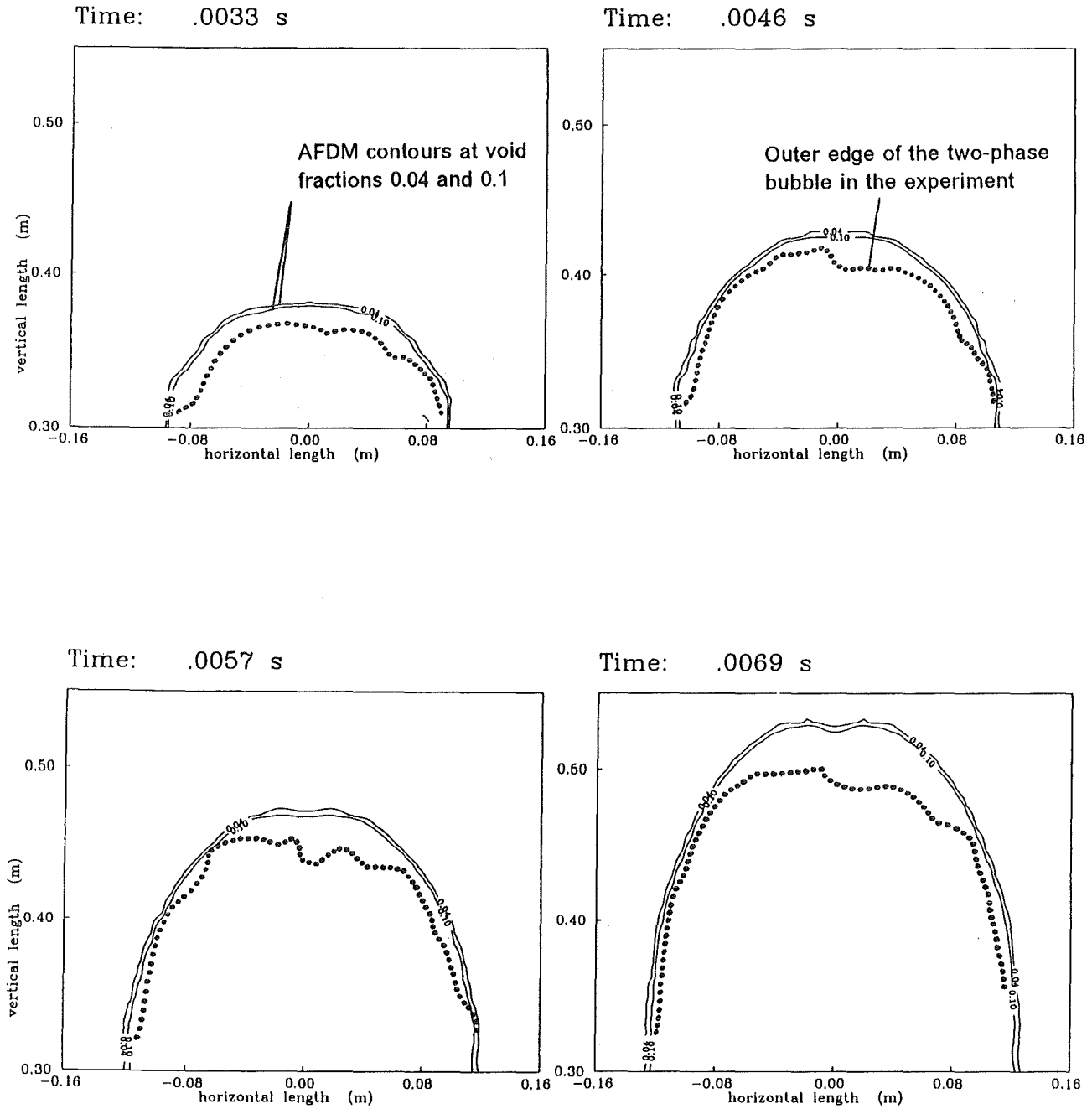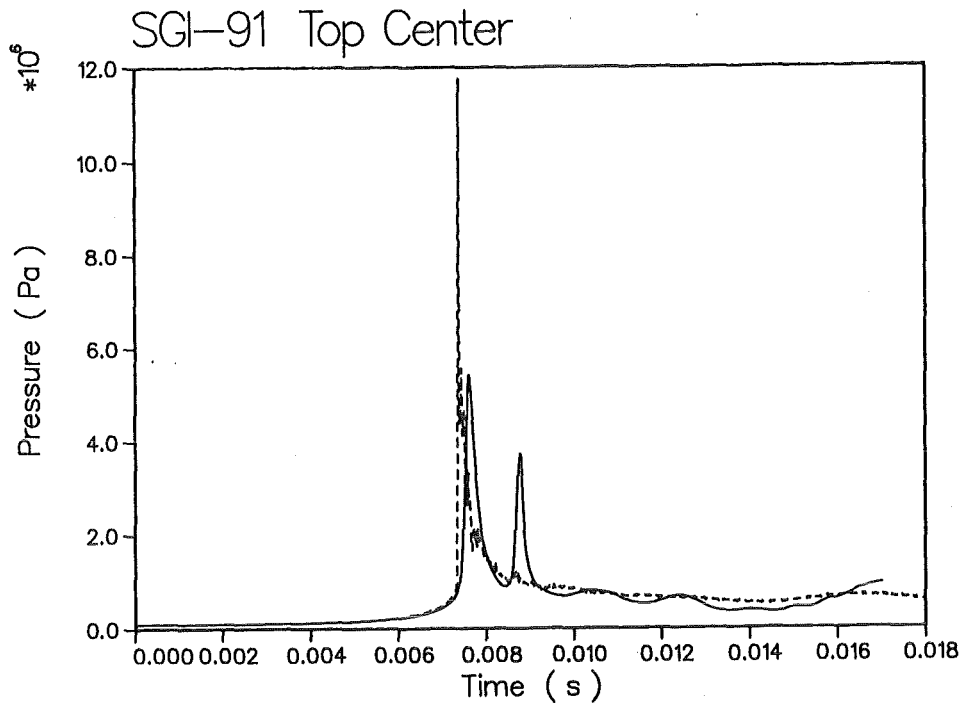
SGI-30

Time: .0033 s

Time: .0046 s

Time: .0057 s

Time: .0069 s

Fig. B.28. Comparison of SGI-30 void fraction contours between experiment and AFDM

SGI−91

FLUID MESH
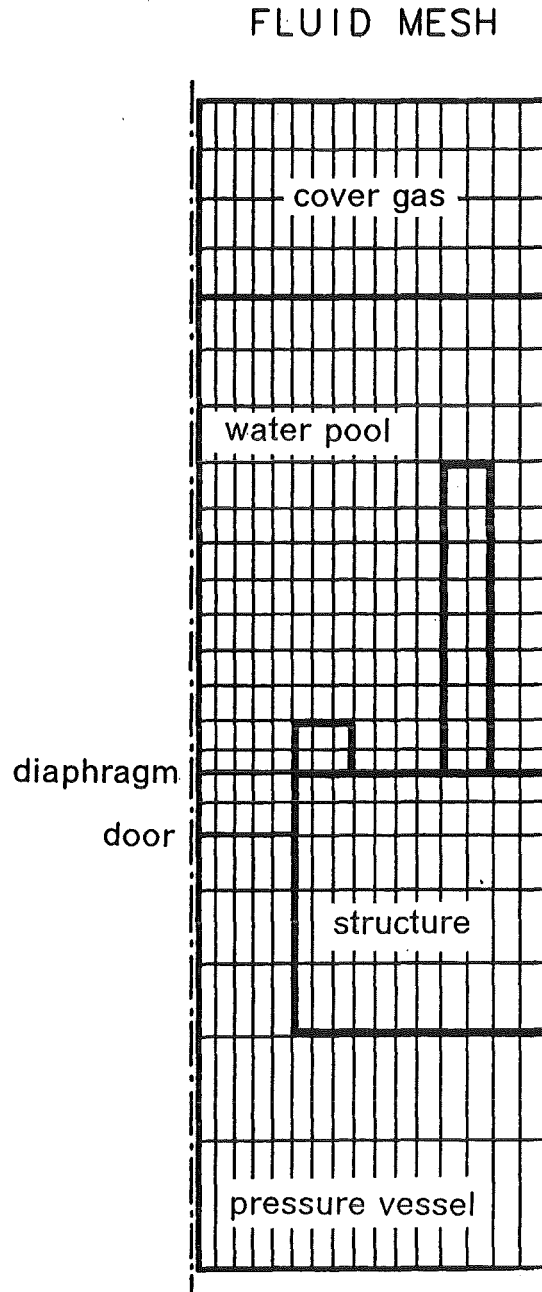
Fig. B.29. AFDM mesh cell set for SGI-91, right side of cylinder

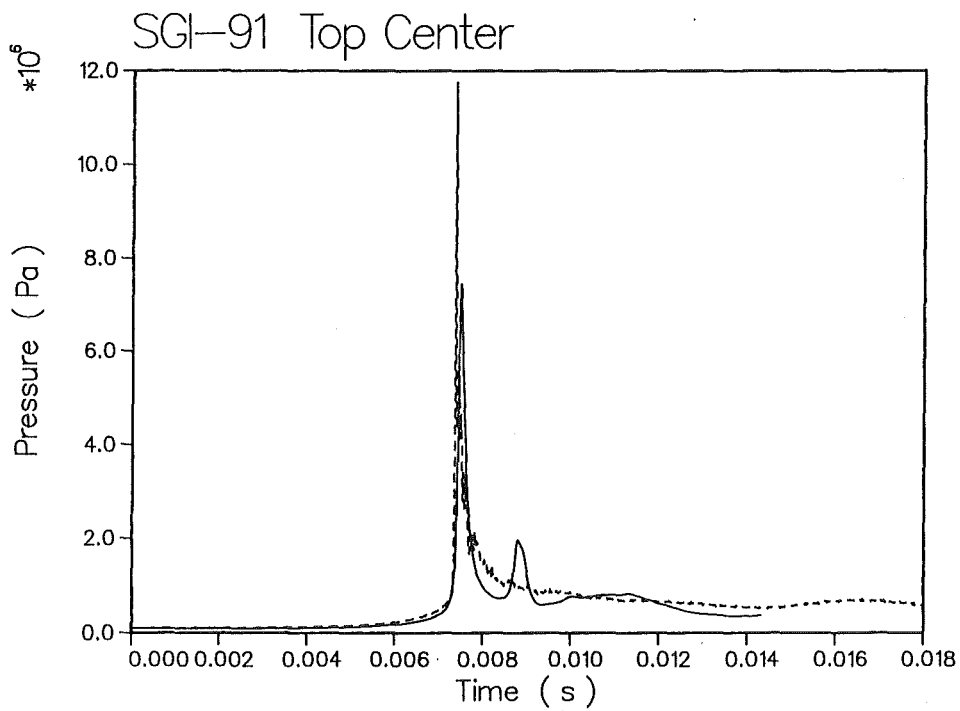**Fig. B.30.** AFDM pressure (solid line) and experimental pressure (dashed line) for SGI-91

Fig. B.31. AFDM pressure (solid line) and experimental pressure (dashed line) for SGI-91 with artificial void fraction
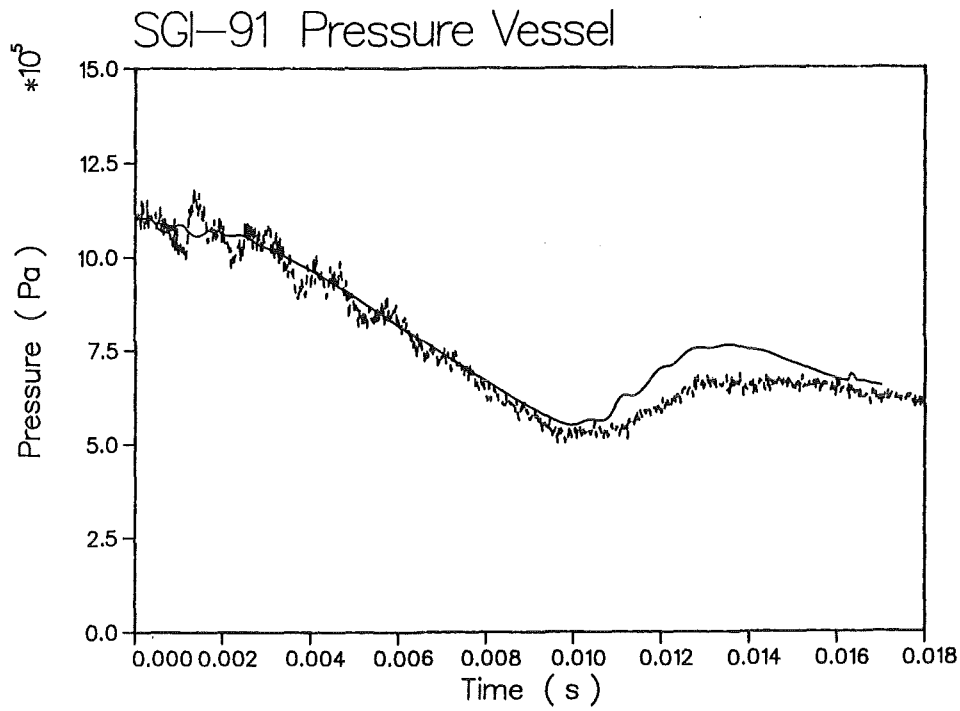
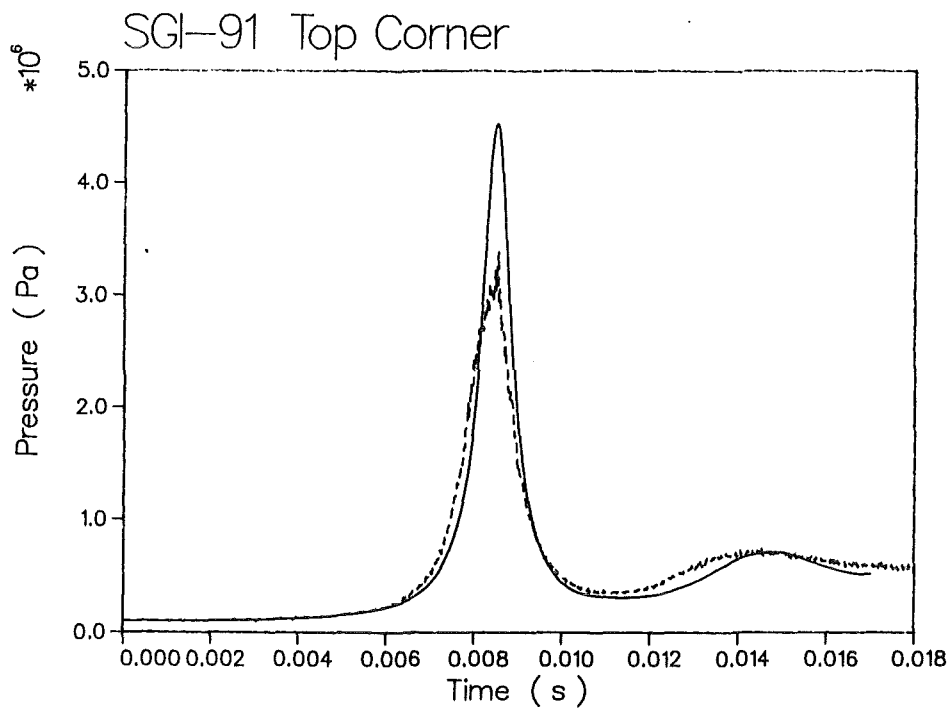**Fig. B.32.** AFDM pressure (solid line) and experimental pressure (dashed line) for SGI-91

Fig. B.33. AFDM pressure (solid line) and experimental pressure (dashed line) for SGI-91
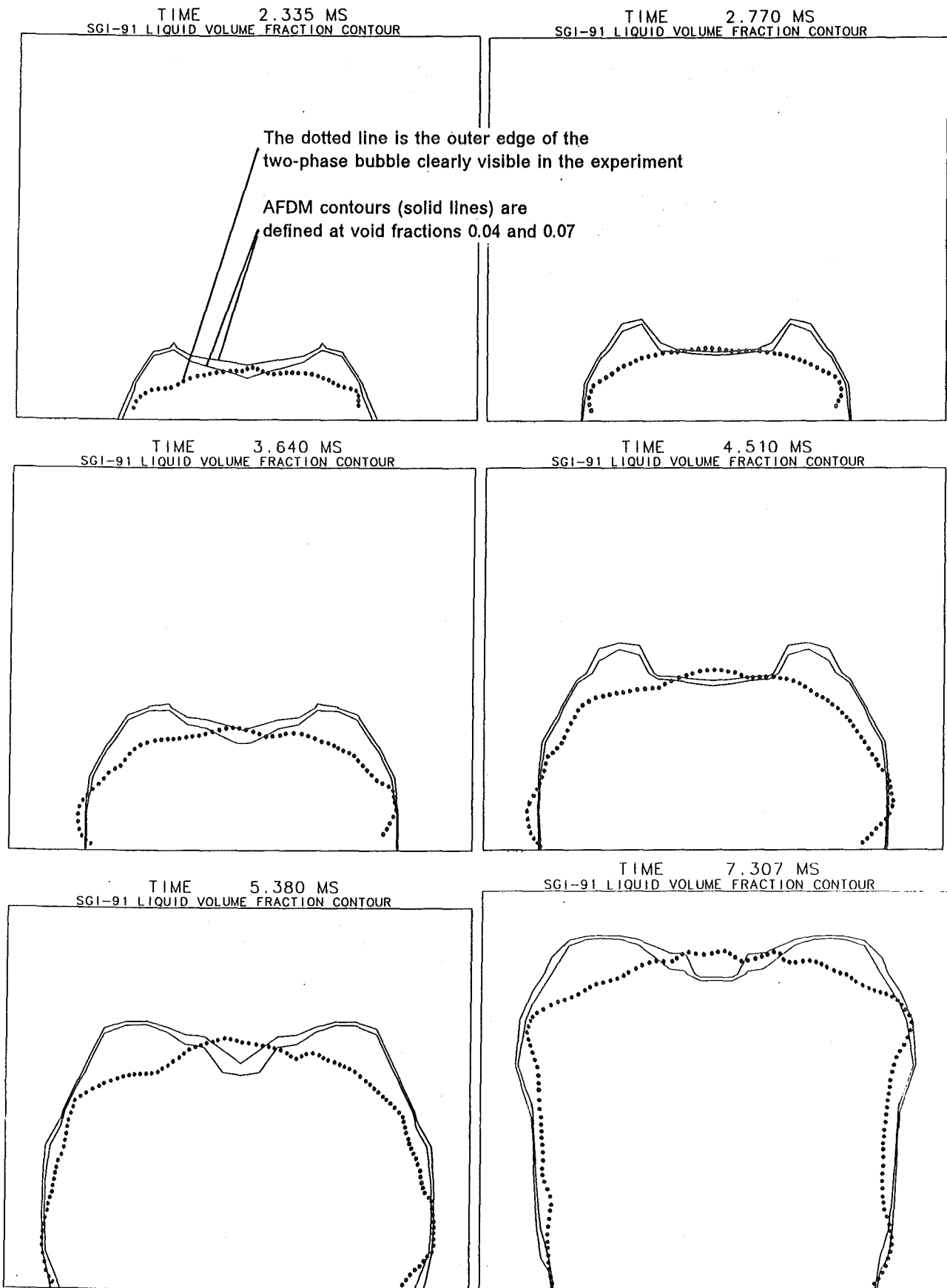
TIME   2.335 MS
SGI-91 LIQUID VOLUME FRACTION CONTOUR

TIME   2.770 MS
SGI-91 LIQUID VOLUME FRACTION CONTOUR

The dotted line is the outer edge of the
two-phase bubble clearly visible in the experiment

AFDM contours (solid lines) are
defined at void fractions 0.04 and 0.07

TIME   3.640 MS
SGI-91 LIQUID VOLUME FRACTION CONTOUR

TIME   4.510 MS
SGI-91 LIQUID VOLUME FRACTION CONTOUR

TIME   5.380 MS
SGI-91 LIQUID VOLUME FRACTION CONTOUR

TIME   7.307 MS
SGI-91 LIQUID VOLUME FRACTION CONTOUR

Fig. B.34. Comparison of SGI-91 void fraction contours between experiment and AFDM
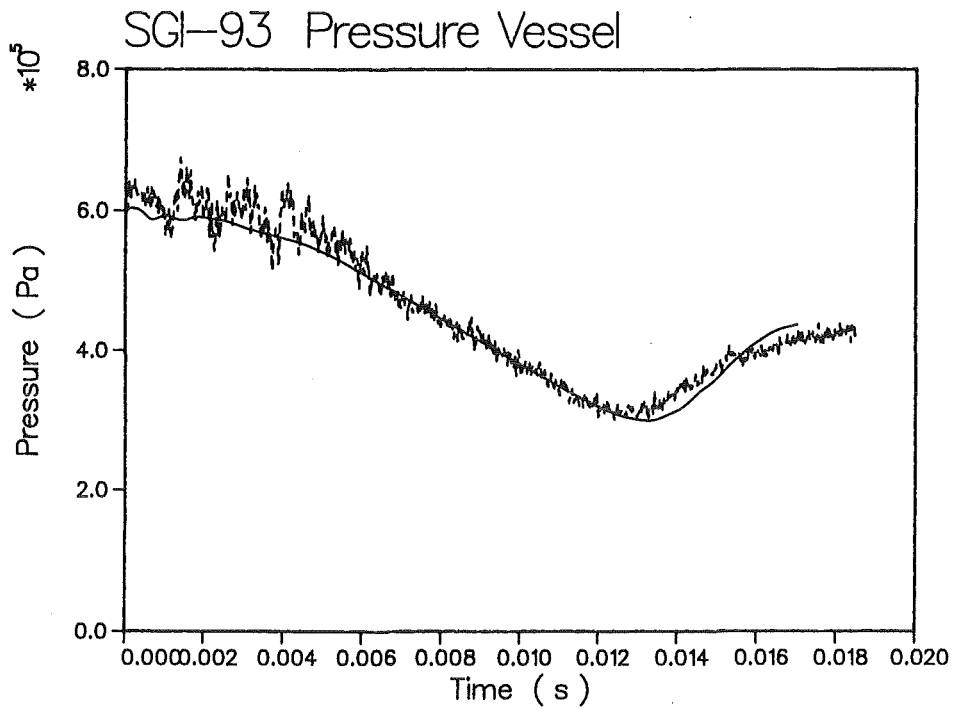
Fig. B.35. AFDM pressure (solid line) and experimental pressure (dashed line) for SGI-93
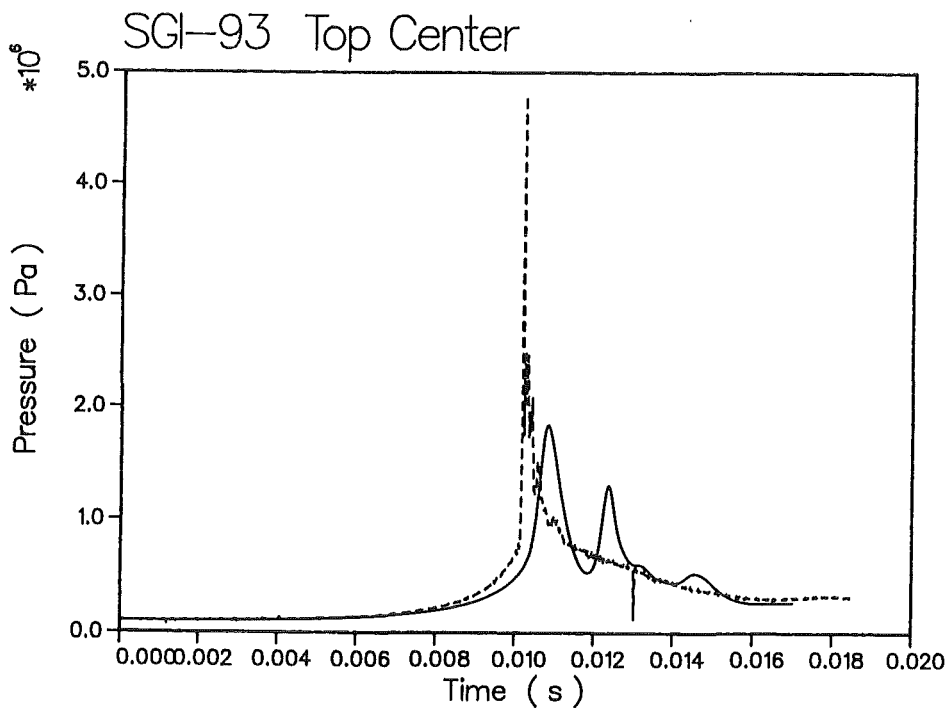

Fig. B.36. AFDM pressure (solid line) and experimental pressure (dashed line) for SGI-93

Fig. B.37. AFDM pressure (solid line) and experimental pressure (dashed line) for SGI-93

Fig. B.38. AFDM pressure (solid line) and experimental pressure (dashed line) for SGI-93
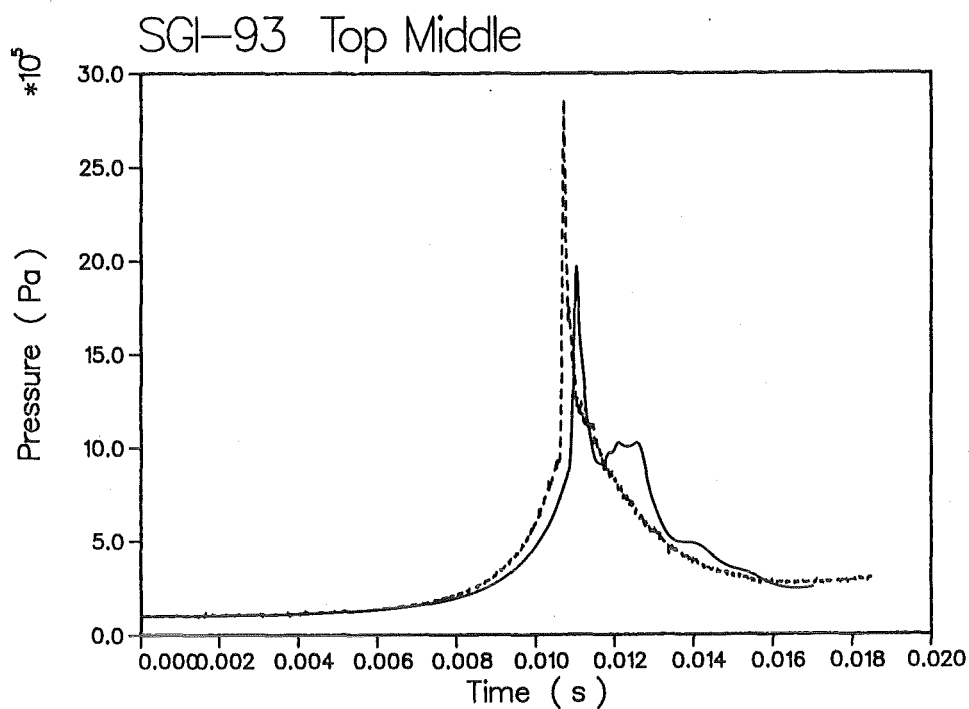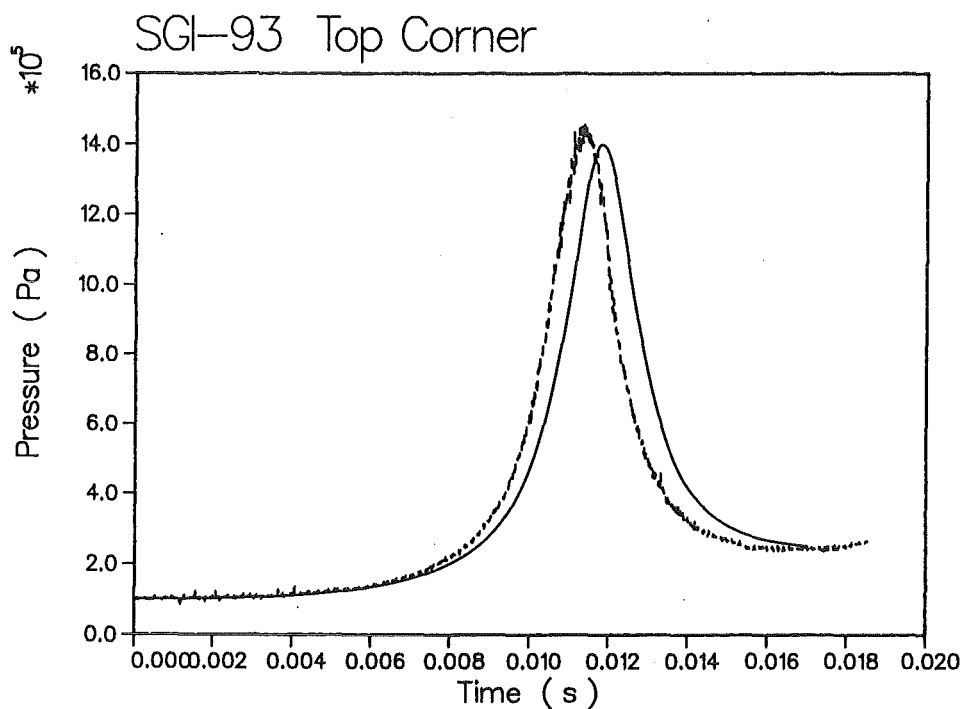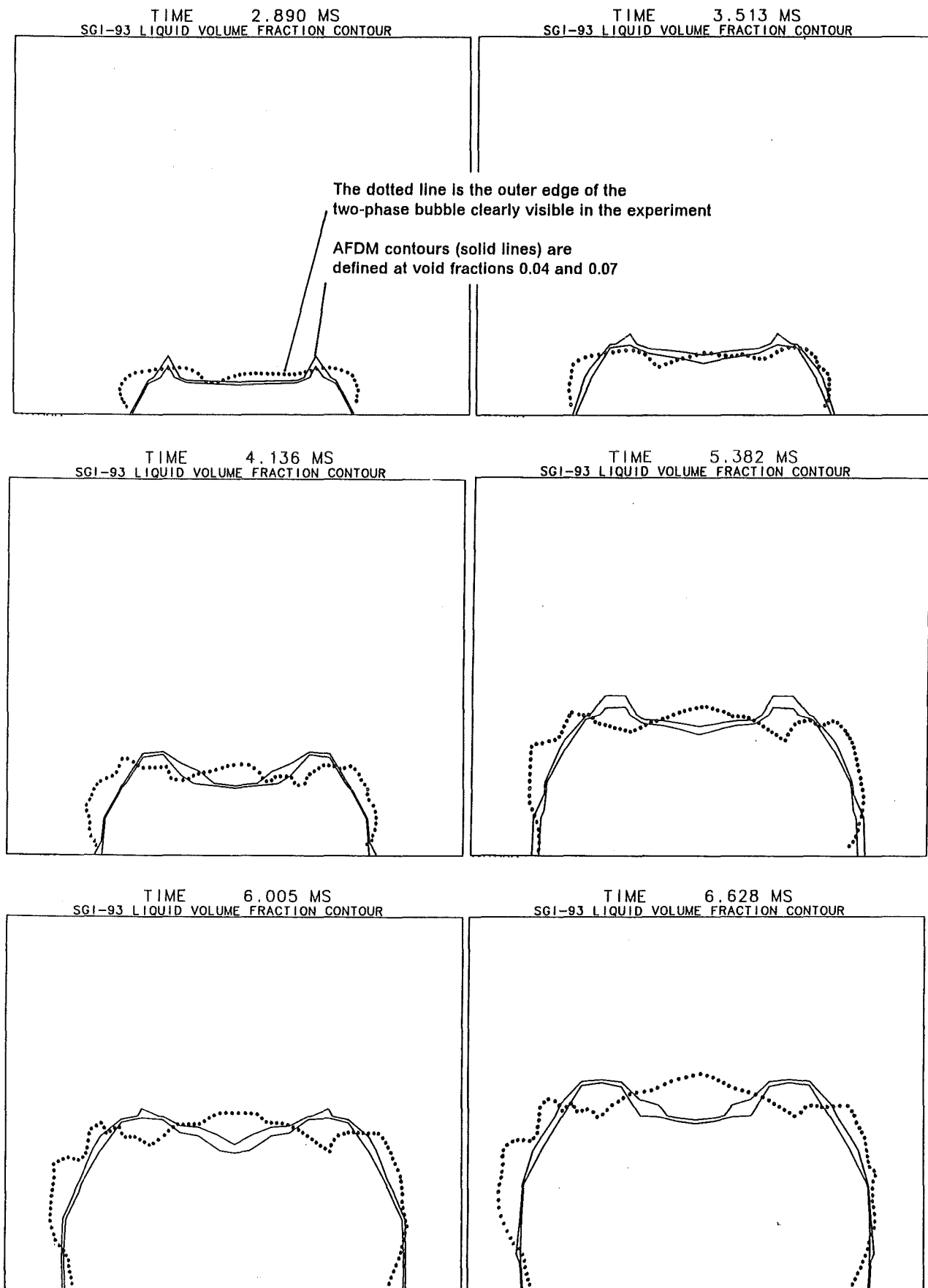
TIME   2.890 MS
SGI-93 LIQUID VOLUME FRACTION CONTOUR

TIME   3.513 MS
SGI-93 LIQUID VOLUME FRACTION CONTOUR

The dotted line is the outer edge of the
two-phase bubble clearly visible in the experiment

AFDM contours (solid lines) are
defined at void fractions 0.04 and 0.07

TIME   4.136 MS
SGI-93 LIQUID VOLUME FRACTION CONTOUR

TIME   5.382 MS
SGI-93 LIQUID VOLUME FRACTION CONTOUR

TIME   6.005 MS
SGI-93 LIQUID VOLUME FRACTION CONTOUR

TIME   6.628 MS
SGI-93 LIQUID VOLUME FRACTION CONTOUR

Fig. B.39. Comparison of SGI-93 void fraction contours between experiment and AFDM
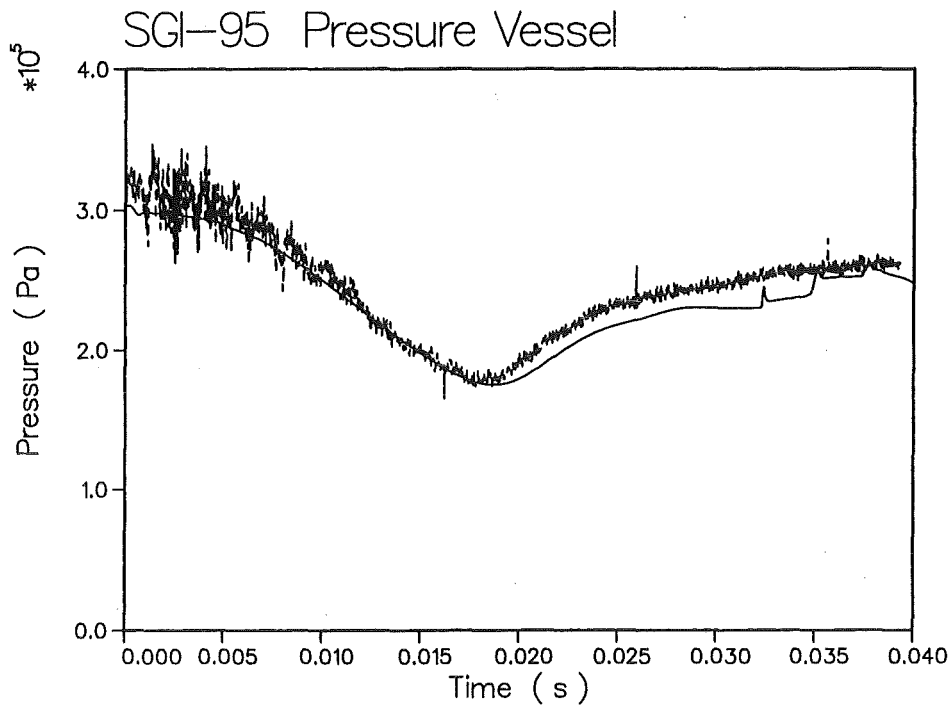
Fig. B.40. AFDM pressure (solid line) and experimental pressure (dashed line) for SGI-95
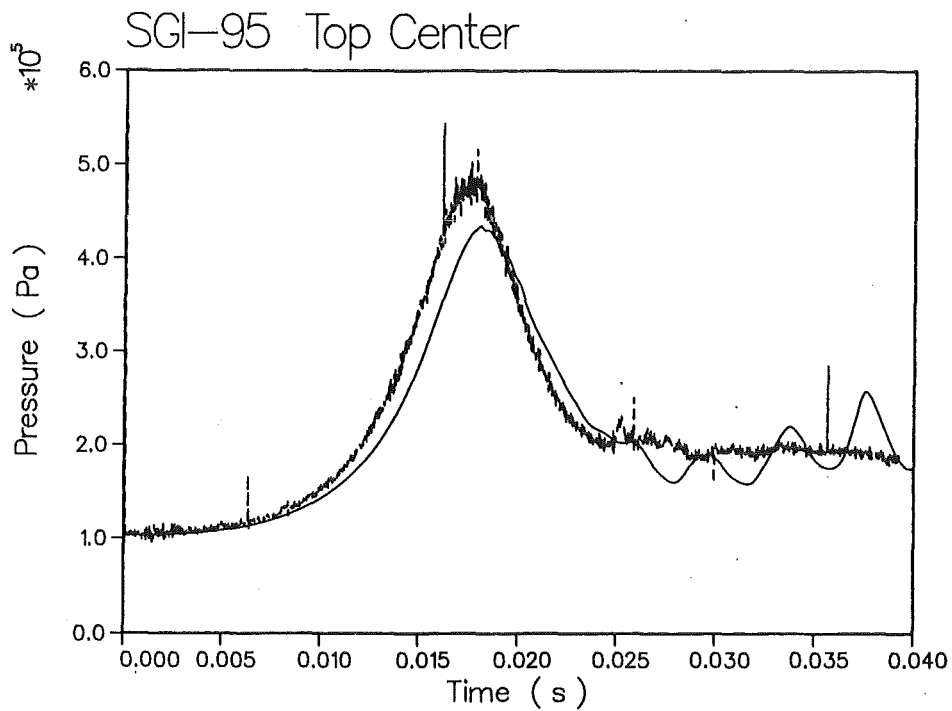

Fig. B.41. AFDM pressure (solid line) and experimental pressure (dashed line) for SGI-95

Fig. B.42. AFDM pressure (solid line) and experimental pressure (dashed line) for SGI-95

Fig. B.43. AFDM pressure (solid line) and experimental pressure (dashed line) for SGI-95
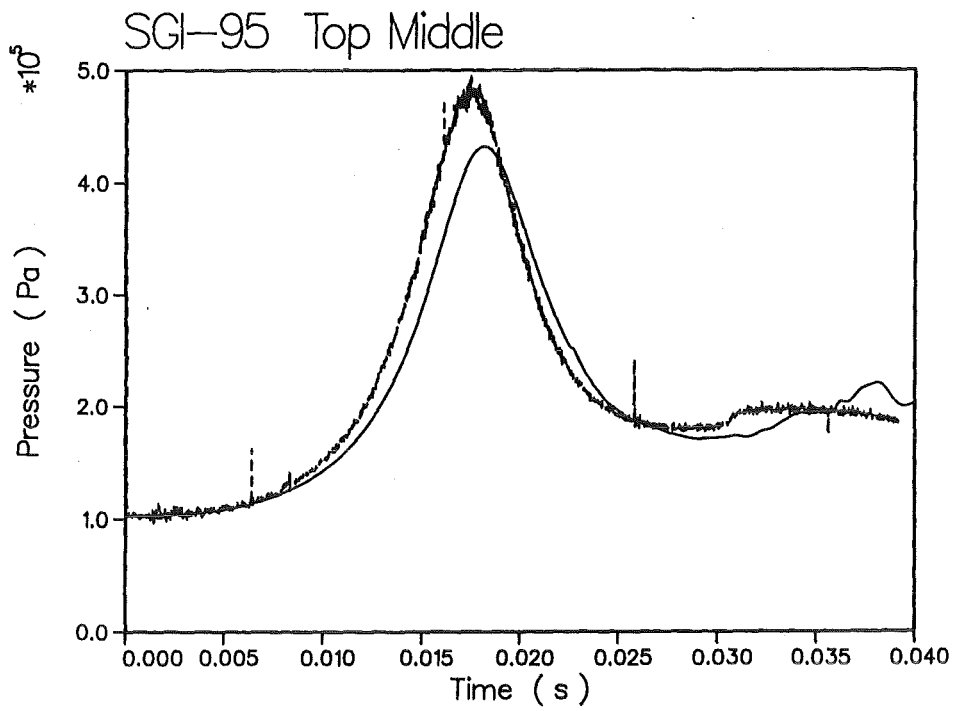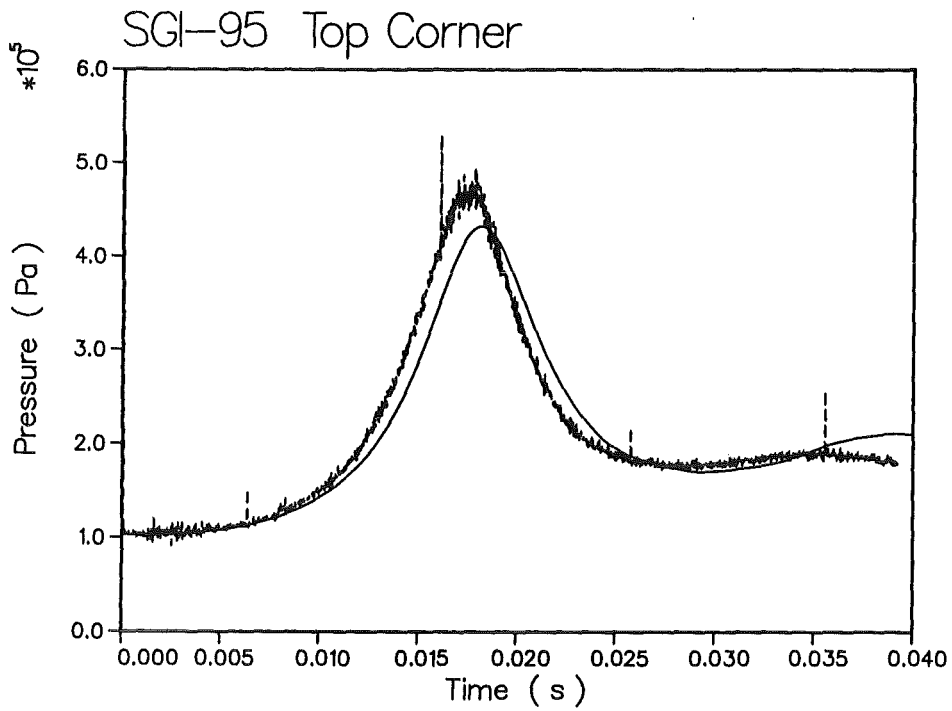
TIME   4.845 MS
SGI-95 LIQUID VOLUME FRACTION CONTOUR

TIME   5.782 MS
SGI-95 LIQUID VOLUME FRACTION CONTOUR

The dotted line is the outer edge of the
two-phase bubble clearly visible in the experiment

AFDM contours (solid lines) are
defined at void fractions 0.04 and 0.07

TIME   6.719 MS
SGI-95 LIQUID VOLUME FRACTION CONTOUR

TIME   8.593 MS
SGI-95 LIQUID VOLUME FRACTION CONTOUR

TIME   9.530 MS
SGI-95 LIQUID VOLUME FRACTION CONTOUR

TIME   11.404 MS
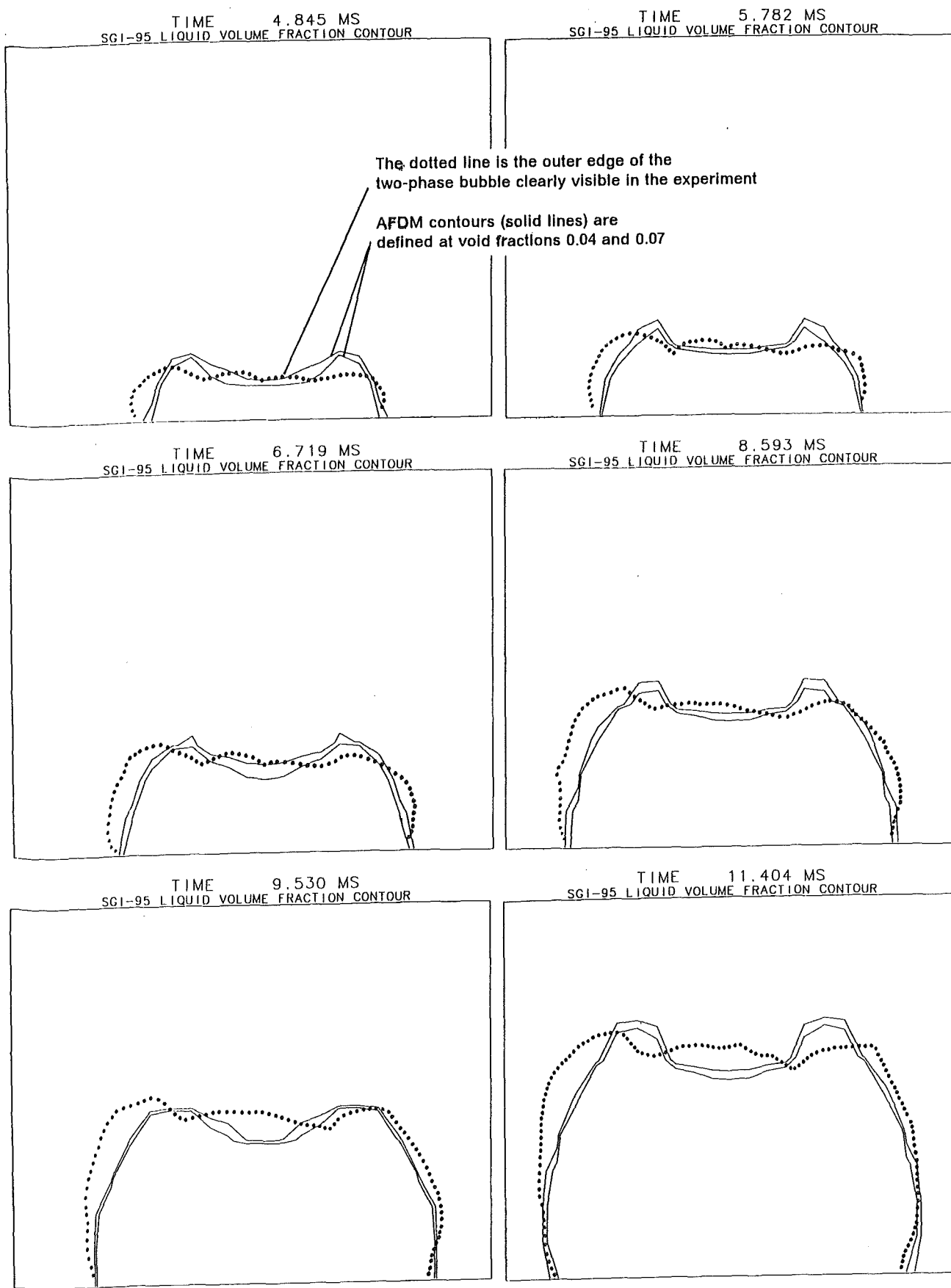SGI-95 LIQUID VOLUME FRACTION CONTOUR

Fig. B.44. Comparison of SGI-95 void fraction contours between experiment and AFDM